University of Southampton

FACULTY OF ENGINEERING AND PHYSICAL SCIENCES

OPTOELECTRONICS RESEARCH CENTRE

Tuneable silicon photonic devices and circuits

by

Xingshi Yu

Thesis for the degree of Doctor of Philosophy

Sep 2022

University of Southampton

Abstract

FACULTY OF ENGINEERING AND PHYSICAL SCIENCES

OPTOELECTRONICS RESEARCH CENTRE

Doctor of Philosophy

Tuneable silicon photonic devices and circuits

by

Xingshi Yu

The commercial market for silicon photonics is growing at a rapid pace. Many optical communications companies have developed their own techniques and products based on silicon photonic platforms. The cost is one of the most important factors in industrial production. The cost spent on testing, packaging and masks, and the yield of each manufacturing process, deeply affects the overall cost of each silicon photonics chip. In this project, new methods of wafer-scale testing, post-fabrication trimming, and programmable photonic circuits are proposed, which can be utilized to decrease the cost.

Several erasable and tuneable silicon photonic devices are demonstrated, including Mach–Zehnder interferometers, ring resonators and directional couplers. They are all developed by Ge ion implantation and annealing techniques. Ge ion implantation induces lattice damage and disorder in conventional silicon waveguide. The refractive index of implanted silicon waveguides, the effective index of propagating modes in these waveguides and the optical performance of devices are altered. This lattice damage can be altered afterwards via annealing processes, including laser annealing and integrated electrical annealing. The performance of implanted devices can be shifted after annealing. Based on this properties, these implanted devices can be used to realize reliable wafer-scale testing in photonic integrated circuit production. The erasable directional couplers can work as the optical input and output ports in large and complex photonic integrated circuits. The coupling efficiency can be designed from 0% to over 90% for each coupler. In order to avoid permanent parasitic loss, these optical testing points can be permanently removed from the main functional circuits after the testing. After full annealing of the implanted sections, the coupling efficiency of an implanted directional coupler dropped to -18dB or less. This residual insertion loss is negligible for optical transmission. The Ge ion implantation and annealing techniques can also be used to realize CMOS compatible post-fabrication trimming. The shift of optical performance brought by Ge ion implantation is larger than that caused by fabrication variations. The optical performance of implanted devices, such as the resonant wavelength of ring resonators and transmission of Mach–Zehnder interferometers, can be trimmed to the originally designed working points. Over one full-spectral range and 1.5π phase shift is achieved respectively for ring resonators and Mach–Zehnder interferometers in this project. The implanted Mach–Zehnder interferometers and directional couplers can act as the basic building blocks in programmable photonic circuits. The long-term power consumption and thermal crosstalk are no longer issues for programmable photonic circuits developed by Ge ion implantation and

integrated electrical annealing, making programmable photonic circuits viable for production for the first time.

Contents

CONTENTS ..... **I**

LIST OF TABLES ..... **V**

LIST OF FIGURES ..... **VII**

RESEARCH THESIS: DECLARATION OF AUTHORSHIP ..... **XI**

ACKNOWLEDGEMENTS ..... **XIII**

DEFINITIONS AND ABBREVIATIONS ..... **XV**

CHAPTER 1 INTRODUCTION **17**

1.1 SILICON PHOTONICS 17

1.2 WAFER-SCALE TESTING 18

1.3 POST-FABRICATION TRIMMING 19

1.4 PROGRAMMABLE PHOTONICS CIRCUITS 19

1.5 THESIS OUTLINE 20

CHAPTER 2 LITERATURE REVIEW **22**

2.1 WAFER-SCALE TESTING 22

2.1.1 Conventional coupling methods in wafer-scale testing *22*

2.1.2 Testing probe *25*

2.2 POST-FABRICATION TRIMMING 26

2.2.1 Conventional post-fabrication trimming methods *27*

2.2.2 Post-fabrication trimming methods using ion implantation and annealing *29*

2.3 TUNEABLE OPTICAL COUPLER AND PROGRAMMABLE PHOTONIC CIRCUITS 35

2.3.1 Tuneable optical units *36*

2.3.2 Waveguide meshes *38*

2.4 SUMMARY 40

CHAPTER 3 THEORY **42**

3.1 AMORPHISATION INDUCED VIA GE-ION IMPLANTATION 42

3.1.1 Ion implantation *42*

3.1.2 Refractive index *44*

3.1.3 Refractive index change by Ge-ion implantation *45*

3.2 RECRYSTALLISATION BY LASER ANNEALING 46

3.3 PHOTONICS WAVEGUIDE 48

3.3.1 Waveguide theory *48*

3.3.2 Silicon on insulator platform *50*

3.4 DIRECTIONAL COUPLERS 51

3.5 Multimode interferometer 53
3.6 Mach-Zehnder interferometer 58
3.7 Ring resonator 60
3.8 Summary 63

CHAPTER 4 DEVICE DESIGN, SIMULATION AND FABRICATION 64

4.1 Device design and simulations 64
4.1.1 Simulation results: MZIs 64
4.1.2 Simulation results: ring resonators 67
4.1.3 Simulation results: single-stage directional couplers 70
4.1.4 Simulation results: two-stage directional couplers 73
4.2 Heater design and thermal simulation 75
4.3 Device fabrication processes 77
4.4 Summary 80

CHAPTER 5 EXPERIMENTAL SETUPS FOR ANNEALING AND DEVICE CHARACTERISATION 81

5.1 Continuous wave laser annealing setup 81
5.2 Pulsed laser real-time annealing setup 82
5.2.1 Annealing setup with real-time spectrum monitoring 82
5.2.2 Annealing setup with real-time gradient feedback 83
5.3 Optical characterisation and electrical annealing setup 84
5.4 Summary 85

CHAPTER 6 EXPERIMENT RESULTS: RING RESONATORS TRIMMING 86

6.1 CW laser annealing of racetrack resonator 86
6.2 Pulse laser annealing of ring resonator and real-time monitoring 91
6.3 Pulse laser annealing of racetrack resonator and real-time monitoring 92
6.4 Electrical annealing of racetrack 94
6.5 Summary 97

CHAPTER 7 EXPERIMENTAL RESULTS: MZI TUNING 99

7.1 Pulsed laser annealing of MZI with real-time monitoring 99
7.2 Electrical annealing of MZI 101
7.3 High accuracy tuning of MZI 104
7.4 Summary 106

CHAPTER 8 EXPERIMENT RESULTS: ERASABLE DIRECTIONAL COUPLERS 107

8.1 Continuous wave laser annealing of erasable directional couplers 107
8.2 Electrical annealing of erasable directional couplers 110
8.3 High accuracy tuning of erasable DC 116
8.4 Summary 117

CHAPTER 9 CONCLUSIONS AND FUTURE WORK 118

9.1 SUMMARY AND CONCLUSIONS 118

9.2 FUTURE WORK 123

APPENDIX A MASK DESIGN 125

APPENDIX B PYTHON SCRIPTS 128

LIST OF REFERENCES 135

List of Tables

TABLE 9.1 - COMPARISON OF DIFFERENT TRIMMING METHODS FOR RING RESONATORS. 121

TABLE 9.2 - COMPARISON OF DIFFERENT METHODS FOR THE 2×2 COUPLERS IN PROGRAMMABLE PHOTONIC CIRCUITS..... 123

List of Figures

FIGURE 2.1 - SCHEMATIC OF PRISM WAVEGUIDE COUPLER. 23
FIGURE 2.2 - SCHEMATIC OF BUTT COUPLING. 24
FIGURE 2.3 - SCHEMATIC OF END-FIRE COUPLING. 24
FIGURE 2.4 - SCHEMATIC OF GRATING COUPLER. 24
FIGURE 2.5 - THE STRUCTURE OF IMPLANTED GRATING COUPLER AND ETCHED GRATING COUPLERS IN PHOTONIC CIRCUITS [101]. 26
FIGURE 2.6 - CROSS SECTION OF THE SILICON RING RESONATOR AFFECTED BY E-BEAM IRRADIATION [66]. 27
FIGURE 2.7 - THE RESONANT WAVELENGTH CHANGING IN TRIMMING PROCESS [66]. 28
FIGURE 2.8 - CROSS SECTION OF RING RESONATOR WAVEGUIDE UNDER POLYMER CLADDING [67]. 28
FIGURE 2.9 - RESONANT WAVELENGTH CHANGING UNDER UV LIGHT TRIMMING [68]. 29
FIGURE 2.10 - CROSS SECTION OF RING RESONATOR WAVEGUIDE UNDER A_2S_3 GLASS [69]. 29
FIGURE 2.11 - SCHEMATIC OF THE IMPLANTED MZI AND THE SCANNING ROUTE OF ANNEALING LASER SPOT [103]. 30
FIGURE 2.12 - NORMALIZED OPTICAL TRANSMISSION OF THE OUTPUT PORTS OF TWO MZIS DURING THE ANNEALING WITH 20× OBJECTIVE LENS [103]. 31
FIGURE 2.13 - (A) SCHEMATIC OF A RING RESONATOR WITH IMPLNTATION SECTION. (B) TRANSMISSION SPECTRA OF FABRICATED RING RESONATORS WITH DIFFERENT LENGTH OF IMPLANTED SETIONS [104]. 31
FIGURE 2.14 - TRANSMISSION SPECTRA OF 10μM RADIUS RING RESONATOR WITH 18^{O} IMPLANTATION SECTION BEFORE AND AFTER ANNEALING [104]. 32
FIGURE 2.15 - CROSS-SECTION OF BORON DOPED RING RESONATOR [105]. 33
FIGURE 2.16 - MEASURED BLUE SHIFT OF RESONANT WAVELENGTH [105]. 33
FIGURE 2.17 - CROSS-SECTION OF IMPLANTED RING MODULATOR [106]. 34
FIGURE 2.18 - RESONANCE SHIFTS AND CALCULATED CHANGE IN EFFECTIVE INDEX ACHIEVED AS A FUNCTION OF IMPLANTED DEFECT DOSE [106]. 34
FIGURE 2.19 - SILICON MICRORING MODULATOR FORMED BY A RIB WAVEGUIDE WITH A PN-JUNCTION, A GE IMPLANTED SECTION AND A TUNGSTEN HEATER ON TOP [107]. 35
FIGURE 2.20 - MEASURED RESONANT WAVELENGTH SHIFT AS A FUNCTION OF THE APPLIED ELECTRICAL HEATING POWER [107]. 35
FIGURE 2.21 - THREE TRANSMISSION MODES OF 2×2 TUNEABLE OPTICAL UNITS: (A) BAR, (B) CROSS, (C) PARTIAL. 36
FIGURE 2.22 - SKETCH OF TUNEABLE DIRECTIONAL COUPLERS. 36
FIGURE 2.23 - SKETCH OF TUNEABLE MZI. 37
FIGURE 2.24 - TRIANGULAR ARCHITECTURE OF WAVEGUIDE MESH [70]. 38
FIGURE 2.25 - RECTANGULAR ARCHITECTURE OF WAVEGUIDE MESH [70]. 39
FIGURE 2.26 - SKETCHES OF LOOP WAVEGUIDE MESH WITH (A) SQUARE, (B) HEXAGONAL AND 40
FIGURE 3.1 - (A) DEPICTION OF SELECTIVE AREA ION IMPLANTATION OF THE UNDERLYING TARGET SUBSTRATE, USING A BLOCKING MASK LAYER; (B) ION IMPURITY CONCENTRATION PROFILE IN THE TARGET WAFER [122]. 43
FIGURE 3.2 - POINTS DEFECT IN CRYSTAL LATTICE AFTER ION IMPLANTATION. 44
FIGURE 3.3 - SHIFT OF REFRACTIVE INDEX IN SILICON INTRODUCED BY DIFFERENT IMPLANTED ELEMENTS [130]. 46
FIGURE 3.4 - TEMPERATURE CHANGE VS. DIFFERENT DEPTH IN AMORPHOUS SILICON SAMPLE [133]. 48

List of Figures

Figure 3.5 - Slab waveguide geometry. 48
Figure 3.6 - Ray model of slab waveguide. 49
Figure 3.7 – Cross-section structure of (a) strip waveguide and (b) rib waveguide. 50
Figure 3.8 - Layer structure of Silicon on insulator wafer. 50
Figure 3.9 - Absorption spectra of silicon and silicon dioxide [141]. 51
Figure 3.10 - Geometry of directional coupler [1]. 52
Figure 3.11 - Simulated optical output of a directional coupler. 53
Figure 3.12 - Schematic of 2×2 MMI. 54
Figure 3.13 - Schematic of the step-index along the multimode structure [143]. 54
Figure 3.14 - Schematic of the multimode waveguide with the input field, a mirrored single image, a direct single image and two-fold images [143]. 56
Figure 3.15 - Geometry of 1×2 optical Mach-Zehnder interferometer. 58
Figure 3.16 - Geometry of 2×2 optical Mach-Zehnder interferometer. 59
Figure 3.17 - Geometry of ring resonator with single drop [146]. 61
Figure 3.18 - Geometry of ring resonator with additional drop bus waveguide. 62
Figure 4.1 - Simulated field profile of MMI working as 3dB coupler. 65
Figure 4.2 - Optical transmission of output1 changes as the function of taper width. 65
Figure 4.3 – Simulated field profile of MMI with W_{T1} is 2μM. 65
Figure 4.4 - Structure of MZI with implanted sections in two arms. 66
Figure 4.5 - Simulated optical transmission as a function of implanted length for different width. 66
Figure 4.6 - Simulated optical transmission of implanted MZI with different implantation length. 67
Figure 4.7 - Top view (a) and cross section (b) of Ge ion implanted ring resonator. 67
Figure 4.8 - Simulated spectra of implanted and unimplanted ring resonators. 68
Figure 4.9 - Top view (a) and cross section (b) of Ge ion implanted racetrack resonator. 69
Figure 4.10 - Simulated field profile of un-implanted racetrack (a) and implanted racetrack (b). (c) Optical spectra of implanted and un-implanted racetrack resonators. 69
Figure 4.11 - Simulated TE0 mode distribution of conventional waveguide (a) and implanted waveguide (b). 70
Figure 4.12 - (a) Top view and (b) cross-section of a single-stage implanted DC. 70
Figure 4.13 - Field profile of single-stage implanted DCs working at the highest coupling efficiency. (a) 30° bending and (b) 90° bending. 71
Figure 4.14 – Simulated transmission of single-stage implanted DCs with (a) 30° bending and (b) 90° bending implanted waveguide. 72
Figure 4.15 – Simulated transmission of single-stage implanted DCs with a 30° bending conventional waveguide. 73
Figure 4.16 - Top view (a) and cross section (b) of Ge ion implanted two-stage DC. 73
Figure 4.17 - (a) Simulated transmission of implanted DC as a function of implantation length. Simulated field profile of implanted DC with (b) 12μM, (c) 6μM and (d) 21μM implanted waveguide. 75
Figure 4.18 - Propagation loss of 10μM length and 1μM width heater on top of waveguide versus thickness of SiO_2 layer. 76
Figure 4.19 - Top view of heater on implanted waveguide. 77

Figure 4.20 - Simulated temperature distribution under 5V applied voltage. 77
Figure 4.21 - Fabrication processes of implanted MZI: (a) SOI wafer; (b) Etched grating couplers; (c) Etched rib waveguides; (d) Ge ion implantation; (e) SiO_2 cladding layer; (f) TiN heater; (g) SiO_2 protection layer; (h) Al contact pad. 79
Figure 4.22 - Mask design for (a) racetrack resonator, (b) MZI and (c) two-stage DC. 80
Figure 5.1 - Schematic of CW laser annealing setup. $\lambda 2$ represent the half-wave plate. And BS is a beam splitter. PBS is a polarizing beam splitter. CCD is a charge coupled device. MO is a microscope objective. 81
Figure 5.2 – Image of continuous wave laser annealing setup [100]. 82
Figure 5.3 - Pulsed laser annealing setup with real-time spectrum monitoring. 83
Figure 5.4 - Pulsed laser annealing setup with real-time gradient feedback [149]. 84
Figure 5.5 - Schematic of optical characterisation setup. 84
Figure 5.6 - Electrical thermal annealing and optical characterisation setups. 85
Figure 6.1 - (a) Top view of racetrack with implanted coupling region. (b) An optical microscope image of the fabricated racetrack resonator [150]. 86
Figure 6.2 - Transmission spectrum showing the difference between simulation and experimental results of un-implanted racetrack resonators [150]. 87
Figure 6.3 - Scanning path of laser spot. 88
Figure 6.4 - Raman spectra of Ge implanted silicon before (amorphous Si) and after annealing using three different power levels of the annealing laser [150]. 89
Figure 6.5 - Transmission spectra of ring resonators with various implantation lengths. (a) Annealing laser power was equal to 35mW; (b) Annealing laser power was equal to 45mW [150]. 90
Figure 6.6 - (a) Experiment setup for laser annealing of implanted ring resonators with real-time spectrum monitoring. (b) Measured resonant wavelength shift of the ring as a function of annealing length. (c) Measured resonant wavelength shift normalised to the FSR (in the range from 1540-1560nm) as annealing length was varied [149]. 91
Figure 6.7 - Measurement spectrum of the last annealed point before and after cooling down [149]. 92
Figure 6.8 - Experimental setup used for pulse laser annealing of racetrack resonators [150]. 93
Figure 6.9 - (a) Measured resonant wavelength shift of the ring as a function of annealing length. (b) Normalised transmission of implanted racetrack resonator before and after pulse laser annealing [150]. 93
Figure 6.10 - Extinction ratio of implanted racetrack as a function of annealing length [150]. 94
Figure 6.11 - (a) is the top view of an implanted racetrack with TiN heater on top and Ion implanted region is shown in purple colour. (b) is the cross-section of black dotted line position, not the zoomed image of (a). 95
Figure 6.12 - Resonant wavelength as a function of annealing time under 1.6V applied voltage. 96
Figure 6.13 - Simulated temperature distribution of the racetrack resonator under 1.6V applied voltage. 96
Figure 6.14 - Resonant wavelength as a function of applied voltage on racetrack. 97
Figure 7.1 - Illustration of pulsed laser annealing with ion implanted MZI [149]. 99
Figure 7.2 - (a) Measured transmission (T) signal shifts as the function of the pump spot position during the scanning along the whole 7 mm implanted section; (b) measured ΔT signal dependent on the pump spot

position. Measured values of (c) T and (d) ΔT for four subsequent annealing cycles, labelled 1–4 in (d), with red dot corresponding to a balanced working point as determined from minimum in ΔT of (c) [149]. 101

Figure 7.3 - A schematic of ion implanted MZI, (a) top view, (b) cross section view. (c) An optical microscope image of the fabricated implanted MZI with TiN heater [154]. 102

Figure 7.4 - Optical transmission spectrum of ion implanted MZI before and after annealing by 18 μm TiN filament [154]. 103

Figure 7.5 - Optical transmission shift of MZI under 0.2V voltage rising step and 20s annealing time. 104

Figure 7.6 - Optical transmission shift of MZI under 0.02V voltage rising step and 0.1s annealing time. 105

Figure 8.1 - (a) Top view of implanted two-stage DC. (b) Illustration of laser annealing process for two-stage DCs [73]. 108

Figure 8.2 - Measured optical transmission of two-stage implanted directional couplers [73]. 108

Figure 8.3 – (a) Top-view of a single-stage DC. (b) Measured transmission of implanted single-stage DC during the CW laser annealing process [73]. 109

Figure 8.4 - Schematic of single-stage implanted DC with optimized bending region. 110

Figure 8.5 - Top view (a) and cross section (b) of ion implanted two-stage directional couplers with TiN heater. (c) An optical microscope image of the fabricated implanted two-stage DC with TiN heater. (d) Mask layout of an implanted two-stage DC with TiN heater [154]. 111

Figure 8.6 - Optical transmission of DC before and after annealing by 19 μm TiN filament [154]. 112

Figure 8.7 - Measured dynamic results of annealing process for an implanted two-stage DC with 17mm filament [154]. 113

Figure 8.8 - Temperature distribution of implanted two-stage DC under 7V applied voltage [154]. 113

Figure 8.9 - Experimental results showing dynamics of the annealing process for a directional coupler with 16mm TiN filament [154]. 114

Figure 8.10 - Simulation result showing a temperature distribution of implanted two-stage DC under 6.5V applied voltage [154]. 114

Figure 8.11 - Experimental and simulation voltage supplied on the filament achieving fully annealing [154]. 116

Figure 8.12 - Measured optical transmission of implanted two-stage DC under high accuracy control of applied electrical power. 117

Figure A.9.1 – Mask design for implanted DCs, implanted racetrack and Implanted MZIs used for low accuracy electrical annealing. 125

Figure A.9.2 – Mask design for implanted racetrack, implanted MZIs and implanted DCs used for high accuracy electrical annealing. 126

Figure A.9.3 – Mask design for implanted MZIs, implanted DCs and tuneable switching networks. 127

Research Thesis: Declaration of Authorship

Print name:

Title of thesis:

I declare that this thesis and the work presented in it are my own and has been generated by me as the result of my own original research.

I confirm that:

1. This work was done wholly or mainly while in candidature for a research degree at this University;
2. Where any part of this thesis has previously been submitted for a degree or any other qualification at this University or any other institution, this has been clearly stated;
3. Where I have consulted the published work of others, this is always clearly attributed;
4. Where I have quoted from the work of others, the source is always given. With the exception of such quotations, this thesis is entirely my own work;
5. I have acknowledged all main sources of help;
6. Where the thesis is based on work done by myself jointly with others, I have made clear exactly what was done by others and what I have contributed myself;
7. #Delete as appropriate#None of this work has been published before submission #or# Parts of this work have been published as:- #please list references below#

[Add references here] #otherwise delete#

Signature: ..... Date: .....

Acknowledgements

My PhD project would not have been possible without the help of others. First and foremost, I would like to express my gratitude to my supervisors, Prof. Graham Reed, Prof. Shinichi Saito, Dr. Milan Milosevic and Dr. Xia Chen. They guided me throughout this journey and offered their insight in silicon photonics. Thanks to them for bring me into this field, always giving me encouragement, answering my endless questions, and giving me countless help in everything from this project to my life.

I would like to say big thank you for all the Silicon photonics group members for supporting me in countless moments. Dr. Yangbo Wu, Dr Yanli Qi, Dr. Libe Arzubiaga Totorika, Dr. Xiangjun Wang, Bharat Pant, Dr. Zhibo Qu, Dr. Wei Cao, Dr. Weiwei Zhang, Dr. Shenghao Liu, Dr. Bigeng Chen, Dr. Xingzhao Yan, Dr. Fanfan Meng and Dr. Teerapat Rutirawut have all helped me in all things from simulations to measurements and fabrication.

I am grateful to the China Scholarship Council (CSC) and Optoelectronics Research Centre (ORC) for providing my studentship that has made this work possible.

I am also thankful to the roommates from Mayflower Halls. Their friendship is indispensable part in my 4-year PhD journey. The time we spent together is the most precious memories in my whole life. Especially thanks to Shubin Wu, who give me endless help and care during the pandemic and lockdown.

I would also like to thank Weng Yee Chong (Beverly) to give me lots of help in life when I write this thesis.

Above all, I would like to express my deepest gratitude to my parents. They give me all their love, patience and support in every second. They always stood by me through all my travails, my absences, my fits of pique and impatience. I also would like to thank to my sister, Ruoxi Ding. She gives me unlimited happiness and pleasure.

Definitions and Abbreviations

CMOS ..... Complementary metal-oxide semiconductor

PIC ..... Photonic integrated circuit

LiDAR ..... Light detection and ranging

OOK ..... On-off-keying

CWDM ..... Coarse wave division multiplexing

5G ..... 5th generation wireless systems

MZI ..... Mach-Zehnder interferometer

FPGA ..... Field programmable gate array

DC ..... Directional coupler

SOI ..... Silicon on insulator

MEMS ..... Micro-electromechanical systems

CW laser ..... Continuous wavelength laser

TEM ..... Transverse electromagnetic

TE ..... Transverse electric

TM ..... Transverse magnetic

MMI ..... Multi-mode interferometer

BOX ..... Buried oxide

PECVD ..... Plasma-enhanced chemical vapor deposition

DUV ..... Deep ultraviolet

CCD ..... Charge-coupled device

FSR ..... Free spectral range

Q factor ..... Quality factor

FWHM ..... Full width at half maximum

Chapter 1 Introduction

1.1 Silicon photonics

Silicon photonics is one of the hottest topics in commercial applications and academic research in laboratories. Silicon photonics provides lower fabrication cost and higher integration flexibility than other photonics platform, such as $LiNbO_3$, III-V semiconductors and silica [1-8]. Benefitting from these advantages and mature complementary metal-oxide-semiconductor (CMOS) fabrication techniques, the research and applications of silicon photonic integrated circuits (PICs) had attracted great interests from both the academic community and industry for a few decades. Huge resources and efforts have been put into this area. The performance of silicon photonic components including integrated laser sources, optical couplers, optical filters, optical switches, optical modulations and optical detectors have also been improved to replace the traditional solutions, which were typically realized on III-V semiconductors, lithium niobate, and silica [9-35]. A lot of companies and research groups have utilized silicon photonics to realize high speed data transmission, optical information networks, chemical sensing, bio sensing and light detection and ranging (LiDAR) applications [36-55].

For optical communications, the operation speed of silicon photonic transmitters has reached more than 100 Gbps on-off keying (OOK) with the power efficiency of the driver at 2.03pJ/bit [36]. One of the leading companies in silicon photonics, Intel, has realized mass production and shipment of silicon photonic 100G, 200G and 400G coarse wavelength division multiplexing (CWDM) transceivers [50, 54]. Those silicon photonic transceivers are used in datacentres and communication base stations of 5th generation wireless systems (5G). The power required for information processing and communication typically grows with the increasing volume of internet traffic. Silicon photonics can provide high-integration, energy-efficient and power-saving communication solutions. In addition to optical communications, silicon photonics has been proposed for many other applications. Silicon photonics can contribute to emerging applications such as LiDAR in automatic smart driving [56]. Compared with the traditional solutions, the mature fabrication techniques of silicon photonic chips allow high integration levels of complex optical components. It also has the advantage of low cost and outstanding performance. Chemical and biological sensing are also attractive commercial areas for silicon photonics. Silicon photonics technology has already stepped into the products in our daily life. The Apple company has worked with photonics company Rockley Photonics to develop silicon photonics sensing modules into the Apple Watch to monitor the biological parameters such as blood oxygen level [50]. Many other companies such as IBM and HP have also been involved in the research and marketization of

silicon photonics [52, 53]. Based on the report from Yole Development, the compound annual growth rate of silicon photonic market between 2020 and 2026 is predicted to be around 49% [50].

Silicon photonics has achieved huge success in photonic commercial applications. The cost of silicon photonic products is one of the most significant factors in commercial markets and it is highly regarded by the investors. Improving the yield of the production process of silicon photonics will greatly reduce the cost. The target of this project is developing erasable and tuneable silicon photonic devices via ion implantation and annealing processes. These devices can be used in wafer-scale testing, post-fabrication trimming and building universal programmable photonic circuits. Wafer-scale testing and post-fabrication trimming techniques can improve the yield and decrease the cost of industrial production. The development of programmable photonic circuits in an industrial scale can reduce the non-recurrent engineering cost and the lead time of photonic chips.

1.2 Wafer-scale testing

Silicon photonic products have been widely deployed in the commercial market, where the cost of mass production is the key metric that attracts much attention. In the industrial production of silicon PICs, yield of photonics chip has always been the substantial factor affecting the cost of the products [51, 55]. Reliable and efficient testing methods for optical circuits at wafer scale have played a significant role in industrial production. During the production process, some part of PICs needs to be characterized individually. This is similar with the debugging process for the electrical circuits in the semiconductor industry. The traditional coupling methods used for testing such as prism waveguide coupler and butt waveguide coupling are not suitable for testing for silicon photonic circuits in wafer scale. The grating coupler is one of the most widely used structures for optical signal coupling in large-quantity production. The detailed analysis of these coupling methods will be discussed in chapter 2.

With the increasing complexity of silicon photonic circuits, a big integrated photonic circuit may consist of several sub-circuits with different functions [57]. They may need to be tested individually. However, the conventional design of the testing structure will result in additional insertion loss for the photonic circuits after finishing testing process [58]. This issue could cause significant residual insertion loss (parasitic loss) of the whole PICs, when integration level keeps raising. The overall insertion loss is normally a testing parameter for the photonic products, such as optical transmitter and receiver. Large insertional loss can result in low yield and high cost.

This project aims to solve this problem. An erasable optical testing method realized by Ge ion implantation and annealing processes is successfully demonstrated. Compared with the traditional testing methods for photonic circuits, the erasable testing ports mentioned in this thesis induce negligible residual insertion loss. They are more suitable and reliable for the wafer-scale testing in industrial production and research study of large-scale silicon photonics wafers. And it is CMOS compatible, which can enable future integration with CMOS electronics.

1.3 Post-fabrication trimming

The parameters of each fabrication process across the whole wafer are subject to fabrication tolerances [59-62]. Fabrication process variations will mean that the measured performance of optical devices and circuits are different from the simulation results [61-63]. For example, the resonant wavelength of a ring resonator and its critical coupling are sensitive to the device dimensions. The transmission of a Mach–Zehnder interferometer (MZI) also depends on the phase difference between the two arms, which in turn can be affected by fabrication tolerances. These are significant parameters for applications such as sensing and optical modulation [64, 65]. The devices that are not working properly will directly decrease the yield of production and increase the production cost. Post-fabrication trimming can be used for correcting the variation of devices' performance caused by fabrication variations. The money and time spent on their fabrication processes can therefore be salvaged.

Post-fabrication trimming processes typically correct the working performance of devices by shifting the effective index of propagating mode. The current trimming methods have the limitation of throughput, cost, and sufficient corrective range. Furthermore, most methods are not CMOS compatible and not friendly for high volume production [66-69]. The trimming range and accuracy are also limited. The details of these methods will be reviewed in the next chapter.

In this project, we proposed a new trimming method, using Ge ion implantation and annealing. This method can bring a large effective index shift of propagating modes in waveguides. A wide trimming range is provided, and it is CMOS compatible. This method is also more suitable for large-scale industrial production due to its high throughput and low cost.

1.4 Programmable photonics circuits

Based on the continuous development of silicon photonics and mature CMOS fabrication technology, the integration level of photonic circuits increases to realize more complex functions. The function of each PIC can be significantly different for various applications. To reduce the cost

of the design and fabrication of photonic circuits, researchers have started to develop a universal programmable photonic circuit with more flexibility, which is made from meshes of connected waveguide and devices [70]. In addition, fabricating PICs with different designs and processes, will induce more variations into the production foundries. The universal photonic circuit with post-fabrication programmable ability has been regarded as the solution for this issue. The production line for these universal optical circuits with the same design will have a higher yield, because the fabrication processes are more controllable for the same design.

A programmable photonic chip is a universal signal processing chip which can be programmed based on the target functions and applications. By applying electrical controlling signals, such a chip could realize field-programmable gate array (FPGA)-like functions. The flow of light in this programmable photonic circuit can be electrically manipulated. A lot of design and fabrication time and cost can be saved [70]. The basic components of such a circuit are repeated waveguide meshes, devices and tuneable elements. Electrically controlled microheaters are used as tuneable elements in such a circuit, which operate via the thermo-optical effect in silicon. The basic building blocks of the optical distribution network are typically MZIs and directional couplers (DCs) [71-73]. The light propagation in these devices is tuned between two outputs. Therefore, the chip can be reprogrammed for different protocols. However, the function of the whole circuits is supported by hundreds, perhaps even thousands of electrical heaters. Consequently, large power consumption results, which may also cause the heat dissipation and thermal crosstalk problems in the whole integrated system.

The tuneable implanted MZIs and DCs introduced in this thesis are used to build a non-volatile programmable photonic circuit. The transmission route of light in these devices can be permanently changed by an electrical power signal. No continuous power supply is needed for its long-term operation.

1.5 Thesis outline

My work is to develop tuneable and erasable photonic devices based on electrical annealing of Ge ion implanted silicon waveguides and to demonstrate its applications. This technique can be used in the applications such as wafer scale testing, post-fabrication trimming of the optical components and developing tuneable building blocks for programmable photonics circuits.

Chapter 2 is a review of current research by other groups. I first review the methods of wafer scale testing. Then different methods for trimming are introduced and reviewed. And a review of the state-of-the-art of programmable photonic circuits is presented.

Chapter 3 introduces the basic theory of ion implantation, annealing and silicon waveguides. Then the theory of Mach-Zehnder interferometer, ring resonators and directional couplers are discussed.

Chapter 4 introduces the design, simulation and fabrication process of optical devices used in this project.

Chapter 5 shows all the experiment setups and experimental techniques used in this work for annealing and characterization.

Chapter 6 shows the results of annealing experiments of implanted ring resonators. Firstly, the results from racetrack ring resonators are discussed. The devices were annealed via a continuous wave laser to realize the trimming of coupling efficiency. Then the results from pulse laser annealing are also reported to anneal the amorphous sections in ring resonators. Finally, the results of electrical annealing carried out by integrated thermal heaters are discussed.

Chapter 7 shows the results of annealing experiments of implanted MZIs. I first report the pulse laser real-time annealing experiments for Mach-Zehnder Interferometers. Then the integrated electrical annealing of MZI with high accuracy control by using python coding is discussed.

Chapter 8 shows the results of annealing experiments of implanted directional couplers. Two different methods to anneal two-stage directional couplers were introduced, including a continuous wave laser and integrated electrical heaters. The high accuracy tuning of the working performance of the devices shows their potential to be actuators in programmable photonic circuits.

Chapter 9 includes conclusions for this thesis and a discussion of possible future research directions, and future work.

Chapter 2 Literature review

This chapter firstly discusses different methods of wafer-scale testing for PICs. In addition, the art regarding post-fabrication trimming for silicon optical devices is reviewed. Finally, the basic principles of programmable photonic circuits are discussed.

2.1 Wafer-scale testing

Wafer-scale testing is one of the key steps in semiconductor research and production lines. It can greatly improve the yield and reduce the cost of production. In this section, four conventional methods of coupling light into photonic circuits will be introduced and compared, and their applicability to wafer-scale testing are assessed. Then, the structure and properties of an erasable grating coupler is reviewed.

2.1.1 Conventional coupling methods in wafer-scale testing

When trying to couple an optical signal between optical fibre and a silicon waveguide, there are two issues to be considered. The first one is that the silicon waveguide is typically designed as polarization dependant; however, the standard optical fibre is not polarisation maintaining. This problem can be solved by adding a polarization controller between the laser source and input fibre or using polarization maintaining fibres instead. The second problem is the mismatch of mode size between the fibres and silicon waveguides, which affects the coupling efficiency. The diameter of optical mode in an optical fibre is approximately 10μm at 1550nm (telecommunications wavelength). For silicon waveguides, the common thickness is around 220nm, 340nm, 500nm or 3μm [74-75]. Except for the 3μm thick silicon waveguide, the cross-sectional area of silicon waveguides is nearly two orders of magnitude smaller than the single-mode fibre, which causes the mode mismatch. During the development of optical measurements, the most common methods for coupling are prism coupling, butt coupling, end-fire coupling and gratings [76-81].

The sketch of prism coupling is shown in Figure 2.1. A prism is designed to couple the optical power coming from the fibre into the waveguide. For planar waveguide, this method can work without sub-micrometre alignment. This advantage makes a relaxed alignment tolerance. In addition, by using this prism, the diameters of coupled laser beam can be hundreds of times the thickness of the waveguide. A coupling efficiency of 94% was achieved by Dror Sarid in 1979 [82]. In this work, the optical signal coupled in Ti diffused $LiNbO_3$ waveguide by a prism with a higher refractive index. This method requires the refractive index of prism to be greater than the

waveguide to achieving a phase match between input fibre and waveguide. However, a very few materials have the higher refractive index than silicon 3.48, therefore this method is not very common in testing of silicon photonic circuits [1, 81].

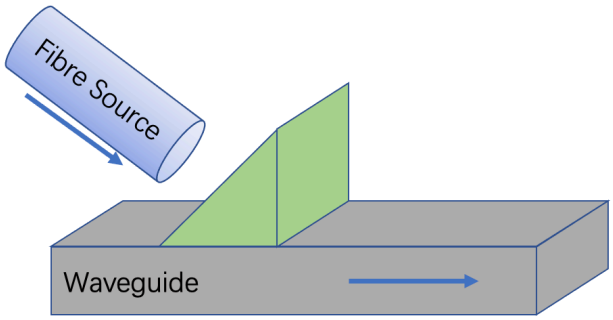

Figure 2.1 - Schematic of prism waveguide coupler.

Butt coupling is a quite straightforward method to couple light from source to the waveguide. In Figure 2.2, the optical fibre is brought close enough (micrometres) to the end of the waveguide with high demand of accurate alignment. Because the size of silicon waveguide is much smaller than the diameter of a fibre, it is difficult to realizing high efficiency coupling and has risk to induce additional insertion loss into testing system. Based on the study of Chen et al. in 2011, the coupling efficiency of single mode fibre (with an effective area of 75μm^2) and silicon photonic waveguides (with an effective area of 0.2μm^2) is less than 10% due to the mode mismatch issue [83]. For improving the coupling efficiency, some inverse tapers and three-dimensional tapers can be used, but increase complexity and alignment requirements. Furthermore, 3-dimensional tapers are very difficult to fabricate for very small waveguides, as roughness losses typically become prohibitive. The coupling efficiency has been increased to around 89% with the assistance of inverse tapers [84]. On the other hand, the usage of this coupling method should locate optical fibre at the edge of the chip with carefully polishing of the edge facets and precise controlling of the cleave process. These addition preparation works may bring more uncertain errors into measurement process, leading to a decrease of the production yield. By using three-dimensional tapers, the coupling efficiency between a fibre and the waveguides (with a height of 0.25µm and width of 1µm) can also boost to around 89% [85]. However, its length is around 600µm. This design strongly limits the integration ability of photonic circuits. In 2010, Cheben firstly experimentally demonstrated the subwavelength grating. A coupling efficiency of 90% was achieved with a 170nm bandwidth [86]. The device size is only approximately 160µm×100µm. In 2015, IBM demonstrated a fibre-chip coupling method by using subwavelength grating and V-grooves [87]. Facet polishing is no longer needed for this design. The peak coupling efficiency for TE mode is 92% while the bandwidth is 60nm with a 0.3dB spectrum roll-off. However, the length of one testing port is over 1mm. Therefore, this method might not be suitable for large production of PICs with high integration level.

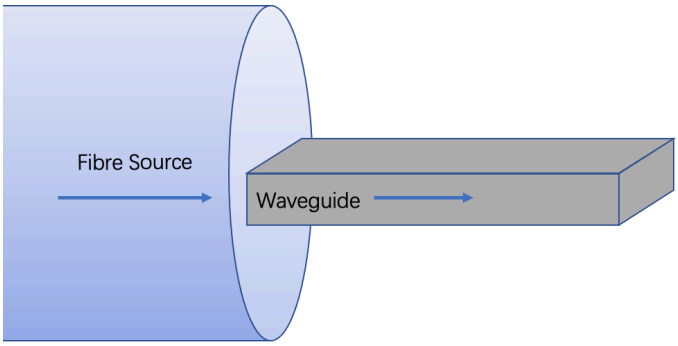

Figure 2.2 - Schematic of butt coupling.

For increasing the coupling efficiency between fibre and waveguide shown in Figure 2.2, a lens is utilized to focus the light beam from fibre to the end face of the waveguide, realizing high accuracy of mode matching. The schematic of end-fire coupling is shown in Figure 2.3, which is very similar with the structure of butt coupling. This method allows all the modes to be excited in the waveguide [88]. In 2018, 88% coupling efficiency has been achieved between emitting laser and single-mode fibre [89].

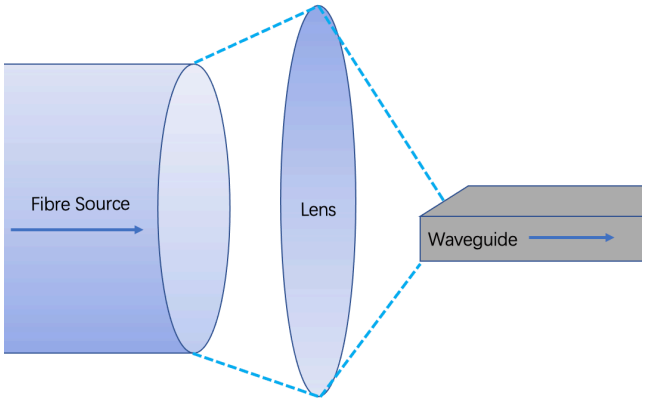

Figure 2.3 - Schematic of end-fire coupling.

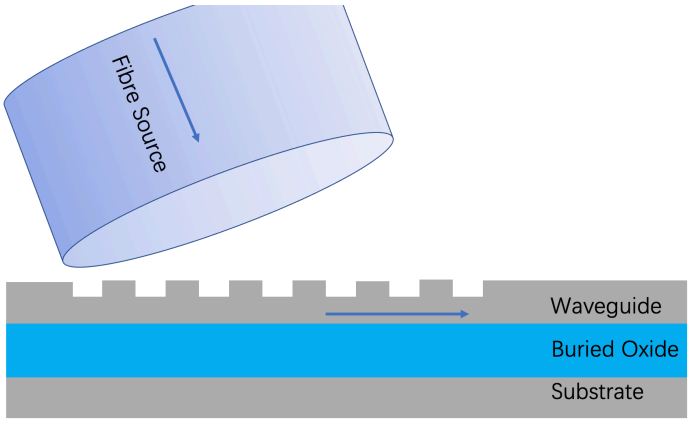

Figure 2.4 - Schematic of grating coupler.

Compared with the other three coupling methods, gratings are more popular in the testing of individual photonic components as well as integrated photonic circuits. A grating coupler comprises a periodic change in refractive index along the waveguide section to diffract the light

signal. The schematic of a standard grating couplers used for optical signal input coupling to the waveguide on silicon on insulator (SOI) wafer is shown in Figure 2.4.

Compared with the fixed horizontal position of the fibre in the butt coupling and end-fire coupling, the grating coupler can give the fibre source more flexibility of alignment angle [90]. The highest coupling efficient of a grating coupler is achieved when the fibre is placed at the correct position with a designed angle. Moreover, there is no additional preparation work needed for the waveguide before the testing, such as cleaving or polishing. In the mass production line, a simple alignment and implementation process is importance to reduce the cost. Chirped gratings are also demonstrated, allowing the fibre to be vertically positioned. This can potentially further simplify the alignment process [91].

However, the grating coupler method has its limitation on the wavelength range. A typically 1dB bandwidth of grating couplers is around 40nm [83, 92]. In 2012, A 1 dB bandwidth of approximately 73 nm has also been demonstrated by Chen. Et al. [93].

2.1.2 Testing probe

In wafer-scale testing for PICs, the output optical signal for testing is launched from the testing probes, which were realized by several techniques. In 2017, Michels et al. demonstrated an optical probe used for characterization of photonic elements [94]. This optical probe was made of a Si microdisk with an optical cavity. The optical signal can be coupled from waveguides into this microdisk. Then they coupled in the fibres attached with the V-grooves. The coupling loss for each facet is 5.5dB. In 2020, Mareike et al. used a 3D-printed optical probes as optical input and output for PICs [95]. The coupling approach between these probes and waveguides are quite similar with the end-fire coupling. 1.9dB per coupling interface was achieved.

Another approach is using conventional DCs and MZIs. The detailed theory of DCs and MZIs will be introduced in the next chapter. A part of optical power can be coupled from one waveguide to another. This coupled optical signal then is used for testing and subsequently coupled out into a testing fibre via a grating coupling. Because this method can achieve fast, accurate and flexible wafer-level testing for PICs, it has been accepted by companies which manufacture automatic wafer-level testing machines, including ficonTec and EXFO [96, 97].

However, with testing probes formed by fibres and conventional gratings for wafer scale testing, we cannot efficiently test a part of photonic circuits or components during the fabrication processes without inducing significant residual loss afterwards. An erasable directional coupler was previously demonstrated using Ge ion implantation and laser annealing technology [98-100].

This grating coupler can be erased from the photonic circuits with negligible residual insertion loss. This erasable grating couplers can also be used as testing probes in the automatic testing machines for PICs.

For the erasable gratings, the periodic change in refractive index along the waveguide input and output section is formed by the crystalline silicon and amorphous silicon, the latter created by the Ge ion implantation process. Controlling the production quality and debugging of large integrated circuits are difficult due to the inability of conventional wafer scale testing techniques to measure individual devices or subsystems. The erasable optical input and output can help to develop an autonomous wafer scale testing method with sufficient flexibility to develop comprehensive testing procedures.

The structure of implanted grating coupler with etched grating couplers as input/output are shown in Figure 2.5. The periodic refractive index changing region is created via Ge ion implantation process. The peak coupling loss for each coupler is ~5.5dB. After testing, the amorphous segments of this device will be annealed and this implanted grating structure is removed, which avoid inducing additional optical loss into the whole photonic circuit. The residual optical insertion loss of erased grating coupler in the original photonic circuit is approximately -25dB. However, the gratings were fabricated within taper structures to enable commercial wafer scale testers to locate them, resulting in relatively large in-line structures (of the order of 160µm per grating. If multiple gratings are required, their size can significantly enlarge a photonic circuit. Nevertheless, they represented a significant step forward in photonic wafer scale testing technology.

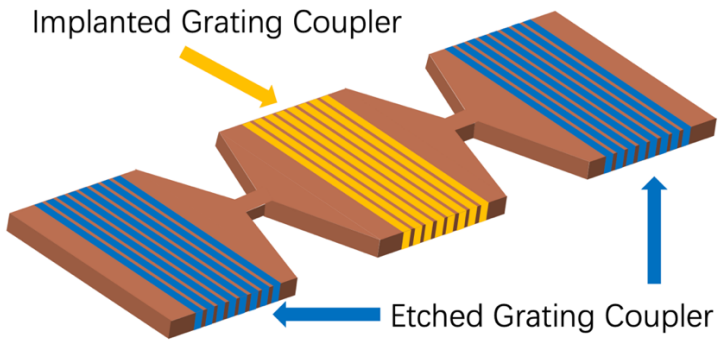

Figure 2.5 - The structure of implanted grating coupler and etched grating couplers in photonic circuits [101].

2.2 Post-fabrication trimming

Post-fabrication trimming is necessary to correct the working performance of photonics components affected by the imperfect fabrication processes. For some devices with high

sensitivity to fabrication variations, such as ring resonators and MZI, the resonant wavelength and transmission can be easily affected by the dimensional shifts of device structure (e.g. waveguide width), caused by fabrication variations. For the applications including modulation and sensing, the resonance of ring resonators is required to be located at specific wavelengths. The performance of the devices on the same wafer, or even on the same chip can vary due to the difference in etching width, etching depth, implantation dose etc. However, in large-scale integrated photonic circuit, each device is designed to work at a particular operating point, for the whole photonic circuit to achieve the predefined functionality. Therefore, post fabrication error correction (trimming) is highly desirable.

2.2.1 Conventional post-fabrication trimming methods

The effective index of a propagating mode relies on the refractive index of waveguide material as well as the cladding media. The refractive index of a cladding layer, such as SiO_2 for the SOI platform, can be shifted by electron-beam induced compaction and strain. Figure 2.6 gives the simulation profile of refractive index change of silicon waveguide affected by e-beam irradiation on cladding media [66]. The volume compaction in the top and sidewall SiO_2 are created by 2 keV electron irradiation. This will lead to the increase of strain in the silicon waveguide, as well as the refractive index. Therefore, the effective index is also increased and finally this method provides a resonance red shift of 4.91nm in a ring resonator, which is shown in Figure 2.7 [66].

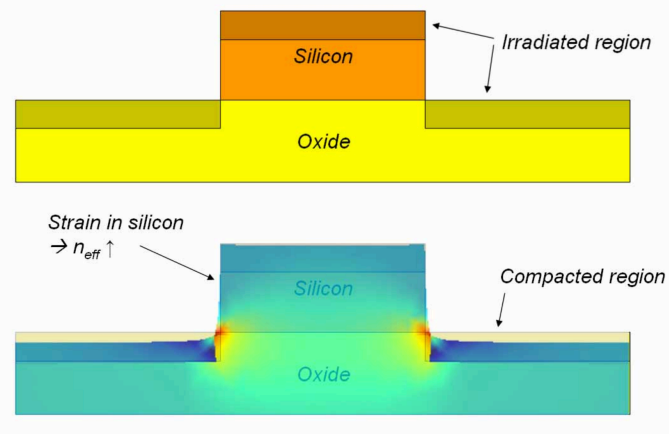

Figure 2.6 - Cross section of the silicon ring resonator affected by e-beam irradiation [66].

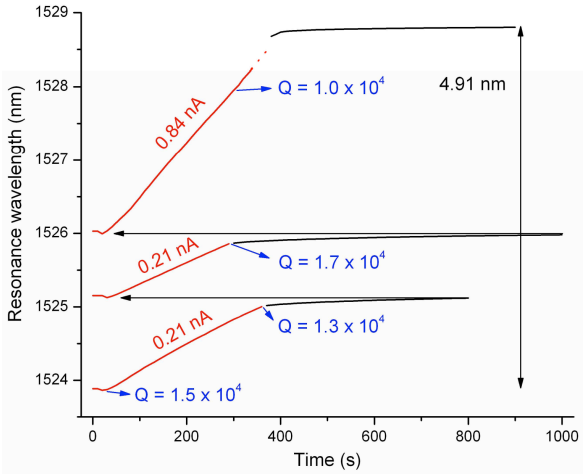

Figure 2.7 - The resonant wavelength changing in trimming process [66].

A similar principle is used to trim a silicon ring resonator with a chromophore-doped guest host polymer cladding. The structure of such a device is shown in Figure 2.8. The high-energy e-beam can lead to bleaching of the chromophore molecules, which results in a reduction of cladding refractive index. Therefore, the effective index of the mode propagating in the silicon waveguide can also be shifted. The resonant wavelength was trimmed towards blue end of the spectrum with a shift of 16.4nm for TM polarization and 4.3nm for TE polarization [67].

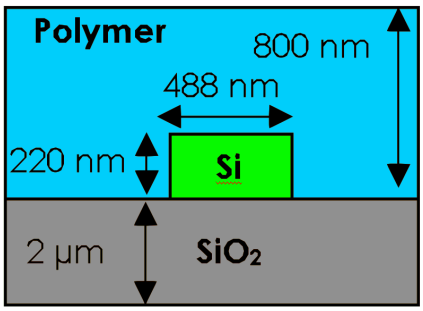

Figure 2.8 - Cross section of ring resonator waveguide under polymer cladding [67].

In addition to the e-beam, the ultraviolet light can also be used in trimming of ring resonators. In the study by Linjie et al., the cladding material around the silicon waveguide is polymethyl methacrylate. This design can provide low sensitivity to temperature changes and a resonant wavelength shift of 0.5nm was reported, shown in Figure 2.9, which can be achieved for a cladding layer irradiated with UV light [68].

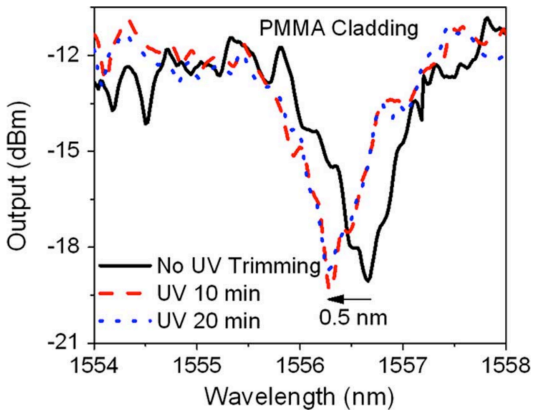

Figure 2.9 - Resonant wavelength changing under UV light trimming [68].

In the study of Antonio et al., the cladding media around the silicon waveguide was changed to a thin layer of A_2S_3 glass. Under the radiation from visible light, the resonant wavelength can be permanently shifted by 6.7nm, corresponding an effective index increase of 0.016 [69].

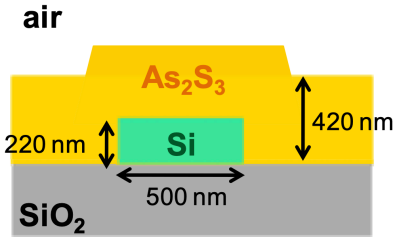

Figure 2.10 - Cross section of ring resonator waveguide under A_2S_3 glass [69].

Whilst these approaches to trimming clearly work, these cladding materials mentioned in the above-mentioned trimming methods are lacking universal CMOS compatibility and have the risk of inducing additional contamination into integrated circuit fabrication facilities. In 2013, a femtosecond laser was used to create a thin amorphous layer on the conventional crystalline silicon waveguide [102]. The effective refractive index of the waveguide was therefore changed after this process. The resonance shift in this method is only 1.7nm and it is difficult to accurately control the laser power to realize amorphization and avoid ablation of waveguide, which has potential to cause more optical loss in the irradiation area.

2.2.2 Post-fabrication trimming methods using ion implantation and annealing

After the investigation of erasable grating couplers mentioned in the former section, the ion implantation and laser annealing process were shown to provide the ability of changing the effective refractive index of silicon waveguides in optical devices. These techniques were also used to develop the post-fabrication trimming of ring resonators as well as MZIs [103, 104].

Figure 2.11 illustrates the schematic of an MZI with Ge ion implantation sections in both arms. Different lengths of implanted segments can modify the phase difference between the two arms.

When a 488nm continuous wave Ar laser was used to anneal the implantation area, the length difference of the amorphous sections between the two arms was changed. This results in the control of the phase difference, and hence the operating point of an implanted MZI.

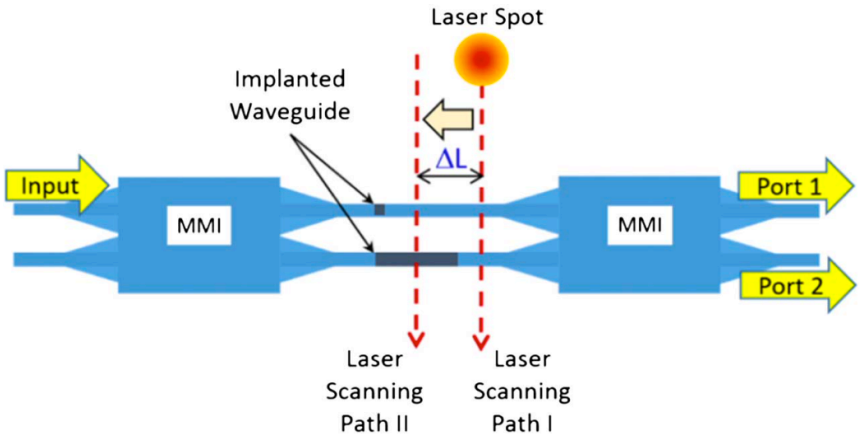

Figure 2.11 - Schematic of the implanted MZI and the scanning route of annealing laser spot [103].

The objective lens affects the diameter of the laser spot, and a small size of scanning laser spot can provide high annealing accuracy of an implanted area. The experimental setup will be introduced with more details in the chapter 5 of this thesis. Figure 2.12 shows the transmission shift of implanted MZIs during the annealing process. The amorphous section is gradually annealed by a laser, and therefore the transmission of MZI can trimmed. The highest transmission of the drop port output that can be achieved is over 90%. The effective index changes by 0.19, for the fundamental TE mode, and is achieved after the amorphous region was fully annealed (in this case). Based on the measurement results, the phase change brought by 1µm implantation difference is around 0.78 rad. Because the positioning resolution of a commercial motor can achieve 100nm. The trimming accuracy can potentially be 0.078 rad with active feedback control.

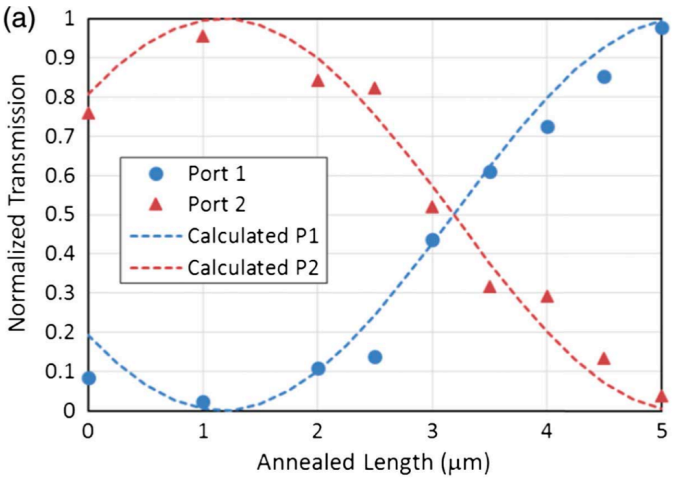

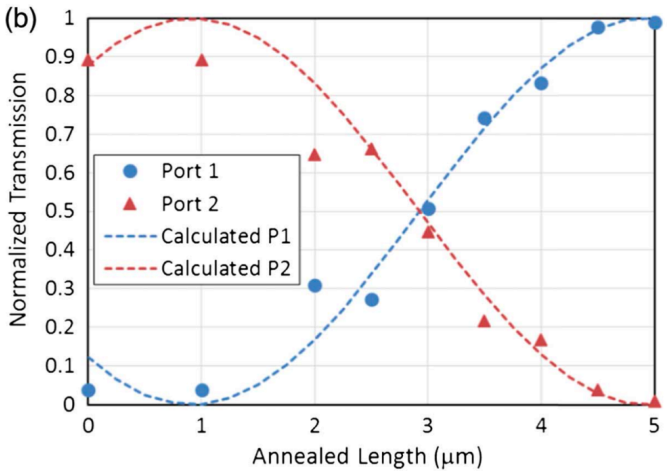

Figure 2.12 - Normalized optical transmission of the output ports of two MZIs during the annealing with 20× objective lens [103].

The same techniques were also used to realize post-fabrication trimming of silicon ring resonators. By inducing different lengths of implanted sections in the ring waveguide, the resonant wavelength of the same designed ring resonator is different, which is shown in figure 2.13.

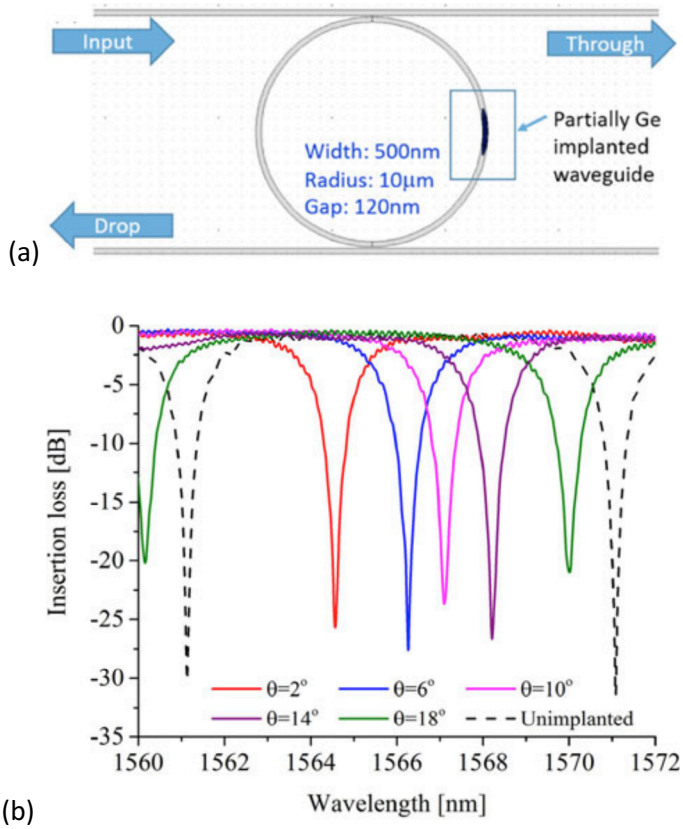

Figure 2.13 - (a) Schematic of a ring resonator with implntation section. (b) Transmission spectra of fabricated ring resonators with different length of implanted setions [104].

In Figure 2.13 (b), an umimplanted ring resonator with the same design and dimensiosn is also shown for comparison. The Ge ion implantation process induced the lattice damage into silicon lattice and result in the rise of refractice index. The longer implantation sections can provide

greater red shift of resoance wavelength. The largest shift, over 9nm, of a ring resonator with 10µm radius is achieved by an 18° implantation arc length section. The tranmission, before and after laser annealing, of this device is shown in figure 2.14. The resonance was shifted from 1571.5nm to approximately 1564.9nm after the amorphous section is fully annealed. The power of annealing laser was approximately 90mW while the diameter of laser spot was 4.7µm. The largest trimming range that this method achieved was 10nm, while the free-spectural range (FSR) is also approximately 10nm. This trimming range is sufficient for most of applications [64]. But in principle, any length of implanted waveguide could be trimmed.

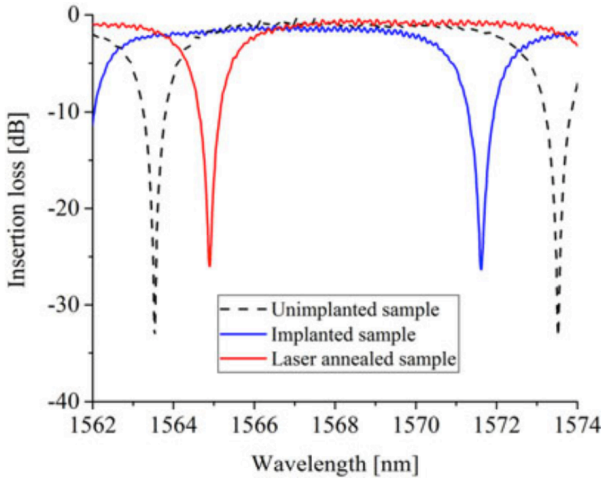

Figure 2.14 - Transmission spectra of 10µm radius ring resonator with 18° implantation section before and after annealing [104].

In 2017, Knights et al., ultilized the boron difussion process and post-fabrication heating to achieve trimming of the resonant wavelength of a ring resonater [105]. The cross-section of their doped ring is shown in figure 2.15. The centre part of waveguide is doped as p type while the two heavily doped p type area are also formed at 750nm from the waveguide edge. These two p++ area act as the contact area for the electrical voltage and the p area in the middel acts as the ohmic heater. After electrical power was applied on these areas, the refractive index of the centre waveguide was changed with the diffusion of boron from the heavily doped contact regions. A permanent blue shift of 240pm was measured for a ring resonator with 30µm radius. In figure 2.16, the navy curve represents the spectrum of the doped ring resonator after fabrication. After 20V bias for 120 minutes, the resonance shifted to the purple curve. In this experiment, the boron dopant will cause the generation of free carriers in the silicon waveguide, which results in additional absorption loss of the optical signal. In addition, the diffusion process will cause less lattice defects than ion implantation, and therefore less refractive index change is achieved. For realizing a longer trimming range than 240pm, more insertional loss will also be induced.

Furthermore, trimming one device took 120 minutes, which is unrealistic for commercial processes. Therefore, this is not a promising method for mass production.

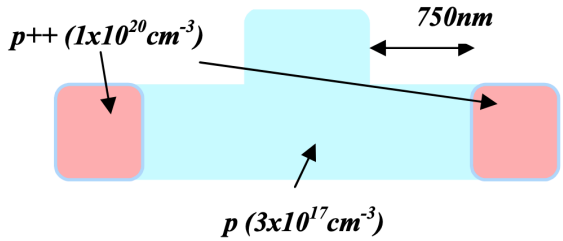

Figure 2.15 - Cross-section of boron doped ring resonator [105].

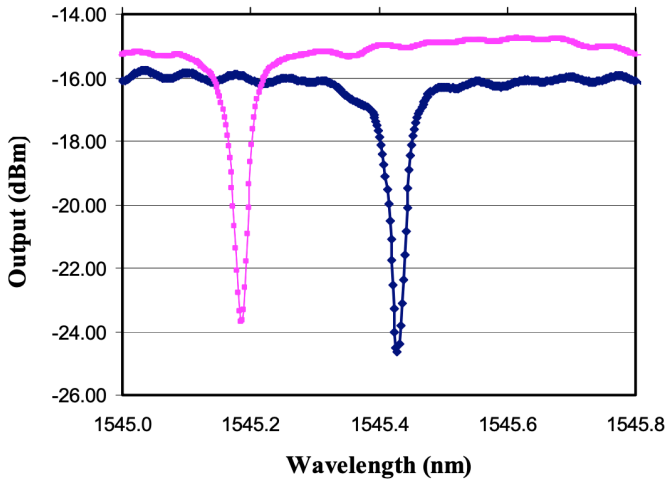

Figure 2.16 - Measured blue shift of resonant wavelength [105].

In 2019, Hagan, Torres-Kulik and Knights use boron ion implantation to create lattice defects in silicon waveguides [106]. The cross-section of an implanted ring resonator is shown in figure 2.17. The annealing process was carried out via an integrated TiN heater fabricated on top of implanted waveguide. The measured resonance shift of this ring resonator and effective index change under different implantation doses are shown in figure 2.18. It demonstrates that higher implantation dose can bring more lattice damage and result in a greater trimming range. However, the boron ion implantation can only bring limited refractive index change of a silicon waveguide. The demonstrated final trimming range of the resonant wavelength was only 380 to 800pm. The extinction ration also doubled after electrical annealing, demonstrating significant optical loss prior to annealing. Therefore, similar to the former experiment in 2017, the additional insertion loss brought by a boron dopant cannot be ignored.

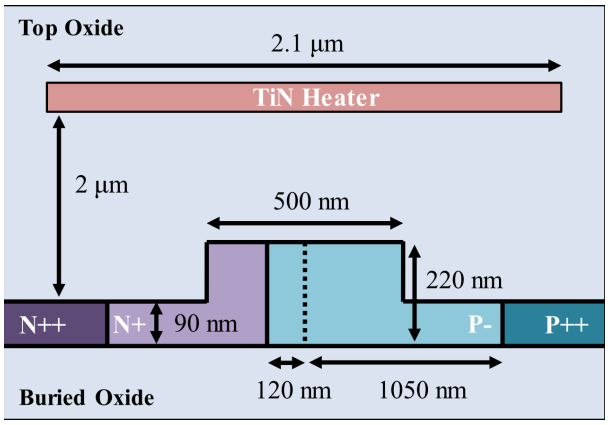

Figure 2.17 - Cross-section of implanted ring modulator [106].

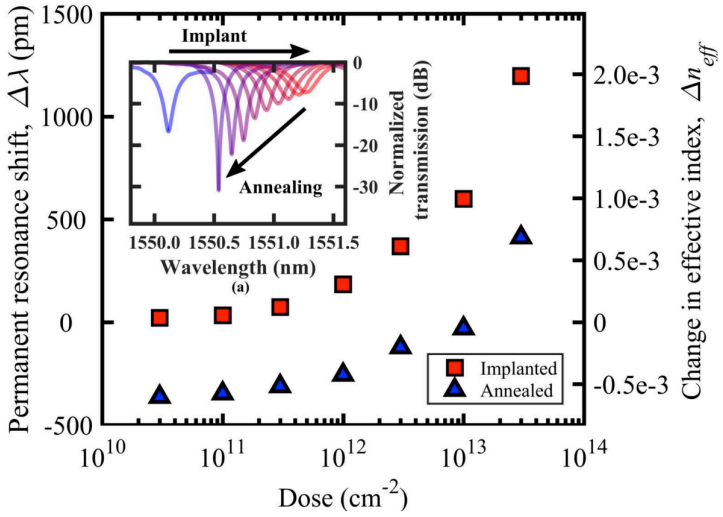

Figure 2.18 - Resonance shifts and calculated change in effective index achieved as a function of implanted defect dose [106].

In 2021, Jayatilleka et al. ultilised similar techniches used in this thesis to realize post-fabrication trimming [107]. An additional Ge ion implantation layer was fabricated on and around the waveguide, which is shown in figure 2.19. After applied eletrical power onto the tungsten heater, the lattice defects created in implantation process can be reversed via thermal annealing. In figure 2.20, over 8nm trimmable range is achived for the ring resonator with an FSR of 6.8nm. By precisly controlling the applied electrical power from the tungsten heater and the annealing time, the trimming accuracy for a range of devices on a whole wafer is controlled to $\pm$32pm.

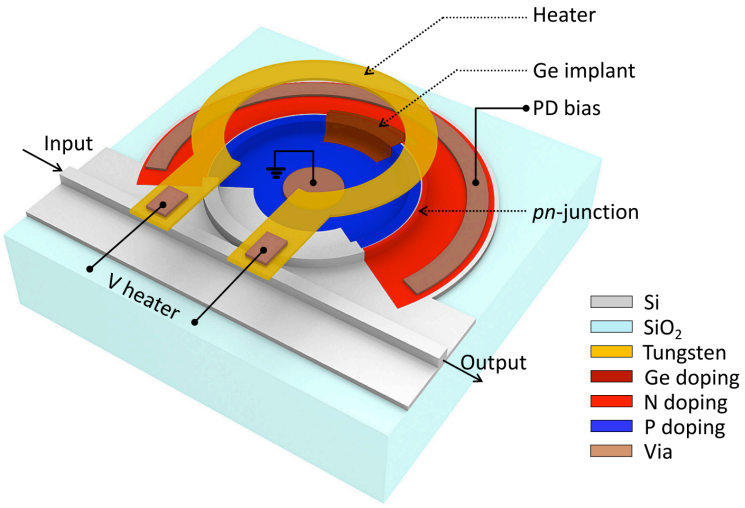

Figure 2.19 - Silicon microring modulator formed by a rib waveguide with a pn-junction, a Ge implanted section and a tungsten heater on top [107].

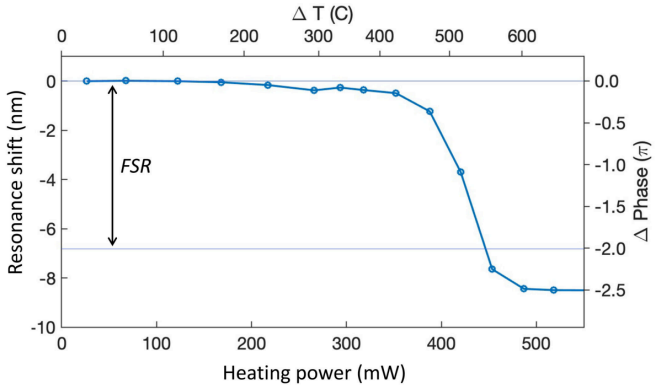

Figure 2.20 - Measured resonant wavelength shift as a function of the applied electrical heating power [107].

2.3 Tuneable optical coupler and programmable photonic circuits

Compared with application-specific photonic integrated circuits, the flow of an optical signal is more flexible in programmable photonic circuits, and can be manipulated after fabrication and packaging via circuit programming. The target of programmable photonic circuits is realizing a common optical hardware solution for a variety of functions and applications. The electrical signal from the software is applied to a tuneable optical coupler and the light can therefore be rerouted. The most essential concepts in the hardware level of programmable photonic circuit are the basic building blocks and the architecture of waveguide meshes.

2.3.1 Tuneable optical units

The basic building block for programmable photonic circuits is a 2×2 tuneable photonics coupling component, which can provide a variety of power coupling ratios independently. Normally, the incoming optical signal is launched into two input ports and transferred by phase shifting to two output ports. In this section, the tuneable basic units fabricated from three common structures are introduced, including MZI, directional couplers.

Figure 2.21 shows three transmission modes of 2×2 optical tuneable units. For each input signal, it can be ideally distributed from 0% (fig. 2.21a) to 100% (fig. 2.2b) at the output ports if all elements in this unit are lossless. Figure 2.21 (c) gives a middle state of (a) and (b). These three states are called the bar, cross and partial states [70].

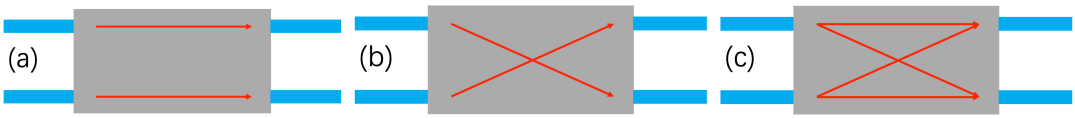

Figure 2.21 - Three transmission modes of 2×2 tuneable optical units: (a) bar, (b) cross, (c) partial.

Directional couplers are the simplest 2×2 tuneable optical unit that consist of two waveguides fabricated in proximity. The optical signal launched in one of the input waveguides can be transferred or partially coupled into the other waveguide. The distribution of output power is controlled by designing the coupling length between them, and the waveguide separation. This transmission behaviour meets the requirement of tuneable basic units in programmable photonic circuits. The thermo-optic effect is typically used to control the coupling efficiency and optical intensity distribution [108, 109]. A thermal heater is fabricated on top of the coupling region. However, only the intensity of the optical signal can be modulated in this situation. The phase information is also a key parameter for both tuneable units and whole integrated photonic circuits. Therefore, a phase shifter located in the output waveguide is designed to realize control of phase delay in the optical signal, which is shown in Figure 2.22.

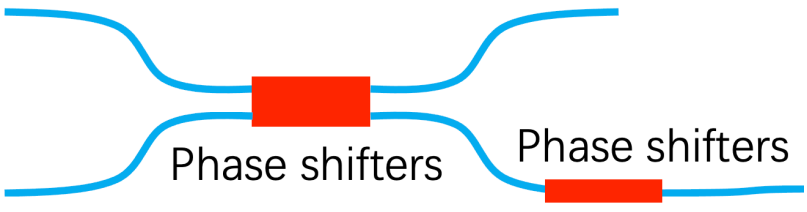

Figure 2.22 - Sketch of tuneable directional couplers.

The MZI is also a common implementation for 2×2 optical structure. The coupler at the input and output in the MZI provides a 3dB function, to equally divide and recombine each input signal into the two arms of the MZI. The structure can be used for this fixed 3dB coupler are multimode

interferometers, directional couplers and Y splitters [69-71]. Based on the same requirements of controlling the intensity and phase of output optical signal, two phase shifting elements should be induced into the conventional MZI structure (one in each arm), which are shown in Figure 2.23. The optical phase shifter inside of the MZI adjusts the final intensity and phase of optical signal emerging from the MZI, while the optical phase shifter outside of the device can be controlled via additional phase shifters in the output waveguides.

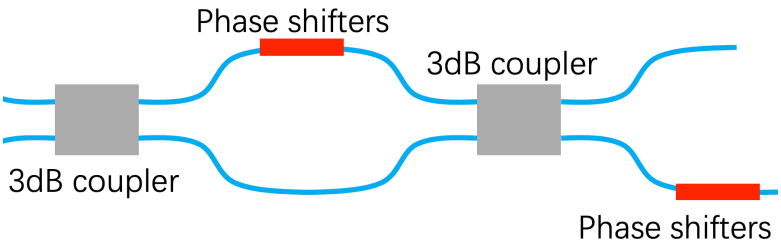

Figure 2.23 - Sketch of tuneable MZI.

In addition to basic optical structures, microelectromechanical system (MEMS) devices have also been reported for use in photonic integrated circuits [110]. Different from the thermo-optic effect mentioned before, the optical properties of photonic MEMS devices are changed by electromechanical behaviour of suspended structures. For example, in a directional coupler, the distance between two waveguides can be changed and the relative position of waveguides can be moved, which all result in the alteration of coupling efficiency [111, 112]. This approach requires a lower power drive than the operation of thermal heaters. Even through, the tuning speed is limited by mechanical resonance frequencies, it is still a competitive solution for programmable photonic circuits at low tuning speed.

Similar to the methods mentioned in the post-fabrication trimming section, the phase changing materials can also be used to fabricate the tuneable optical units in programmable photonic circuits. Carlos et al. report the design of integrated all-photonic non-volatile memory in 2015 [113]. The phase state of y $Ge_2Sb_2Te_5$ can be changed by ultrashort laser pulses. Then the effective index of optical mode in the silicon waveguides can be shifted due to the near-field effects. The switching energy was 13.4 pJ at the frequency of 1GHz. Recently, chalcogenide phase change materials, Sb_2Se_3 and Sb_2S_3, have also attracted researchers' attention when it was demonstrated that these phase change materials were used in tuneable photonic components [114-116]. These materials have advantages of ultralow-loss and lower switching temperature of lattice states. In both crystalline and amorphous states, the materials exhibit ultra-low intrinsic absorption losses ($k < 10^{-5}$) over the telecommunications communication band at 1550nm. The switching temperatures, from amorphous to crystalline, are 200°C for Sb_2Se_3 and 270°C for Sb_2S_3. The real part of refractive indexes of these two materials are closer to silicon than $Ge_2Sb_2Te_5$. This provides better mode match with silicon photonic platform. However, chalcogenide phase change

materials are not CMOS compatible, and the switching process was achieved by laser annealing. Laser annealing is not achievable after the post-package process of devices. Therefore, this solution is not compatible with further integration with electrical circuits. Furthermore, repeated phase changing can degrade performance.

2.3.2 Waveguide meshes

The architecture of waveguide mesh decides the flexibility of optical propagation in the circuits. There are two broad classes which are defined by the direction of optical propagation: (1) forward and (2) recirculating [70]. The forward-only photonic circuits can only allow the optical propagation from one side of the mesh to another side. In the recent studies, two shapes, including triangular and rectangular, of forward waveguide meshes have been used to build optical networks [117, 118]. Figure 2.24 gives a schematic of a 5×5 triangular unitary circuit which consists of five input/output waveguides, ten 2×2 tuneable optical units and ten optical power detectors. In this example, tuneable MZIs are shown as examples in this circuit. Due to the fabrication non-uniformity and errors, the performance of each MZI will also vary. Therefore, the calibration for the initial operating of each tuneable unit in the whole circuit is significant for precisely realizing the final function. By adjusting the two-phase shifters mentioned in the former section 2.3.1, the transmission of each MZI can be trimmed. By monitoring the optical signal of D11 to a minimum value, MZI11 can be tuned to the maximum output to MZI12, while the optical signal was launched into input waveguide 5. The following devices, MZI12 to MZI14 on the same diagonal, can also be subsequently trimmed to the same operating state by repeating a similar process. In this situation, all the input optical power from waveguide 1 to 5 can be coupled into output waveguide 1. The second diagonal layer, coloured as yellow in Figure 2.24, will be further tuned when detector D11 to D14 have the maximum value. Since the optical signals for the inner diagonal layers all come from the former detectors, it requires that as much as optical power as possible is passed to the next layer, which needs these detectors to be almost transparent.

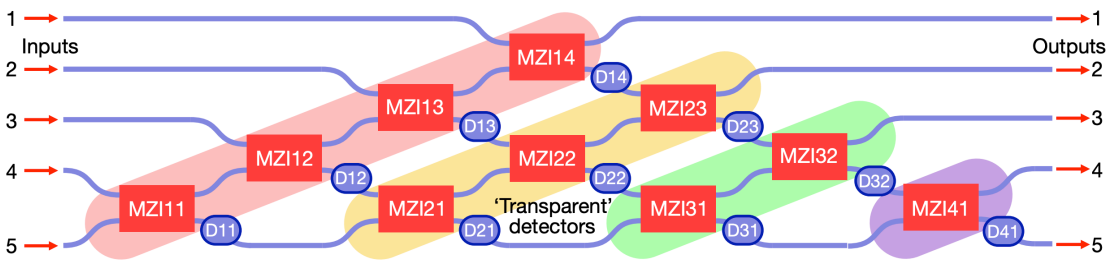

Figure 2.24 - Triangular architecture of waveguide mesh [70].

To minimize the total optical loss brought in by the detectors located between each layer, the alignment starts from the MZI14 with no detector operation. The optical signal launches out at the output waveguide 1 can be trimmed to minimum value, which means most of optical power is

transferred to the MZI23. By repeating this process, MZI23, MZI32 and MZI41 can be optimized by using output waveguides 2 to 4. Based on these three working states mentioned in the section 2.3.1, these MZIs can trimmed to the cross state. Due to the symmetrical design of each MZI, devices MZI14 to MZI11 can be trimmed to the bar state by using the output waveguide 1. MZI13 therefore can further been turned to the bar state while the optical signal is launched from input waveguide 3 and MZI12, MZI14 are all working at the cross state. By repeating the former process, the basic tuneable units in this circuit can be aligned to bar and cross states as required.

The outputs at right ports are defined by the working state of these tuneable optical units. Assuming that all the MZIs worked initially at bar state, the optical signal from input 1, 2, 3 and 4 can be detected at output 1, 2, 3 and 4 respectively. By changing the MZI14 to cross state, the optical signal at output 1 and 2 can be switched. While the output 3 and 4 has no change. By further controlling work states of all the MZIs in this circuit, more routings of optical propagation can be achieved in this circuit.

The rectangular mesh structure shown in the figure 2.25 can also realize the arbitrary unitary transmission matrix. However, the alignment of this shape of waveguide mesh must be carried on with the help of in-built optical detectors. There is a power monitor after each of tuneable MZI. For example, a directional coupler on the waveguide between MZI11 and MZI31. MZI11 is firstly calibrated to bar state. Then MZI31 can be tuned to bar or cross state by monitoring the optical power from output 1. Similar calibration processes are carried out for MZI22 and MZI42. When MZI31 work as cross state, MZI41 can be calibrated by detecting optical power from output 2 and 3. The rest of MZIs can be further calibrated. Similar with the triangular architecture circuit, the output situation can be tuned by adjusting the state of each MZI. The advantage of this rectangular circuit is that it have more compact structure and shorter length than triangular circuit.

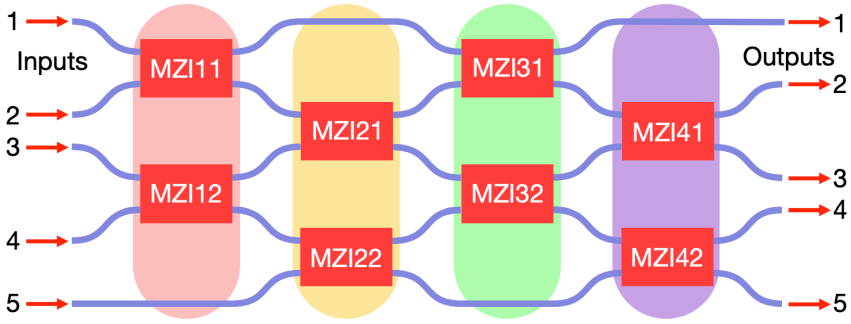

Figure 2.25 - Rectangular architecture of waveguide mesh [70].

Different to the forward-only mesh, the recirculating mesh has the possibility to be programmed as loops, while the basic building concept is still a waveguide mesh and 2×2 tuneable optical couplers. In this architecture, the route of light can be programmed to any direction in the mesh.

Compared with the forward mesh, this structure allows the optical length as the integer multiple of segments, which can potentially achieve the functions of wavelength filtering. However, higher optical loss is induced by longer optical path and more passed tuneable couplers that are used to achieve the same function.

The recirculating mesh in recent studies consist of different topologies, such as triangular, square and hexagonal. Schematics of these structures are shown in the figure 2.26. For each kind of topology, many factors should be evaluated, including the footprint of realizing the target functions, additional optical losses induced after programming, and the reconfigurable ability. In 2015, Zhang et al. utilizing a square architecture waveguide mesh achieved the optical filtering function with an extinction ratio of 55dB [119]. A Hexagonal mesh has an attractive advantage that is all ports can be used as input and output and it can be programmed as a forward-only mesh [70]. Although this waveguide mesh can provide more flexible programming ability, higher optical losses will also be induced. In 2017, Pérez et al. experimentally demonstrated a recirculating and programmable waveguide mesh that are made from seven-unit cells. Over 20 different functions have been realized and applied in different fields such as optical communication, sensing, signal processing and quantum information systems [120]. Two year later, Pérez et al. used a DC based triangular waveguide mesh to demonstrate a programmable beam splitter with a small device footprint [121].

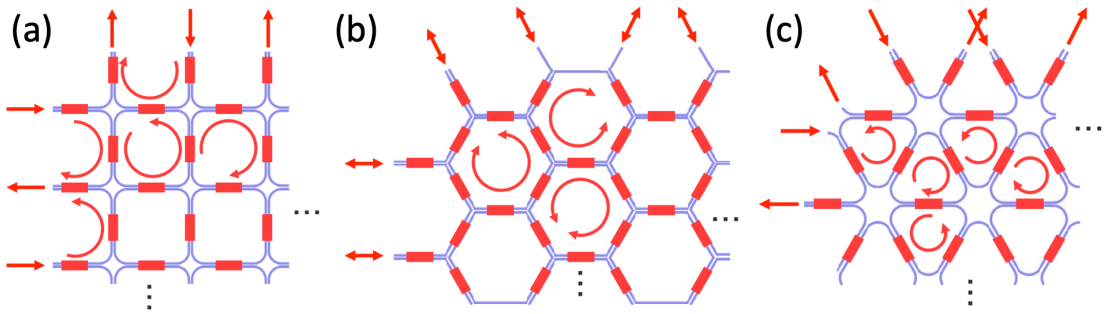

Figure 2.26 - Sketches of loop waveguide mesh with (a) square, (b) hexagonal and (c) triangular topologies [70].

2.4 Summary

This chapter firstly reviewed the literature describing coupling methods for wafer-scale testing. Grating coupling with fibre is the most popular solution to form the testing probe, providing flexible, fast and accurate wafer-scale testing for photonic industry. For improving the residual insertion loss brought by testing probes in PICs, and providing capability for comprehensive testing, an erasable grating coupler was introduced. However, erasable grating coupler will still

result in a large footprint when optical signals are tapped out from the intermediate parts of photonic circuits.

After discussing wafer-scale testing, several post-fabrication trimming methods were introduced. These techniques can also help to increase the yield and decrease the cost of fabrication of PICs. Among them, the trimming process realized via Ge ion implantation and annealing process can bring large trimming range of optical devices and this method is CMOS compatible.

Finally, the development of programmable photonic circuits was reviewed, including three different structures of basic tuneable optical units and two main architectures of waveguide meshes.

Based on these reviews, a tuneable device can be the most fundamental component in these applications. This has also become the motivation to develop the project in this thesis.

Chapter 3 Theory

In this project, the refractive index can be shifted by the ion implantation and laser annealing. During these processes, the transmission of optical devices can also be altered. This chapter firstly introduces the theory of ion implantation and laser annealing. The fundamentals of optical waveguides and devices used in this project are also discussed.

3.1 Amorphisation induced via Ge-ion implantation

This section introduces the basic knowledge of ion implantation and its effect, which is to increase the concentration of lattice defects. This disorder effect in the silicon lattice is the starting point of this project. The refractive index of the silicon waveguide and performance of optical devices are therefore changed due to this disorder.

3.1.1 Ion implantation

Ion implantation is a micro/nano fabrication process that allows ions to be accelerated towards, and implanted at a depth within the target silicon wafer. The energy of the implanted ions is rapidly (on the femtosecond timescale) transferred to the target wafer by a combination of nuclear and electronic collisions, which are stochastic in their nature. In the semiconductor and photonics industry, this process is mainly used to introduce dopants into silicon, which has almost replaced thermal diffusion processes. The key parameters of ion implantation include ions elements, dose of ions and ion implantation energy. For different applications, the element chosen results in different properties.

For building N type and P type doping areas to change the concentration of carriers and electrical property, such as in the CMOS transistors and silicon photonics modulators, ions of elements from group V and III are respectively used as dopants. Typical ion implantation energies and doses are 10 to 200 KeV and 10^{11} to 10^{16} ions/cm^2, respectively. The implantation energy and the mass of ions can significantly affect the stopping distance, or “projected range” of the implanted ions. A relatively large accelerating voltage transfers a large kinetic energy to the ions, resulting in a longer projected range or deeper implantation depth for most of the implanted ions. The time integrated ion beam current determines the impurity dose or concentration of the implanted ions and the area over which this dose is delivered is determined by the areal scan rate of the ion beam.

A typical ion implantation process is depicted in figure 3.1. Figure 3.1 (a) shows ion implantation into the silicon (grey) and mask (light grey). The mask can protect the bottom part of the sample and stop the ions traveling within it. A photoresist layer is the most common soft mask for this process, while the oxide, nitride and polysilicon are typically used as hard mask materials, when resistance to greater penetration depth is required. In figure 3.1 (b), R_p represents the projected range, or mean stopping distance of the implanted ions. The stochastic nature of the process means that the implanted ions are distributed about Rp with a deviation, ΔR of the range, which is known as the "straggle". Based on a rule of thumb, the ion concentrations, at positions $R_p \pm 2\Delta R$ and $R_p \pm 3\Delta R$ are approximately 10% and 1% of the peak concentration (at R_p) [122].

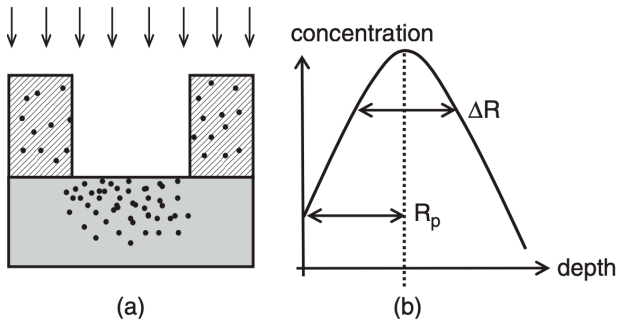

Figure 3.1 - (a) Depiction of selective area ion implantation of the underlying target substrate, using a blocking mask layer; (b) ion impurity concentration profile in the target wafer [122].

However, ion implantation is a relatively high energy process compared with thermal diffusion. Lattice damage will be created and left in the sample after the implantation. During the ion implantation process, the energy of the implanted ions will be dissipated through electronic stopping and nuclear stopping. Electronic stopping is the process in which energy is transferred to electrons and ultimately producing heat. Nuclear stopping is an elastic interaction process and can be described by kinematic theory, which result directly in lattice defects in crystals if the nucleus receives sufficient recoil energy (i.e. an average of 24 ± 2 eV for silicon) [123].

Point defects in the implanted crystal lattice can be specifically divided into three major types. In figure 3.2, the lattice substitution, interstitial and vacancy point defects are shown. The lattice substitution happens as the atoms are removed from the lattice and replaced by the implanted ions. Vacancy defects occurs when atoms of the sample are removed, and no implanted ions replace them. The interstitial defect is caused by an atom, either implanted or native lattice, occupies non-conventional space in the lattice. More complex defects are developed from these basic point defects, such as Frenkel pair defects which are the combination of the vacancy and self-interstitial point defects [124].

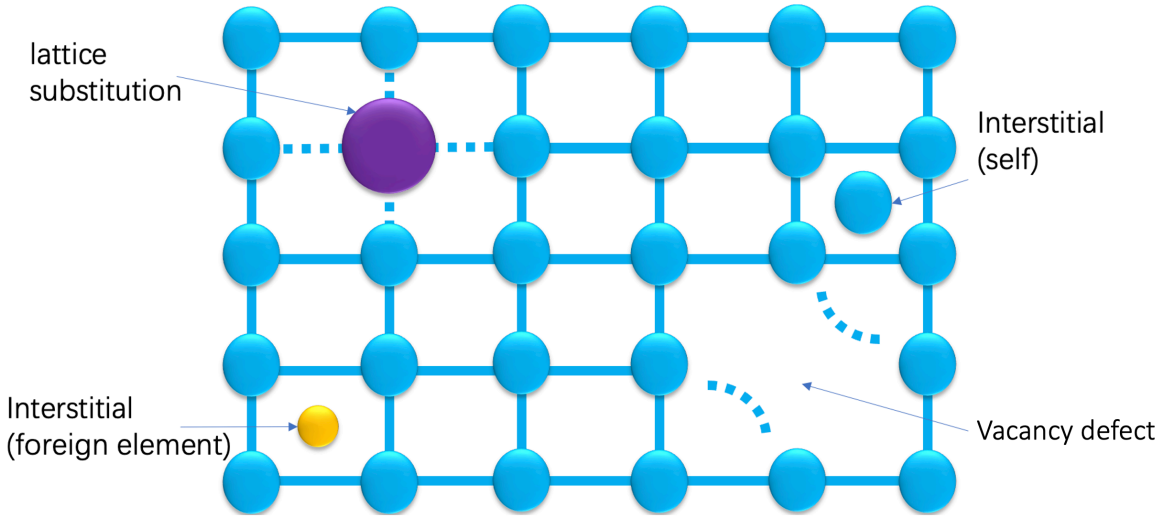

Figure 3.2 - Points defect in crystal lattice after ion implantation.

3.1.2 Refractive index

Refractive index is used to describe the speed of light travelling through the material, and it is defined as:

$$n = \frac{c}{v} \tag{3-1}$$

where c is the speed of light in vacuum and v is the phase velocity of light in the medium. Therefore, greater refractive index means the slower the speed that light will travel at, in the medium. The introduction of refractive index usually starts from the reflection equation between two media, incorporating the angle of incidence and the angle of reflection. However, the refractive index is the parameter to describe the property of a medium. Therefore, for better understanding how the implantation process affects the refractive index, we can start with the equation of complex refractive index.

$$n' = n_R + jn_I \tag{3-2}$$

The real part n_R, dominates the travelling speed of light in the medium. The imaginary part n_I, also called extinction coefficient, represents the attenuation of light travelling through the medium. For example, the electromagnetic waves in the vacuum can be described as:

$$E(t,x) = E_0 exp[-i(wt - kx)] \tag{3-3}$$

Whilst propagating in the medium with the complex refractive index mentioned before, equation 3.3 can be modified as:

$$E(t,x) = E_0 exp(-n_I kx)[-i(wt - n_R kx)] \tag{3-4}$$

We can see that the refractive index will affect the light when travelling through the medium. The speed of light in the medium is affected by the interaction between light and particles in the medium. This results in a longer time that light will travel through a fixed distance in the medium than the vacuum. Therefore, at the macro level, the light travels “slower” when passing through the medium. The refractive index of amorphous silicon is greater than crystalline silicon [125]. This means that the light will travel slower in the silicon waveguide with more defects.

The absorption in silicon is dominated by two types: band edge absorption and free carrier absorption. For silicon waveguides, the effect of edge absorption is negligible under a suitable wavelength range (for example, a wavelength of 1520 nm has an intrinsic loss of 0.004dB/cm) [126]. Doping in the silicon can generate the free carriers. However, the raised concentration of free carriers will increase the absorption of light. This property can be described by famous Drude-Lorenz equation [127].

$$\Delta\alpha = \frac{e^3\lambda_0^2}{4\pi^2 c^3 \varepsilon_0 n}\left[\frac{\Delta N_e}{\mu_e (m_{ce}^*)^2} + \frac{\Delta N_h}{\mu_h (m_{ch}^*)^2}\right] \tag{3-5}$$

Scattering, which will also cause the optical loss, in the optical waveguide is described as two types: volume scattering and interface scattering [1, 5, 128]. The interface scattering is caused by the roughness at the interface between the core and the cladding materials. Volume scattering is due to the imperfections of the waveguide material itself, such as defects. Therefore, the defects induced by the ion implantation process will increase the optical loss of implanted silicon crystalline waveguide.

For semiconductor materials, such as Si, the refractive index also varies with the wavelength of light. Crystalline silicon has a refractive index of 3.48 at the communication wavelength of 1550nm. A range of techniques can be used to change the refractive index of silicon. A temperature shift can affect the refractive index. Optical modulators, optical switches and phase shifters are based on the property of this refractive index alteration. The thermo-optic effect can be used to change the refractive index of the silicon waveguide [129].

$$\frac{dn}{dT} = 1.86 \times 10^{-4}/K \tag{3-6}$$

3.1.3 Refractive index change by Ge-ion implantation

In this project, the refractive index of silicon is increased after the ion implantation. Based on the section 3.1.1, ion implantation can induce lattice defects in the silicon waveguide. These lattice defects in crystalline silicon will lead the electronic polarizability change, which is caused by the modification of the ion-ion couplings. A study from Baranova et. al describe the function of

refractive index change to the dose of a range of implanted elements, which is illustrated in the figure 3.3 [130].

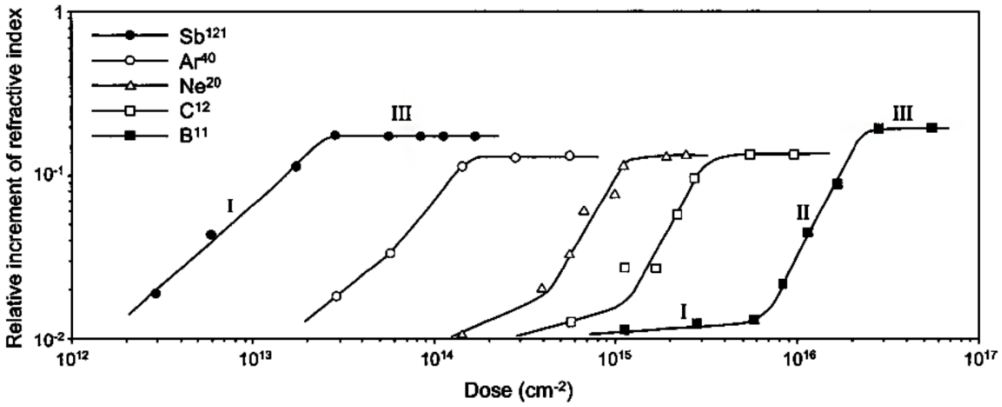

Figure 3.3 - Shift of refractive index in silicon introduced by different implanted elements [130].

In this project, we aim to achieve the largest shift of real refractive index via ion implantation process. The maximum values of refractive index change for those elements in figure 3.3 have very small differences. This suggests that the basic reason of this change has an independence from the implanted element. From the former discussion, the defects produced by the ion implantation are the main reason to increase the refractive index. Under the same implantation energy, heavier atoms can create more nuclear stopping as well as more defects. Therefore, atoms with heavier relative mass have a stronger effect to increase the refractive index even under situations of lower dose. The optical loss caused by implantation should also be minimised. To avoid generating additional free carriers in the silicon waveguides, Ge ions from group IV is an ideal choice for this project, as it is not an electronic dopant and has large relative mass.

3.2 Recrystallisation by laser annealing

Annealing is a common process to repair the lattice damage created by ion implantation and radiation in a crystal structure [131]. This technology is also used in the study of forming silicon optical waveguides in amorphous silicon. The basic principle of annealing is the thermal treatment for the lattice and recrystallization will happen as the temperature reaches the annealing point.

Laser annealing is the technology of using laser power to heat the sample and achieve the annealing effect. In the earliest study by Antonenko and Gerasimenko et al., laser irradiation was found that it could be used to repair lattice damage created by ion implantation in crystalline silicon and realise electrical activation of doped layers [132]. In most of the studies of laser annealing, two types of laser systems have been used: continuous wave (CW) lasers and pulsed lasers [133]. In CW laser experiments, the target area was illuminated and scanned by a laser spot with suitable size, while the pulsed laser can accomplish thermal treatment of the sample by one

single laser spot with larger size and higher density of laser power [134]. Therefore, the CW laser annealing is more suitable for thermal treatment of a large area under the laser power density 50 to 600kW/cm^2 [134]. However, some defects still cannot be repaired by the CW laser. The pulsed laser with the pulse width of nanoseconds scale can provide a better annealing effect as discussed below [135]. In this case, much higher power density is provided in a single pulse. For different sample materials, there are different thresholds of laser power density to achieve annealing, no matter for CW laser or pulsed laser. The lower limit of the threshold is the power density that satisfies the minimum temperature of the annealing process. The upper limit of the threshold is the power density that starts to lead the lattice damage. Therefore, in this project, the power of laser used for annealing should be finely controlled.

The basic physical mechanism of laser annealing of silicon comes from the energy transfer from laser to sample materials [135]. The effect of laser annealing is the result of melting of the surface layer and the liquid phase epitaxy during the cooling down of melted layer. When the sample is irradiated by a laser, the energy is transferred to the electrons at the surface layer. These electrons will be excited to the conduction band as free carriers if the energy of the photon hv is greater than the band gap of the sample. The production rate of free carriers Y_c is proportional to the irradiation energy. For silicon $R = 0.37(300K)$, $\alpha = 1.25 \times 10^4 cm^{-1}$, and assuming that the $I_L = 100mJ/cm^2(\lambda = 532nm,\ \tau_p = 15ns)$, thus $Y_{c0} = 1.4 \times 10^{29} cm^{-3}/s$ [136, 137].

$$Y_c \approx \frac{\alpha(1-R)}{hv\tau_p} I_L \exp(-\alpha z) = Y_{c0} \exp(-\alpha z) \tag{3-7}$$

The production rate of free carriers Y_c will decrease as the transmission depth z goes deeper. An electron-hole plasma is believed to be produced after the laser energy is absorbed by a solid material. Because the lifetime of free carriers is normally shorter than the laser pulse (1psec,), this plasma state will start to relax to a stable state. The relaxation process depends on the relation of actual density of carriers n_c. If the $n_c > 10^{29} cm^{-3}$, the relaxation process of the plasma state is firstly dominated by electron-electron collisions. The plasma energy will be transferred to secondary electron. Then excess electron energy transferred to the lattice via phonon collision. Therefore, the energy given by photons finally transferred to phonons in time scale that less than 1psec, and thus leading to the elevating sample temperature locally [136]. Figure 3.4 shows the temperature-time profile of several depths inside the amorphous silicon under the irradiation of pulsed laser power 1.5 J/cm^2 [133, 138].

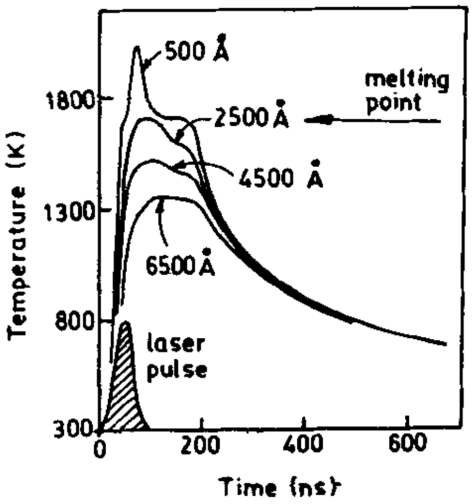

Figure 3.4 - Temperature change vs. different depth in amorphous silicon sample [133].

3.3 Photonics waveguide

3.3.1 Waveguide theory

An optical signal can propagate in a material as a transverse electromagnetic (TEM) field, and the electric and magnetic fields are perpendicular to the direction of propagation of the field. All the electromagnetic fields can be described by Maxwell's equations [1, 139]. A general optical waveguide used in the modern photonic circuits design can be described as the simplest slab waveguide in a three-layer structure, which is shown in figure 3.5. The light is guided in the middle waveguide layer with refractive index n_1. The thickness of the middle layer is *h*. The field propagates along the direction of the z-axis. To confine the light in the waveguide core, the refractive index of upper and lower cladding layers, which are n_2 and n_3, should all be smaller than n_1.

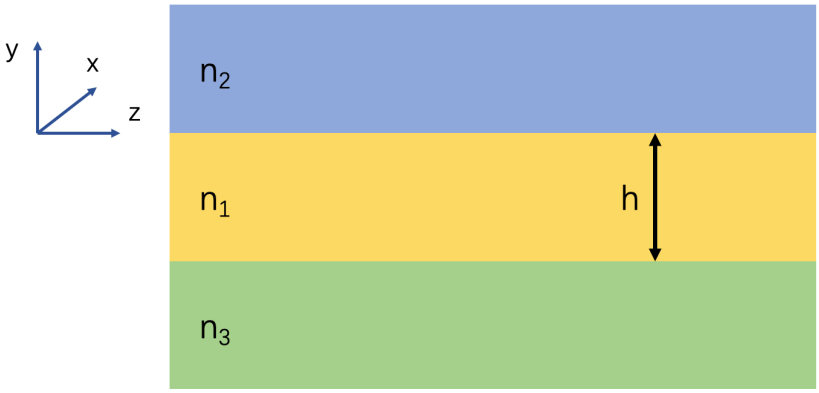

Figure 3.5 - Slab waveguide geometry.

Based on the ray model of slab waveguide, light should have total internal reflection at the interface of two layers when the angle of incidence greater than critical angle, which is shown in

figure 3.6. In the slab waveguide, the propagating light is only constrained at the y-axis. To form a mode in the waveguide, the wave must obey a standing wave condition in the y-axis, which means the total phase shift should be the multiple of 2π across the y direction. This is described as the following equation. θ represents the incident angle and λ is the wavelength of light. ϕ_{12} and ϕ_{13} is the phase shift at the reflection at the interface of the waveguide layer with top and bottom layers respectively.

$$2n_1 \cos\theta \frac{2\pi}{\lambda} h - \phi_{12} - \phi_{13} = 2m\pi, \quad m = 0,1,2,\ldots \tag{3-8}$$

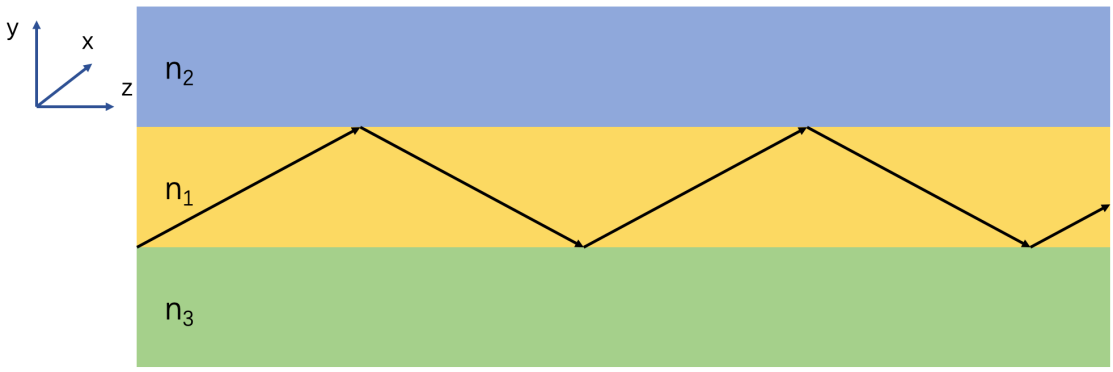

Figure 3.6 - Ray model of slab waveguide.

The electromagnetic wave propagating in the slab waveguide can also be described by Maxwell's equations. These electric and magnetic field distributions in the x-y plane are illustrated in following equations. The up one represents the transverse electric (TE) modes, while the bottom one represents the transverse magnetic (TM) modes. $E_x(y)$ and $H_x(y)$ represent the distribution of the x-axis polarised electric and magnetic field along the y direction. $k_0 = 2\pi/\lambda_0$ is the free-space propagation constant of light, while $\beta = k_0 n_{eff}$ is the propagation constant of light in the media. λ_0 is the free-space wavelength of light wave. n_{eff} is the effective index of the mode.

$$\frac{d^2E_x(y)}{dy^2} + [k_0^2 n^2(y) - \beta^2]E_x(y) = 0 \tag{3-9}$$

$$\frac{d^2H_x(y)}{dy^2} + [k_0^2 n^2(y) - \beta^2]H_x(y) = 0 \tag{3-10}$$

However, in the actual silicon photonic integrated circuits, the waveguide typically has constraints in two directions, such as in a rectangular waveguide, which is most popularly used to build the basic optical components. The optical signal is transferred in one direction, i.e. the z direction. This can be achieved by introducing similar refractive index difference of waveguide core and cladding media in x direction as well as the y direction, taking figure 3.5 as an example. Therefore, the conventional waveguides, such as strip waveguides and rib waveguides, can be formed. The schematics of the cross-section of a strip waveguide and a rib waveguide are shown in Figure 3.7

(a) and (b). The refractive index of the waveguide layer is n_1 which is larger than the refractive index, n_2, of the surrounding material.

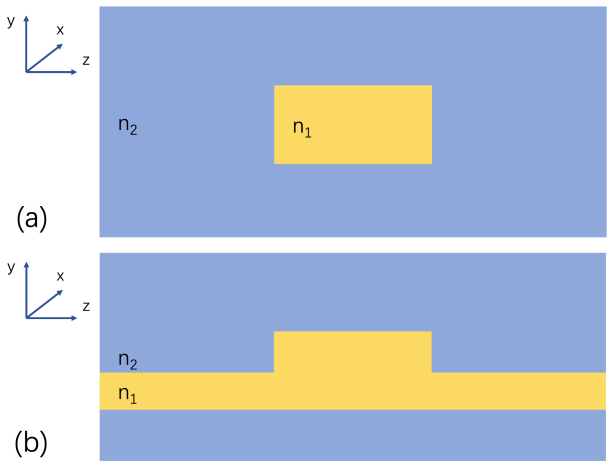

Figure 3.7 – Cross-section structure of (a) strip waveguide and (b) rib waveguide.

3.3.2 Silicon on insulator platform

In the CMOS industry and near infrared silicon photonics, SOI is one of the most common and popular platforms, which is shown in figure 3.8. SOI is a sandwich structure and consists of a silicon substrate at the bottom, a buried oxidation layer in the middle, and a thin silicon layer on top.

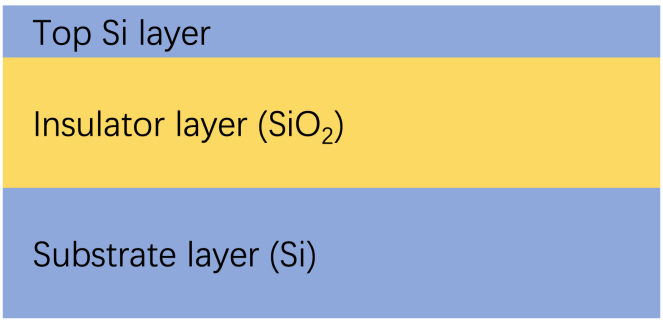

Figure 3.8 - Layer structure of Silicon on insulator wafer.

Compared with the traditional bulk silicon wafer, the CMOS integrated circuit fabricated on SOI wafers have advantages of high integration density, high communication speed, superior tolerance of high temperature and radiation. It has become the mainstream technology of developing micro-electronics and nano-electronics.

For integrated photonics, SOI also shows its unique advantages because of the large refractive index difference between Si and SiO_2, and consequently SOI has gained favour for applications that require a high density of integration. Silicon waveguides also have low absorption at telecommunication wavelengths, 1300nm to 1600nm. Figure 3.9 shows the absorption spectra of

silicon and silicon dioxide in wavelength range of 1 – 10 µm [140]. The absorption loss of silicon is lower than 1dB/cm over the wavelength range of 1.2 – 7 µm. Based on this transparent window, silicon is ideal for infrared applications.

The low loss silicon waveguide on SOI is the most fundamental component for silicon integrated photonic circuits. Single-mode SOI rib waveguides with loss as low as 0.1dB/cm were demonstrated in 1996 by Fischer et. al [141]. Bending of the waveguides is one of the key issues affecting the integration performance. To achieve high integration level, the radius of bending should be designed as small as possible. However, small and sharp bending structures of waveguides will lead to high side radiation loss. Avoiding the energy loss from side radiation is the main problem that should be considered when designing the waveguide bend.

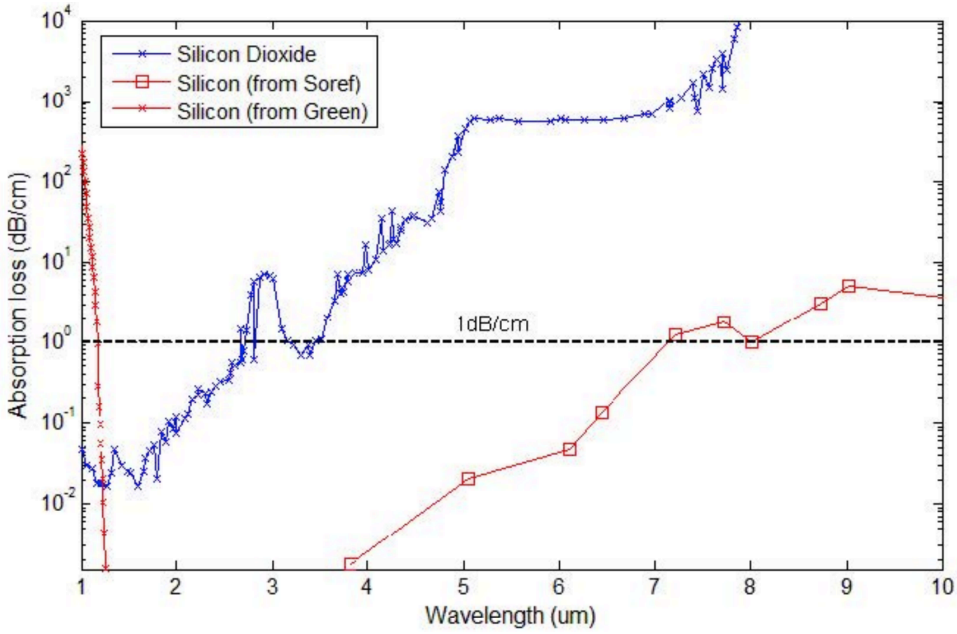

Figure 3.9 - Absorption spectra of silicon and silicon dioxide [141].

3.4 Directional couplers

The directional coupler is an optical passive device that can realise power coupling from one waveguide to another and achieve power redistribution at the output ports [1]. The optical field, which extends beyond the waveguide core, is referred to as the evanescent field. The coupling between waveguides will occur as the evanescent fields of these two waveguides are overlapping, which is shown in Figure 3.10 [1]. These two waveguides have the same width *w*, and are separated by a gap *s*. The transfer of power results from the coupling of the propagating mode from one waveguide to the other.

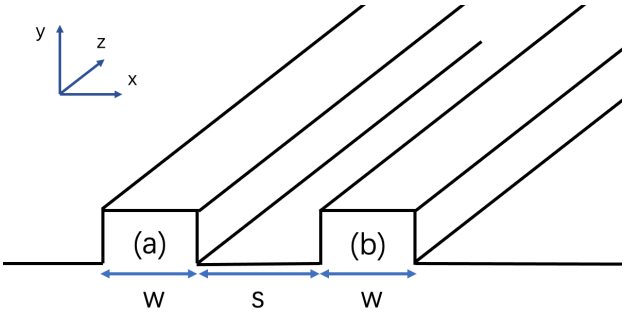

Figure 3.10 - Geometry of directional coupler [1].

The fields in waveguides (a) and (b) can be described as follows.

$$E_a = a_0(x,y)e^{j\beta z}e^{jwt} \tag{3-11}$$

$$E_b = b_0(x,y)e^{j\beta z}e^{jwt} \tag{3-12}$$

By inducing a coupling coefficient κ, and assuming that between the single modes of each waveguide the phases of the two modes are matched and no attenuation, and codirectional coupling, the coupling equations related with the amplitudes for each waveguide can be simplified as [1]:

$$da_0/dz = \kappa b_0 \tag{3-13}$$

$$db_0/dz = -\kappa a_0 \tag{3-14}$$

If there is no attenuation and co-directional coupling between each waveguide, then solutions to these equations can be illustrated as:

$$a_0(z) = c_0 \sin(\kappa z) \tag{3-15}$$

$$b_0(z) = c_0 \cos(\kappa z) \tag{3-16}$$

Therefore, the decrease of field in one waveguide gives rise to the field in the other. This power transfer process is periodic over a propagation distance z, which is noted as L_π. Based on the equations (3-15) and (3-16), after the distance $L_\pi = m\pi/2\kappa$, the power is transferred completely from guided waveguide to coupled waveguide [1]. The value of *m* is an odd integer. The transfer mode of the directional coupler shows that this device can achieve various power output distributions by controlling the coupling distance. A common application of this device is the 3-dB coupler with coupler length of $L_c = L_\pi/2 = m\pi/4\kappa$.

However, in real integrated circuits, absorption loss in the waveguide will not allow the unlimited coupling length. If the attenuation coefficient is set as $e^{-\alpha z}$, then the power in two waveguides can be expressed as [1]:

$$P_a(z) = sin^2(\kappa z)e^{-\alpha z} \tag{3-17}$$

$$P_b(z) = cos^2(\kappa z)e^{-\alpha z} \tag{3-18}$$

When calculating the coupling coefficient, mode confinement and propagation constant should all be taken into consideration. The study from Somekh et al. in 1973 shows that κ can be expressed as [142]:

$$\kappa = \frac{2k_{xc}^2 k_{xs}\exp(-k_{xs}s)}{\beta w(k_{xs}^2 + k_{xc}^2)} \tag{3-19}$$

In this equation, k_{xc} is the propagation constant in the waveguide along the x-direction, while the k_{xs} is the decay constant of gap between waveguides, w is the width of waveguide, and s is the gap between waveguides. Based on this equation, the coupling efficiency of a directional coupler also varies with the wavelength of light. Figure 3.11 shows the simulated output of a conventional directional coupler. z represents the length of coupling region between two waveguides and L_c is the coupling length achieving the highest coupling efficiency. Assuming that the optical power is input in I_2, and I_1 is the drop port output.

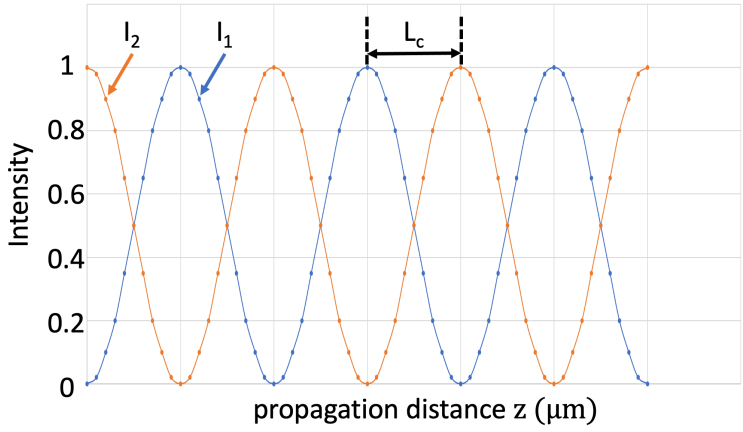

Figure 3.11 - Simulated optical output of a directional coupler.

3.5 Multimode interferometer

The multimode interferometer (MMI) is an optical device consisting of a planar waveguide and several input/output ports located at the front and end face. A multi-mode planar waveguide allows a continuum of waveguide modes to freely propagate in the multimode region. The signal

from the input ports to the multimode region will propagate as the combination of continuum of multiple modes. After the interference among those modes, the multiple images will periodically appear along the multimode region. Figure 3.12 shows the schematic of a typical 2×2 MMI used in this project. Tapers are used for each input/output ports, providing an efficient coupling of optical signal between waveguides.

Figure 3.12 - Schematic of 2×2 MMI.

The self-imaging theory of MMIs was firstly published by Soldano et al. in 1995 [143]. It is the basic theory of all MMI devices. The refractive index of the core of MMI, n_r, is higher than the cladding refractive index, n_c. Based on the theory discussed in section 3.3.1, the light will propagate along the z direction, which is shown in Figure 3.13.

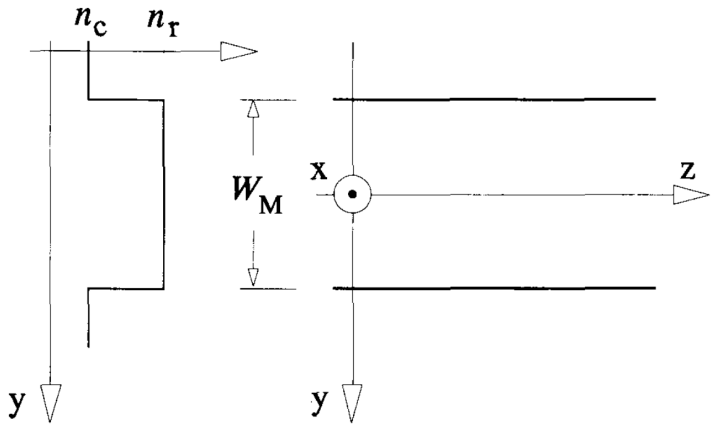

Figure 3.13 - Schematic of the step-index along the multimode structure [143].

Based on the light propagation theory in waveguides, the lateral wavenumber, k_{yv} and propagation constant, $\beta_v = k_{zv}$ need to satisfy the following equation, while v is the mode number [143]:

$$k_{yv}^2 + \beta_v^2 = k_0^2 n_r^2 \tag{3-20}$$

Where,

$$k_0 = \frac{2\pi}{\lambda} \tag{3-21}$$

$$k_{yv} = \frac{(v+1)\pi}{W_{eff,v}} \tag{3-22}$$

Where λ is the wavelength of input light and $W_{eff,v}$ is the effective width of mode v, which is determined by Goos-Hahnchen shifts [143]. In SOI waveguide, the contrast of refractive index of core and cladding is high. Therefore, the effective width of higher mode $W_{eff,v}$ is approximated to $W_{eff,0}$, which is the effective width of fundamental mode. The width of fundamental mode can be further approximately equal to W_{MMI}, the width of multimode waveguide in the MMI.

$$W_{eff,v} \approx W_{eff,0} = W_{MMI} + (\frac{\lambda}{\pi})(\frac{n_c}{n_{eff}})^{2\sigma}\left(n_{eff}^2 - n_c^2\right)^{-\frac{1}{2}} \approx W_{MMI} \tag{3-23}$$

where $\sigma = 0$ for TE mode, $\sigma = 1$ for TM mode.

Also, in SOI waveguides, the penetration depth, is far smaller than the length of multimode region due to the limitation of waveguide dimensions. We have:

$$k_{yv}^2 \ll k_0^2 n_r^2 \tag{3-24}$$

By using the binomial expansion [143]:

$$\beta_v \approx k_0 n_r - \frac{(v+1)^2\pi}{4n_{eff}W_{eff,v}^2} \tag{3-25}$$

The beat length, L_π, of the two lowest-order modes is [143]:

$$L_\pi = \frac{\pi}{\beta_0 - \beta_1} \approx \frac{4n_r W_{eff,v}^2}{3\lambda} \tag{3-26}$$

The difference between the propagation constants from the fundamental mode is [143]:

$$\beta_0 - \beta_v \approx \frac{v(v+2)\pi}{3L_\pi} \tag{3-27}$$

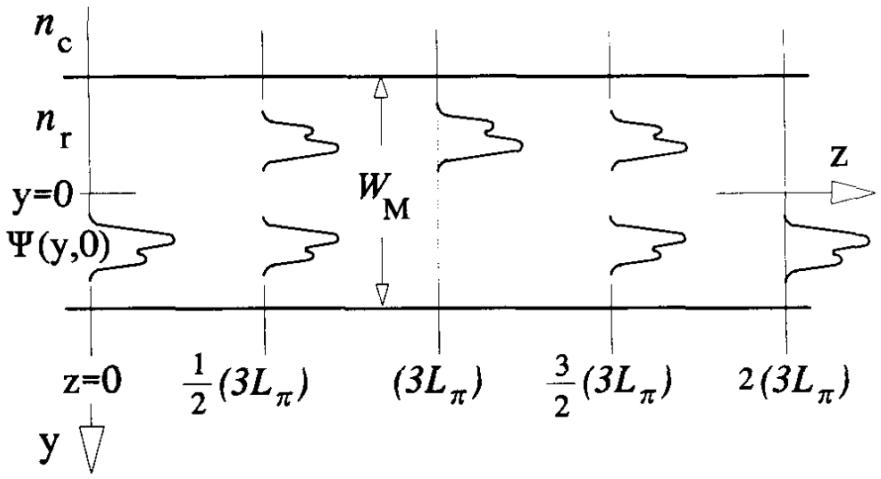

Figure 3.14 - Schematic of the multimode waveguide with the input field, a mirrored single image, a direct single image and two-fold images [143].

Figure 3.14 shows the input field profile starts at $z = 0$ and it is totally contained in a multimode waveguide. This input field will decompose into the modal field distribution of all modes and the signal propagates along z direction. If only confined modes are considered, then we have:

$$\Psi(y,0) = \sum_{v=0}^{m-1} c_v \psi_v(y) exp[j(\omega t - \beta_v z)] \tag{3-28}$$

If we further consider the time dependence exp $(j\omega t)$ and absorb the common fundamental mode term exp $(-j\beta_0 z)$, the equation (3-28) transforms into:

$$\Psi(y,0) = \sum_{v=0}^{m-1} c_v \psi_v(y) exp[j(\beta_0 - \beta_v)z] \tag{3-29}$$

After substitute equation (3-27), the field profile at the distance $z = L$ can be presented as [143]:

$$\Psi(y,0) = \sum_{v=0}^{m-1} c_v \psi_v(y) exp\left[j\frac{v(v+2)\pi}{3L_\pi}L\right] \tag{3-30}$$

Under the following condition:

$$L = p(3L_\pi) \text{ where } p = 0, 1, 2 \ldots. \tag{3-31}$$

The exponential part is:

$$\begin{cases} exp\left[j\frac{v(v+2)\pi}{3L_\pi}L\right] = 1 & p\ is\ even \quad (3\text{-}32) \\ exp\left[j\frac{v(v+2)\pi}{3L_\pi}L\right] = (-1)^v & p\ is\ odd \quad (3\text{-}33) \end{cases}$$

And combining the symmetry of transverse modes:

$$\psi_v(-y) = (-1)^v \psi_v(y) \tag{3-34}$$

We can have:

$$\begin{cases} \Psi\big(y, p(3L_\pi)\big) = \sum_{v=0}^{m-1} c_v \psi_v(y) = \Psi(y,0) & p\ is\ even \quad (3\text{-}35) \\ \Psi(y, p(3L_\pi)) = \sum_{v=0}^{m-1} c_v \psi_v(y)\,(-1)^v = \Psi(-y,0) & p\ is\ odd \quad (3\text{-}36) \end{cases}$$

Based on this equation, the direct self-image and inverted self-image of input signal will appear at $z = p(3L_\pi)$, when p is even and odd respectively.

If considering a two-fold self-imaging condition when

$$L = \frac{p}{2}(3L_\pi) \text{ where } p = 1, 3, 5 \ldots. \tag{3-37}$$

Then, the field profile at this distance can be written as [143]:

$$\begin{aligned} \Psi\left(y, \frac{p}{2}(3L_\pi)\right) &= \sum_{v=0}^{m-1} c_v \psi_v(y) exp\left[jv(v+2)p\left(\frac{\pi}{2}\right)\right] \\ &= \sum_{v\ is\ even} c_v \psi_v(y) + \sum_{v\ is\ odd} (-j)^p c_v \psi_v(y) \\ &= \frac{1+(-j)^p}{2}\Psi(y,0) + \frac{1-(-j)^p}{2}\Psi(-y,0) \end{aligned} \tag{3-38}$$

This result shows that the multimode waveguide simultaneously produces a pair of images of $\Psi(y,0)$ at $z = \frac{p}{2}(3L_\pi)$, where $p = 1, 3, 5$ ….These two images both have half of the power as the original input signal at $z = 0$. The distribution of optical power at this position is named as two-fold image.

Soldano et al. also gives the conclusion that the N-fold image will be generated at [143]:

$$L = \frac{p}{N}(3L_\pi) \tag{3-39}$$

N is the order of self-imaging. In this condition, integer p and integer N have no common divisor. The input power is equally distributed into each N-fold sub image. Substituting L_π from equation (3-26) into equation (3-39), we have:

$$L_{MMI} \approx \frac{4Nn_{eff}W_{MMI}^2}{\lambda} \quad (3\text{-}40)$$

L_{MMI} is the length of multimode waveguide in the MMI. λ is the input wavelength and n_{eff} is the effective refractive index in multimode waveguide. In this project, the MMI acts as a 3dB coupler in MZIs, providing optical power splitting and combining. Therefore, the intensity of each output signal should be half of the input signal. Based on the equation 3-40, the two output ports should be located at the position of the second order of self-imaging, in the case of N=2.

3.6 Mach-Zehnder interferometer

The MZI is a famous structure in photonic circuits that has been used to develop applications such as modulators, optical switches, phase shifters and sensors [1, 139]. A sketch of a general 1×2 MZI is shown in figure 3.14. The optical signal is launched from input 1 to the left 3dB coupler. This 3dB coupler can be the directional coupler mentioned in the former section, or other device with similar functions, such as Y-junctions and 3dB multi-mode interferometers. The optical signal is divided into two output ports (Arm1 and Arm2). By inducing the phase difference between arm1 and arm2, two signals will therefore propagate with different phase state, ϕ_1 and ϕ_2. They are finally interfered at the right-hand coupler and then launched out from the two outports at the right (Output1 and Output2) [1, 144].

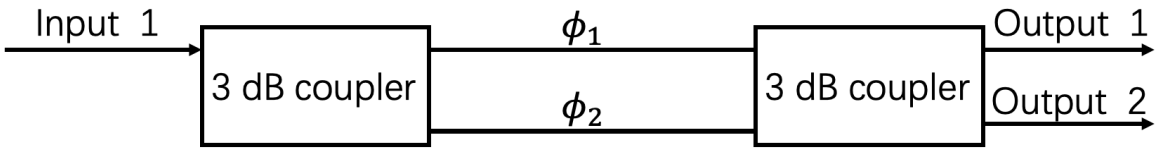

Figure 3.15 - Geometry of 1×2 optical Mach-Zehnder interferometer.

Based on different applications, the method of introducing phase difference into the two arms can be different. For passive devices such as signal splitters, designing different lengths of the optical path can achieve this function. For active devices, such as modulators, optical switches and phase shifters, electro-optical effects and thermo-optical effects will be used to control the optical phase difference between the two arms.

Assuming that the MZI, with one input and one output, is lossless and imbalanced, its transfer functions can be simply illustrated as follows [144]:

$$\begin{bmatrix} E_{out1} \\ E_{out2} \end{bmatrix} = M_{1\times 2MZI}E_{input1} = \begin{bmatrix} \frac{1}{2}(\tau_1 e^{j(\omega t-\phi_1)} - \tau_2 e^{j(\omega t-\phi_2)}) \\ \frac{1}{2}(\tau_1 e^{j(\omega t-\phi_1)} + \tau_2 e^{j(\omega t-\phi_2)} \end{bmatrix} \quad (3\text{-}41) \quad (3\text{-}42)$$

Where τ_1 and τ_2 are the transmission coefficients for each arm, the output intensity can be written as [144]:

$$\begin{cases} \frac{I_{out1}}{I_{input1}} = \left(\frac{E_{out1}}{E_{input1}}\right)^2 = \frac{1}{4}[\tau_1^2 + \tau_2^2 - 2\tau_1\tau_2\cos(\phi_1 - \phi_2)] & (3\text{-}43) \\ \frac{I_{out2}}{I_{input1}} = \left(\frac{E_{out2}}{E_{input1}}\right)^2 = \frac{1}{4}[\tau_1^2 + \tau_2^2 + 2\tau_1\tau_2\cos(\phi_1 - \phi_2)] & (3\text{-}44) \end{cases}$$

Assuming there is no loss in waveguides, $\tau_1 = \tau_2 = 1$, then we have [144]:

$$\begin{cases} \frac{I_{out1}}{I_{input1}} = \frac{1}{2}[1 - \cos(\phi_1 - \phi_2)] = \sin^2\left(\frac{\Delta\phi}{2}\right) & (3\text{-}45) \\ \frac{I_{out2}}{I_{input1}} = \frac{1}{2}[1 + \cos(\phi_1 - \phi_2)] = \cos^2\left(\frac{\Delta\phi}{2}\right) & (3\text{-}46) \end{cases}$$

Where $\Delta\phi$ is the phase difference between two arms in MZI, including the environmental factors such as temperature fluctuations and fabrication errors.

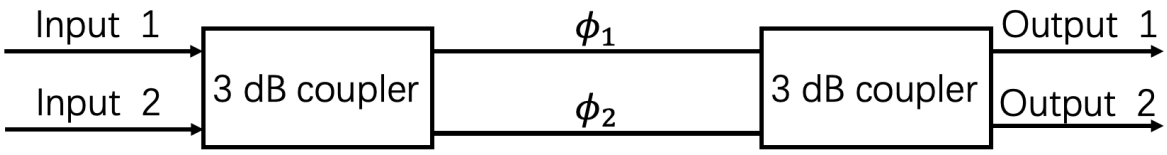

Figure 3.16 - Geometry of 2×2 optical Mach-Zehnder interferometer.

For the 2 x 2 MZI, we have two inputs and two outputs, which is shown in the figure 3.15. The transfer function can be described as [144]:

$$\begin{bmatrix} E_{out1} \\ E_{out2} \end{bmatrix} = M_{2\times2MZI}\begin{bmatrix} E_{input1} \\ E_{input2} \end{bmatrix}$$

$$= \frac{1}{2}\begin{bmatrix} \tau_1 e^{j(\omega t-\phi_1)} - \tau_2 e^{j(\omega t-\phi_2)} & -\tau_1 e^{j(\omega t-\phi_1)} - \tau_2 e^{j(\omega t-\phi_2)} \\ \tau_1 e^{j(\omega t-\phi_1)} + \tau_2 e^{j(\omega t-\phi_2)} & -\tau_1 e^{j(\omega t-\phi_1)} + \tau_2 e^{j(\omega t-\phi_2)} \end{bmatrix}\begin{bmatrix} E_{input1} \\ E_{input2} \end{bmatrix} \quad (3\text{-}47)$$

This equation can further be simplified by assuming that only one input is excited, such as:

$$\begin{bmatrix} E_{input1} \\ E_{input2} \end{bmatrix} = \begin{bmatrix} 1 \\ 0 \end{bmatrix} \quad (3\text{-}48)$$

Then, this situation is the same as the 1×2 MZI. The outputs can be written as:

$$\begin{cases} \frac{I_{out1}}{I_{input1}} = \sin^2\left(\frac{\Delta\phi}{2}\right) & (3\text{-}49) \\ \frac{I_{out2}}{I_{input1}} = \cos^2\left(\frac{\Delta\phi}{2}\right) & (3\text{-}50) \end{cases}$$

Based on the former equations, the distribution of optical power at output ports can be controlled by the optical phase difference between the two arms in the MZI.

3.7 Ring resonator

Ring resonators play a significant role in the silicon photonic integrated circuits. Different to directional couplers and MZIs, this structure has the function of wavelength selection and was firstly used in an optical filter [1, 5, 139, 145]. Multi ring resonator arrays are used as multiplexers, demultiplexers and optical switch arrays.

Figure 3.17 show the simplest structure of the ring resonator, which consists of a straight waveguide and a closed ring waveguide. Due to the evanescent wave effect, light will be gradually coupled into ring waveguide when the light propagates through the upper bus waveguide. The optical wave coupled in the ring propagates around the ring. After one round trip in the ring waveguide, this wave will interfere with other waves, which is just coupled from the straight waveguide. a is the round-trip transmission of the light in the ring waveguide. r is the self-coupling coefficient. k is defined as the cross-coupling coefficient. In order to form the standing wave in the ring waveguide, the radius of ring and the wavelength of light should have the relationship:

$$2\pi R n_{eff} = m\lambda_r \qquad (3\text{-}51)$$

R is the radius of ring waveguide and n_{eff} is the effective index of guided mode in ring. λ_r represents the wavelength of light and m is the positive integer. This equation means the optical length of ring should be an integer multiple of the wavelength.

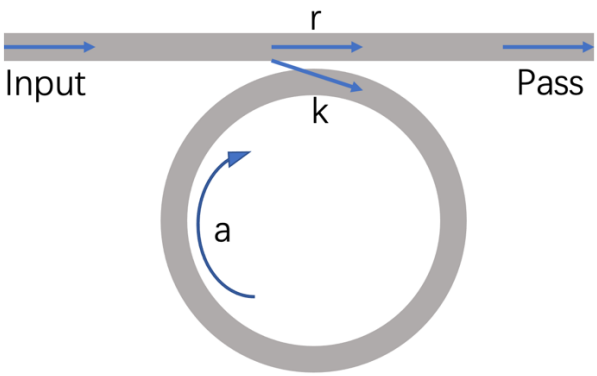

Figure 3.17 - Geometry of ring resonator with single drop [146].

The ratio of the transmitted field at the pass-port (normally referred to as “through-port”) can be expressed as follows [146]:

$$E_{pass}/E_{input} = e^{i(\pi+\phi)}\frac{a - re^{-i\phi}}{1 - rae^{i\phi}} \tag{3-52}$$

Where ϕ is the phase shift after a single pass, and can be expressed as $2\pi R\beta$. β is the propagation constant of the circulating mode. For a lossless ring, we have $a = 1$. The intensity transmitted can be therefore described as:

$$I_{pass} = I_{input}\frac{a^2 - 2racos\phi + r^2}{1 - 2racos\phi + (ra)^2} \tag{3-53}$$

Under the condition $\phi = 2\pi m$, where m is an integer, the intensity transmitted through the pass-port waveguide is:

$$I_{pass} = I_{input}\frac{(a - r)^2}{(1 - ar)^2} \tag{3-54}$$

Under the assumption that there is no loss in coupling section [146]:

$$r^2 + k^2 = 1 \tag{3-55}$$

Based on the relative relationships of a and r, the ring resonator has three different coupling situations.

When the bus waveguide transmission is greater than the ring waveguide transmission, we have $a < r$, which is known as under coupling. In this situation, the loss per round trip is greater than the coupling loss between bus waveguide and ring waveguide. The ring resonators working under this condition have a smaller resonance linewidth and low sensitivity to the thermal broadening [145, 146].

When the ring waveguide transmission is equal to the bus waveguide transmission, we have $a = r$, which is known as critical coupling. In this situation, the loss per round trip is also equal to the coupling loss between bus waveguide and ring waveguide. Because the light coupled out of ring waveguide is out of phase with the light in the bus waveguide, the destructive interference shows that there is no output intensity in the pass-port waveguide. This working situation can give the highest extinction ratio of the resonant wavelength.

When the ring waveguide transmission is greater than the bus waveguide transmission, we have $a > r$, which is known as over coupling. In this situation, the loss per round trip is less than the coupling loss between the bus waveguide and ring waveguide. The ring resonators working under this condition have a wide resonance linewidth due to more light being coupled in the ring waveguide.

For coarse wavelength division multiplexing applications, the optical signal filtered into the ring waveguide needs to be coupled out. Therefore, a drop waveguide is added at the other side of the ring, which is shown in figure 3.18. In this structure, the coupled field is partially transmitted to the drop port. This device facilitates the conversion of broadband input coupled signals to the out-coupling of discrete resonant signals. The transmission intensity at these two ports can be expressed as [146].

$$I_p = I_i \frac{r_2^2 a^2 - 2r_1 r_2 a cos\phi + r_1^2}{1 - 2r_1 r_2 a cos\phi + (r_1 r_2 a)^2} \quad (3\text{-}56)$$

$$I_d = I_i \frac{(1 - r_1^2)(1 - r_2^2)a}{1 - 2r_1 r_2 a cos\phi + (r_1 r_2 a)^2} \quad (3\text{-}57)$$

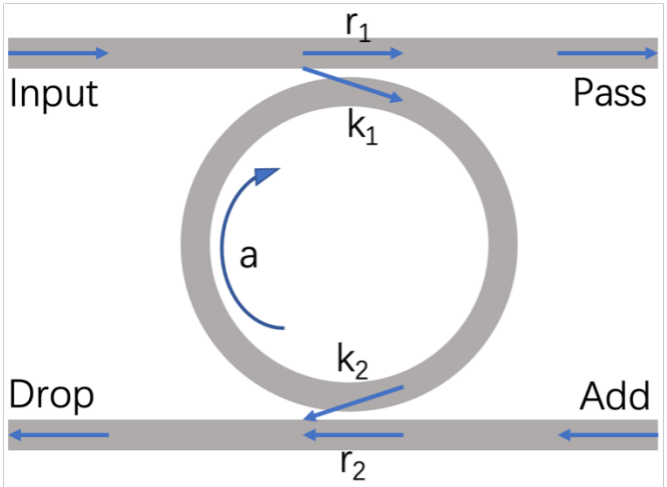

Figure 3.18 - Geometry of ring resonator with additional drop bus waveguide.

3.8 Summary

This chapter introduces the basic theory that will be used in this project, including ion implantation and why we chose Ge as the implanted ion. The laser annealing process is used to reverse the lattice disorder in the silicon lattice. The energy transfer in the laser annealing process is also introduced. Then the basic theory of optical waveguides and components, such as DCs, MZIs, MMIs, and ring resonators are discussed. In this project, the transmission of these devices can be changed with the refractive index shifted by implantation and annealing.

Chapter 4 Device design, simulation and fabrication

In this chapter, the simulation results and fabrication processes for the devices studied in this thesis are introduced. All the silicon photonic devices are based on (silicon on insulator) SOI wafers with a 220 nm thick top Si layer and 2000 nm thick buried oxide (BOX) layer. The devices are simulated using software from Lumerical. All fabrication processes were completed in the Nanofabrication Centre at the University of Southampton, except for the Ge ion implantation process which was carried out at the Ion Beam Centre at the University of Surrey, UK.

4.1 Device design and simulations

This section will introduce the simulation processes and results of optical devices used in this project. MZI has been used to develop optical modulators, optical switches, phase shifters and sensors. An accurate 3dB coupler is one of the most significant components in the MZI. A 2×2 MMI is used in this project to equally split input signal into two waveguides. Two implanted sections with different length are designed into two arms of the MZI, causing phase difference between two optical signals. After traveling through two arms of the MZI, these two optical signals will interfere at another 2×2 MMI.

The designing processes of circular ring resonators are also introduced. After inducing a segment of implantation region in the ring waveguide, the resonance wavelength is changed. For achieving higher coupling efficiency between ring waveguide and bus waveguide, a racetrack ring resonator with longer coupling region is designed. The coupling efficiency can be changed by designing an implanted coupling region.

The directional couplers used in this project are different from the conventional ones. One of the waveguides in these devices is formed by the implantation process but not traditional etching process. The ratio of power distribution at the output ports for each coupler can be controlled by the length of the implanted waveguide.

4.1.1 Simulation results: MZIs

In this project, the MZIs were used as 2×2 splitters and switches. Two 2×2 MMIs were used as the 3dB splitters for each MZI. The width of this MMI was set at 6μm while the two input ports of this MMI were symmetrically located with a gap of 2μm. The length and width of the MMI are 44.8μm and 6μmrespectively. Tapers with 20μm length are used to convert the mode size between the input/output waveguides and core multimode waveguide, achieving lower optical

loss. The field profile of this MMI is shown in Figure 4.1, which was simulated using the EME simulator in Lumerical MODE solution.

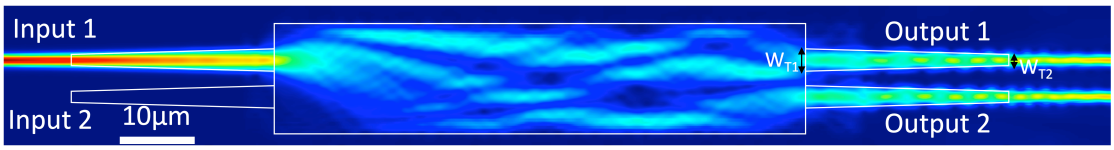

Figure 4.1 - Simulated field profile of MMI working as 3dB coupler.

The width, W_{T2}, of the tapers is 500nm, which is the same as the conventional waveguides used in this work. The other end face of the taper is connected with the multimode waveguide. The width of this side, W_{T1}, is designed as 1.5µm, achieving the highest simulated optical transmission of 49%, demonstrating that this MMI works as a nominally 3dB coupler. Figure 4.2 shows the change of optical transmission of output 1 when the W_{T1} scans from 0.5µm to 3µm. Due to the crosstalk between two output ports, a wider taper will lead to cross coupling between the two waveguides, which is shown in Figure 4.3. However, shorter W_{T1} will induce additional optical loss caused by mode mismatch between waveguides.

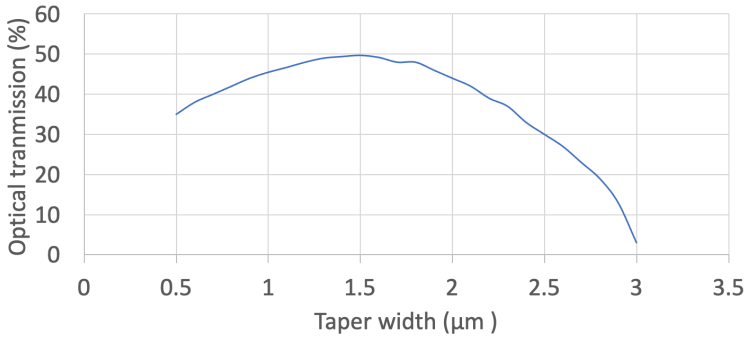

Figure 4.2 - Optical transmission of output1 changes as the function of taper width.

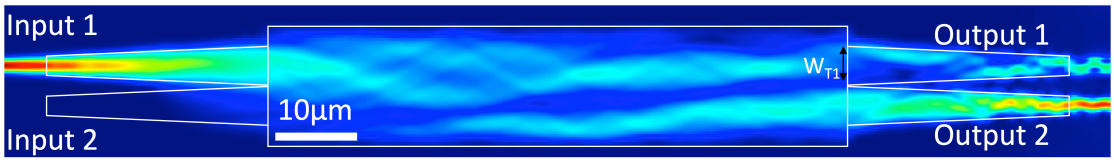

Figure 4.3 – Simulated field profile of MMI with W_{T1} is 2µm.

The structure of an implanted MZI is shown schematically in Figure 4.4. Implanted sections with different lengths are introduced in the arms to control the optical phase difference. The shorter one has a fixed length of 2µm and is to balance any possible reflection loss at the interface between implanted silicon and crystalline silicon, so that both arms experience the same parasitic losses. The length of the longer implanted section can be varied to induce a different phase difference between the two arms. The transmission for the output ports is therefore altered.

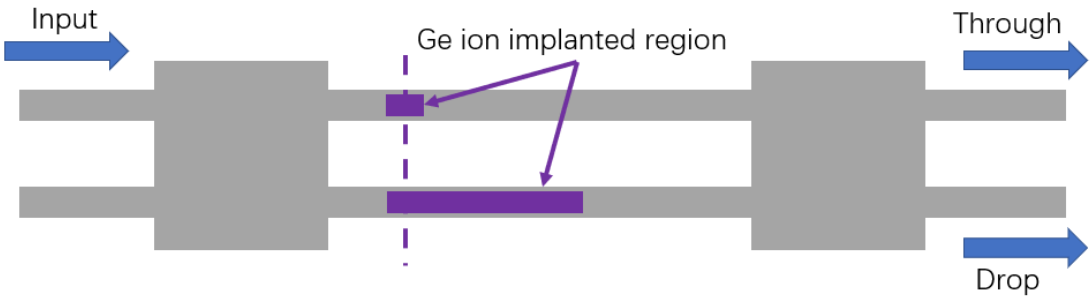

Figure 4.4 - Structure of MZI with implanted sections in two arms.

The depth and width of the implantation region in the waveguide can also affect the transmission. The implantation depth is controlled by the implantation energy, which will be discussed in the later fabrication section of this thesis. The width of the implantation region should be firstly optimised. Based on our former results, the depth and refractive index of implanted region in the waveguide is set as 170nm and 3.96 [100]. Figure 4.5 gives the comparison of simulated optical transmission change under different implanted widths. For a fixed 8μm implantation length, 400nm width can provide approximately a 2π radian phase shift, while 200nm width can provide around π radian phase shift. Wider implantation, such as 500nm, can provide greater phase shift. However, in the Deep-UV lithography processes, there could be misalignment of the waveguide layer and implantation mask layer. For example, a 50nm misalignment can lead the maximum 50nm variation of 500nm wide implantation region. To minimise the difference between simulation results and measurement results, the width of the implantation section in a 500nm wide waveguide is designed as 400nm.

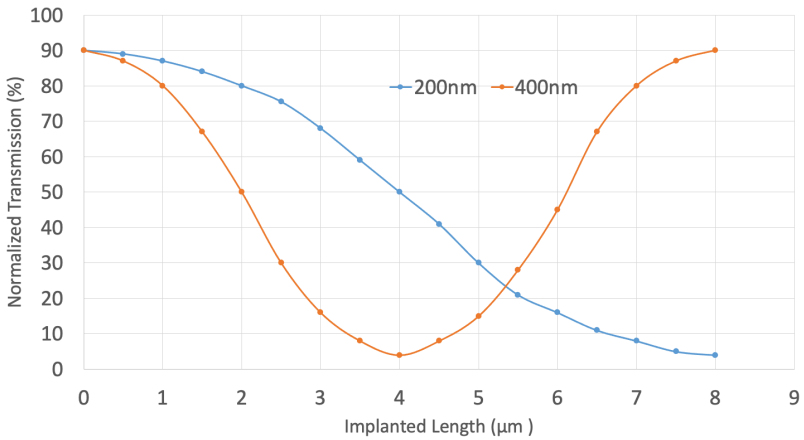

Figure 4.5 - Simulated optical transmission as a function of implanted length for different width.

The transmission of implanted MIZs should periodically change with the length of the implantation region (see chapter 3), which is shown in simulation in Figure 4.6. In this simulation, the length of the longer implantation section is varied between 0μm and 8μm. The width of the implantation sections is 400nm. They all located at the centre of the waveguides. When the length of the longer implantation section is 0μm, a part of optical signal is coupled into the drop

port output. When the length increased to 2μm, over 80% of optical signal is detected at the through port. A maximum transmission of 90% is obtained at the through port for an implanted length of 2.5μm. In this work, the longer implantation sections for the MZIs are designed with different lengths to characterise different transmissions.

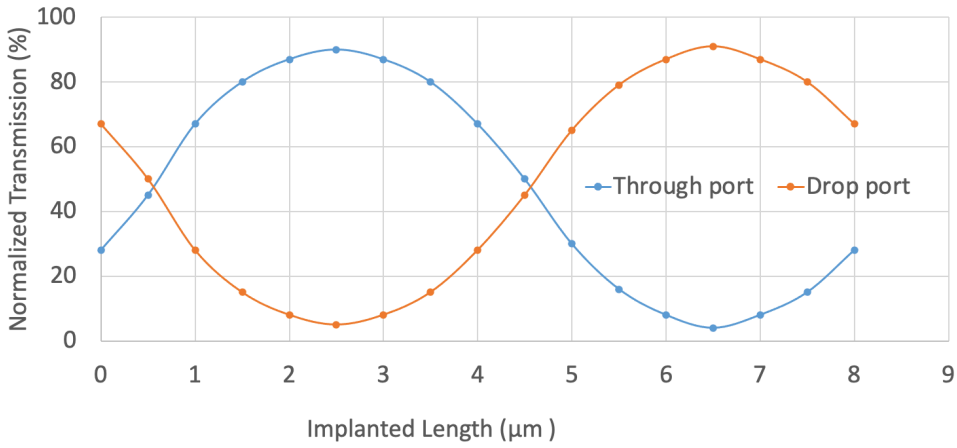

Figure 4.6 - Simulated optical transmission of implanted MZI with different implantation length.

4.1.2 Simulation results: ring resonators

In this project, a segment of Ge ion implantation will be induced into the silicon waveguide and results in the change of effective index of the propagating mode and additional optical loss. This change can directly change the coupling conditions and shift the resonant wavelength of an implanted ring resonator. The structure of a simulated ring resonator is shown in Figure 4.7. The width of bus waveguide and ring waveguide are all 500nm. The thickness of the slab layer is 100nm. The radius of this ring is 10μm. The gap between the straight waveguide and the ring waveguide is set as 100nm. The width and depth of implantation region in the ring waveguide is set as 400nm and 170nm respectively. The arc length of this implantation segment is 10°.

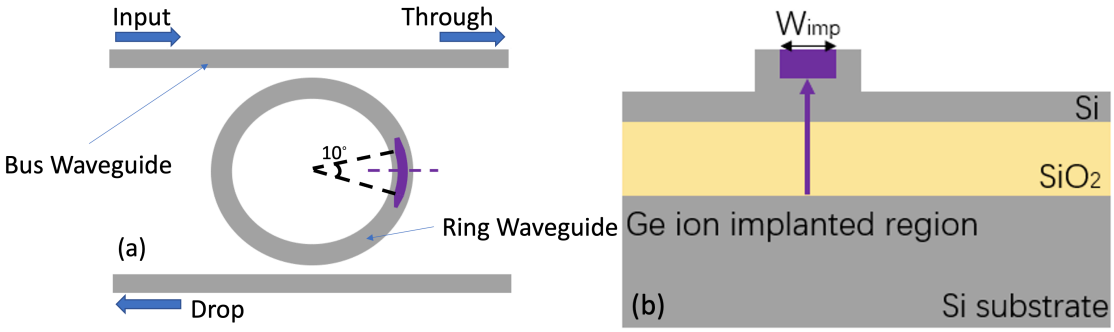

Figure 4.7 - Top view (a) and cross section (b) of Ge ion implanted ring resonator.

Figure 4.8 gives the simulated spectra of the unimplanted and implanted ring resonator, respectively. Simulations are carried out using the varFDTD simulator in Lumerical Mode solution.

The length of each resonance wavelength is called the free-spectral range (FSR). The FSR depends on the resonance wavelength λ_r, and length of ring waveguide L_r by:

$$FSR = \frac{\lambda_r^2}{n_g L_r} \quad 4\text{-}1$$

Where, n_g is the group index. Extinction ratio, in the transmission spectrum of a ring resonator, represents the difference between the highest and lowest through-port transmission intensity levels, close to the cavity resonant wavelength. Thus, for each resonance wavelength, there is a corresponded extinction ratio.

For the unimplanted ring resonator, a resonant wavelength near 1550nm is located at 1547.6nm. The FSR near this resonance wavelength is around 11nm, and the extinction ratio is over 25dB. After an ion implantation segment with 10° induced into the ring waveguide, this resonance peak shows a red shift of 2.7nm to 1550.3nm. Therefore, the resonant wavelength of a ring resonator is successfully changed via inducing an implantation section in the loop waveguide.

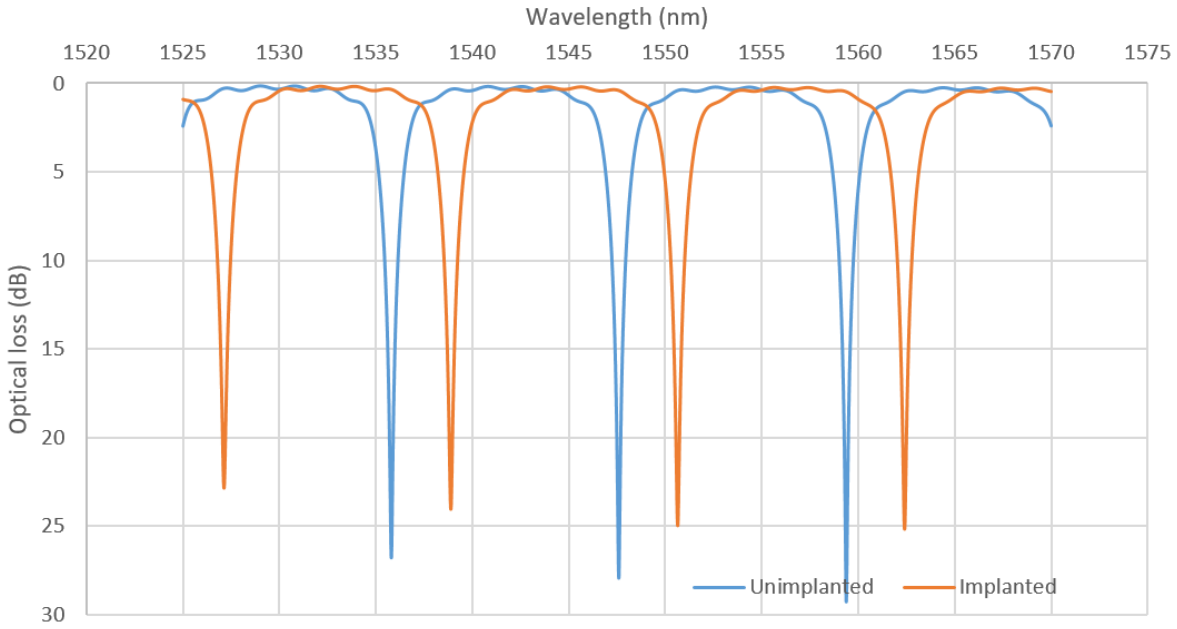

Figure 4.8 - Simulated spectra of implanted and unimplanted ring resonators.

Racetrack resonators have an extended coupling length between bus waveguide and ring waveguide as compared to circular ring resonators. Hence the coupling coefficient can be higher than the circular ring resonator. We aim to fabricate implantation sections located at the slab part between the bus waveguide and loop waveguide, which can change the coupling state of racetrack resonators. Figure 4.9 schematically shows the structure of an implanted racetrack resonator. The width of all the waveguides is 500nm. The slab layer of the rib waveguide is 100nm thick. The racetrack consists of two semicircles with radius of 25µm. The coupling region with a length of 6µm is fully implanted.

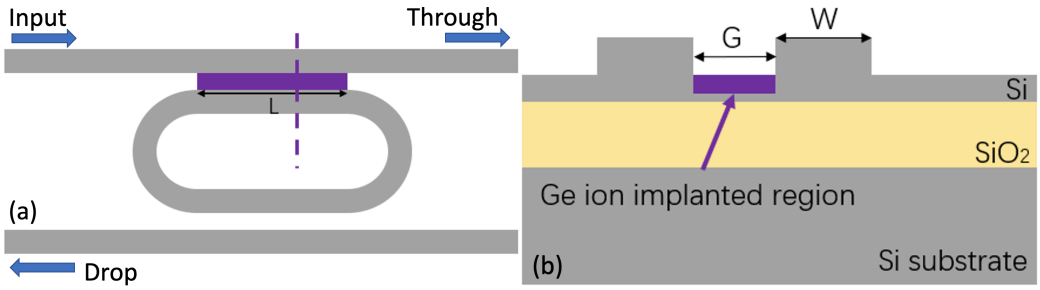

Figure 4.9 - Top view (a) and cross section (b) of Ge ion implanted racetrack resonator.

Figure 4.10 (a) and (b) show the field profile of un-implanted racetrack and implanted racetrack, working at the resonant wavelength. The simulated spectra of these two devices are shown in figure 4.10 (c). The resonance wavelength shows a red shift after the implantation. The extinction ratio also decreases from 22dB to 16dB due to the additional loss cause by implantation damage. This result shows that Ge ion implantation into the slab region between the bus waveguide and the ring waveguide can permanently change the coupling efficiency and resonant wavelength of racetrack resonators.

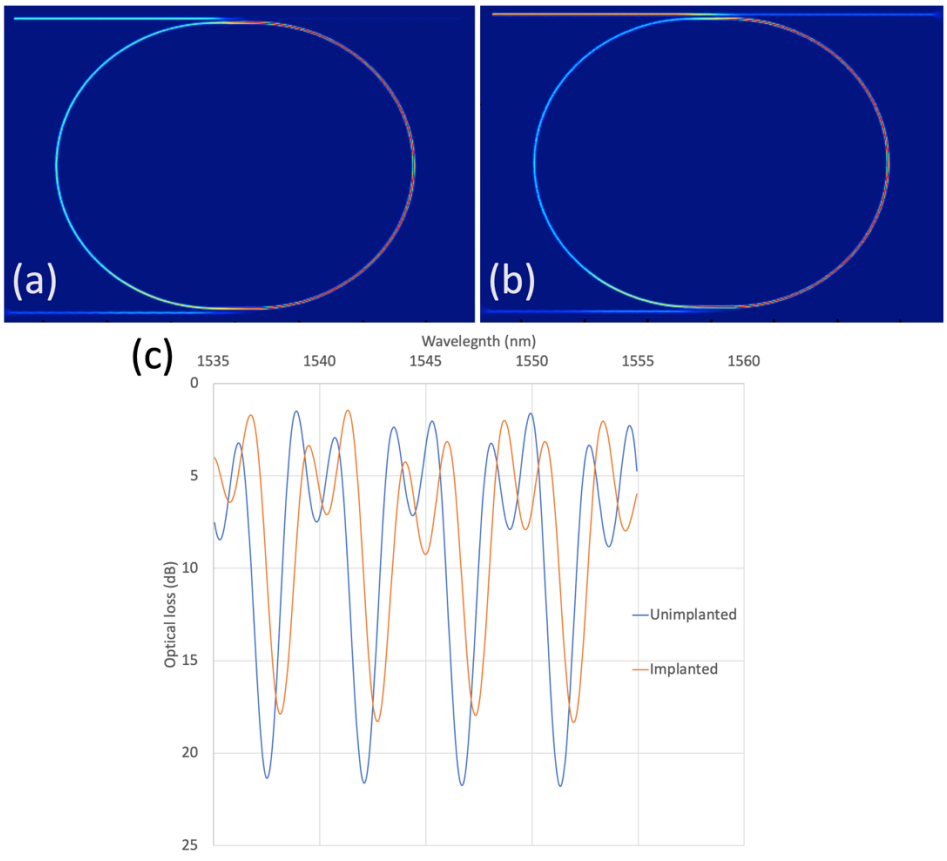

Figure 4.10 - Simulated field profile of un-implanted racetrack (a) and implanted racetrack (b). (c) Optical spectra of implanted and un-implanted racetrack resonators.

4.1.3 Simulation results: single-stage directional couplers

In this project, erasable directional couplers (DCs) are used for wafer-scale testing. A single-stage DC has been designed with one conventional waveguide and one implanted waveguide. This device was also simulated by varFDTD simulator in Lumerical's Mode solution. Phase matching is the basic condition for efficient waveguide-to-waveguide coupling. The simulated mode distributions for implanted waveguide and conventional waveguide are shown in figure 4.11. In this simulation, the conventional rib waveguides were formed by a 70 nm partial etch, leaving a 150 nm thick slab layer. The height and width of the strip part were 220 nm and 500 nm. An implanted waveguide was formed in the slab layer with width of 500 nm. Based on the implantation profile from our former studies, the height of this implanted waveguide was set as 140 nm [98-100]. The effective indexes for the TE0 modes of each waveguide are 2.72 and 2.78 respectively.

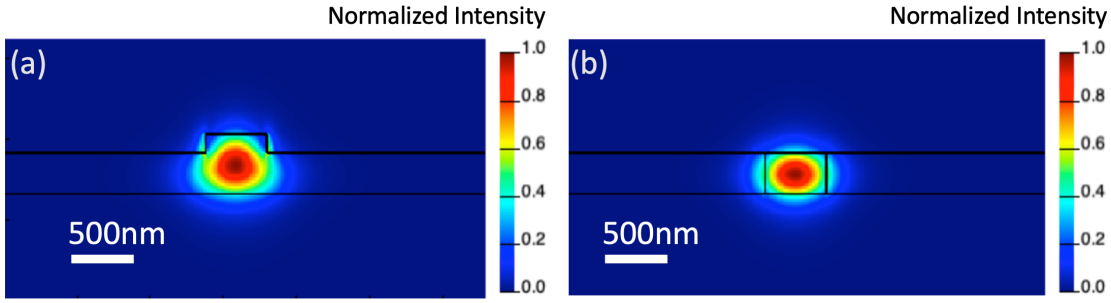

Figure 4.11 - Simulated TE0 mode distribution of conventional waveguide (a) and implanted waveguide (b).

The top view and cross-section of single-stage implanted directional coupler are shown in figure 4.12. The implanted waveguide is still formed in the slab layer of the rib waveguide. In the simulation, the width of implanted waveguide and conventional waveguide are designed as 500nm and 500nm respectively. The gap between them is 200nm. A conventional rib waveguide is connected with the end of implanted waveguide. The length of straight part of implanted waveguide is defined as L_c.

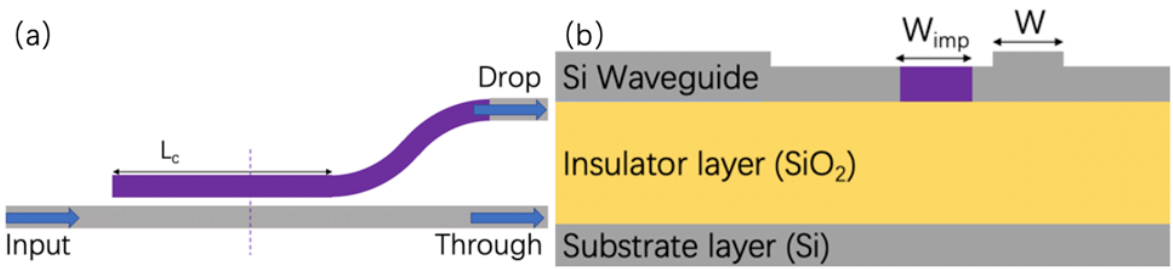

Figure 4.12 - (a) Top view and (b) cross-section of a single-stage implanted DC.

In this device, the optical signal will be coupled into the implanted waveguide from the input waveguide. The coupled light will propagate through an S-bend implanted waveguide before it is finally launched out at the drop port.

Two single-stage implanted DCs with 30° (10µm radius) and 90° (5µm radius) were simulated by Lumerical Mode solution. Figures 4.13 (a) and (b) shows the field profile of these two devices working at their highest coupling efficiency. These two devices both achieve their highest coupling efficiency at a coupling length of 7µm. Figure 4.14 (a) and (b) present the transmission shift with different coupling length. For coupling length equal to 0µm, a part of optical signal will be still coupled into the drop-port output, which is caused by the coupling between bent waveguide and input waveguide. For the DC with 30° bending, the highest detected optical power at drop-port output is over 85% of input signal. For the DC with 90° bending, the monitored peak output at drop-port is only 68%. This difference is caused by that sharper bent waveguide results in greater bending loss, so the final device can be designed with a more gradual bend to avoid any excess loss. In the figure 4.13 (b), the leaked optical field is more obvious at the right side of bended waveguide. With increasing coupling length, the optical signal in the implanted waveguide starts to be coupled back to the through-port output.

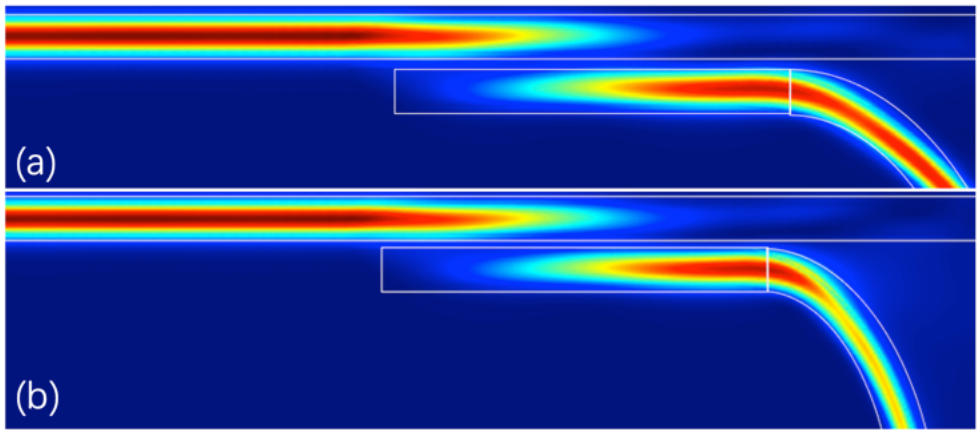

Figure 4.13 - Field profile of single-stage implanted DCs working at the highest coupling efficiency. (a) 30° bending and (b) 90° bending.

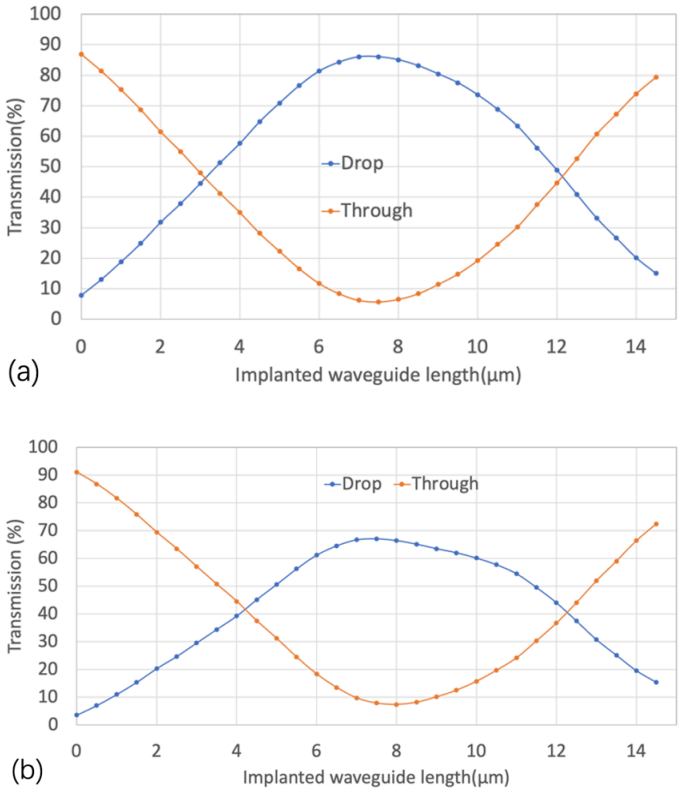

Figure 4.14 – Simulated transmission of single-stage implanted DCs with (a) 30° bending and (b) 90° bending implanted waveguide.

In the former two simulations, the bending part of the waveguide is designed as an implanted waveguide. The transmission of the signal detected at the drop-port can be increased by approximately 9% (depending on waveguide length) if the implanted waveguide is replaced by a conventional silicon rib waveguide, after the coupling section. The simulated results are shown in figure 4.15. We can conclude that the implanted waveguide will induce higher transmission loss than the conventional waveguide. However, in this single implanted DC, 10% of input signal will be coupled into the drop port waveguide even with no implanted waveguide, because the distance between input waveguide and output waveguide is too small. Therefore, in the wafer-scale testing application, this part of coupled optical power will cause inevitable insertion loss in an integrated circuit. Moreover, there is additional reflection loss and mode mismatch loss in single-stage DC at the interface between the implanted waveguide and the conventional waveguide.

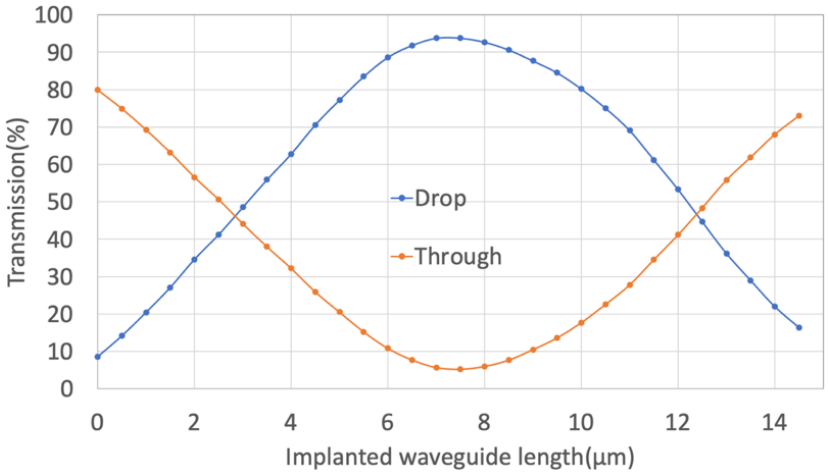

Figure 4.15 – Simulated transmission of single-stage implanted DCs with a 30° bending conventional waveguide.

4.1.4 Simulation results: two-stage directional couplers

For improving the transmission loss and insertional loss issues in single implanted DC, a two-stage erasable directional coupler is shown in figure 4.16. The conventional waveguides of the DC were formed by a 70 nm partial etch, leaving a 150 nm thick slab layer with width W = 500 nm and silicon guiding layer thickness is 220 nm. Between the input waveguide and output waveguide, an implanted waveguide was formed in the slab layer with width W_{imp} = 500 nm. In consideration of the resolution of our DUV lithography process, the gap between the implanted waveguide and conventional waveguide is 230 nm. L is the length of implanted waveguide. The optical signal can be coupled from input waveguide into implanted waveguide, and then subsequently coupled to the drop port output waveguide. The uncoupled optical signal will continually propagate to the through port output.

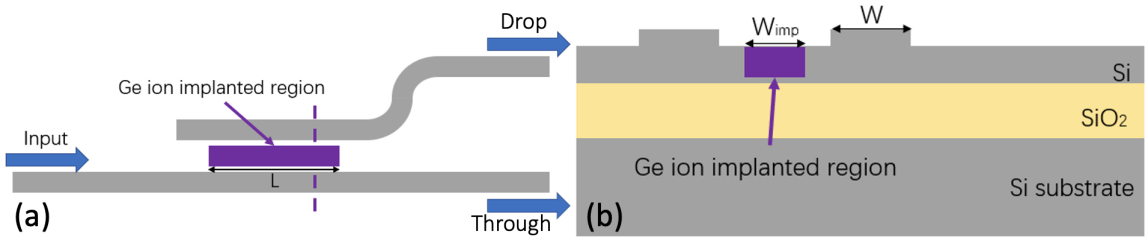

Figure 4.16 - Top view (a) and cross section (b) of Ge ion implanted two-stage DC.

This device was also simulated by varFDTD simulator in Lumerical's Mode solution. Figure 4.17 (a) gives the transmission of drop port output changes as a function of the implanted waveguide length. The optical transmission is coupled from the top waveguide into the middle-implanted waveguide, and subsequently coupled into the bottom waveguide. The length of the implanted waveguide determines the output transmission at drop port output. Figure 4.17 (b) shows the

simulated field profile of the erasable DC with a 12μm implanted waveguide. The highest simulated coupling efficiency, over 80% of the input signal, was achieved when the length of the implanted waveguide is 12μm. Figure 4.17 (c) shows the simulated field profile of the erasable DC with a 6μm implanted waveguide. The optical transmission of the through port and drop port are 29% and 24% respectively. Due to the limited length of the implanted waveguide, this device suffers from scattering loss at the far end of the implanted region. When the optical power cannot be fully coupled from implanted waveguide to the drop waveguide, the remaining optical power will scatter away at the end. When the length of the implanted waveguide is longer than 12μm, a part of the optical power in the bottom waveguide will couple back to the top waveguide through the implanted waveguide. The light left in the middle-implanted waveguide will also scatter away at the end. Figure 4.17 (d) shows the simulated field profile of an erasable DC with a 19μm implanted waveguide. The optical transmission of the through port and drop port are 31% and 33% respectively.

Based on these simulation results, the transmission of an implanted two-stage DC can be tuned via changing the length of implanted waveguide. However, the transmission curve of the two-stage DC is not a sinusoidal shape, and there is also no 3dB coupling state, which is caused by the scattering loss. Thus, two-stage DC is not ideal for photonics computing applications. Even so, the two-stage DC is still better than the single-stage DC when working as an optical power monitor in the wafer-scale testing application, because there is smaller insertion loss brough by coupling when the implanted waveguide is erased. When these two DCs are working at their highest coupling states, the transmission loss brought by implantation waveguide in a two-stage DC is actually lower than that of a single-stage DC. This is because that single-stage DC has a much longer implanted waveguide after the coupling region.

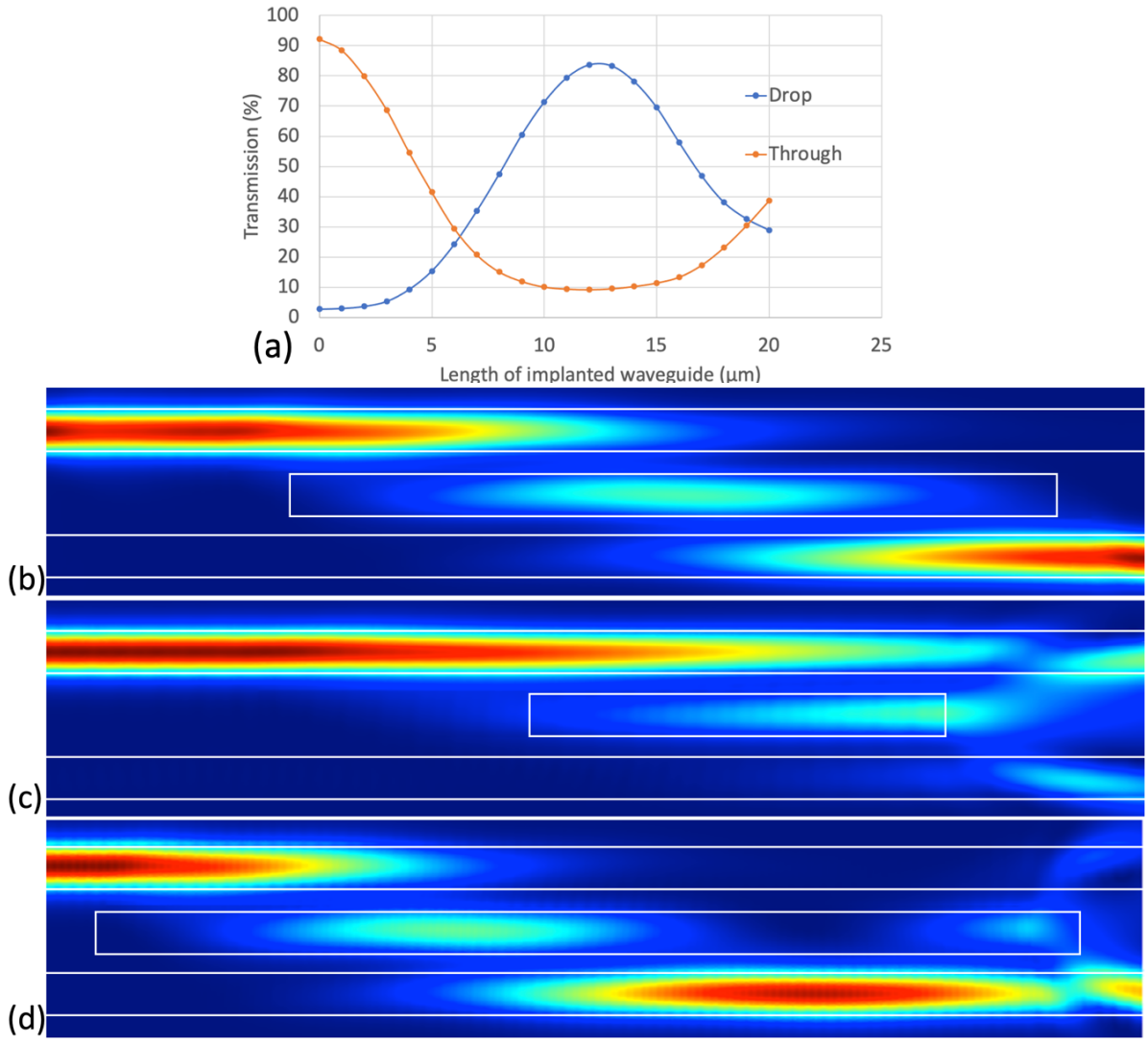

Figure 4.17 - (a) Simulated transmission of implanted DC as a function of implantation length. Simulated field profile of implanted DC with (b) 12μm, (c) 6μm and (d) 21μm implanted waveguide.

4.2 Heater design and thermal simulation

The thermal simulation for TiN heater was carried out using COMSOL. The target of this simulation is to design a TiN heater, which can heat the implantation section in the silicon waveguide to the annealing temperature. Based on previous work of our group, the annealing temperature of the implanted regions should be higher than 450°C. The temperature of the TiN filament and the surrounding SiO_2 should also be lower than their melting temperatures, which are 2930°C and 1710°C respectively [147, 148].

A 3D simulation structure was built in COMSOL. The thickness of the silicon waveguide is 220nm and the width is 500nm. The implanted region was also built into the waveguide structure. The

width and depth of this section was 400nm and 170nm, which came from previous simulation work [103]. The material used for this part was chosen as the amorphous silicon.

An SiO_2 cladding layer was positioned between the heater layer and silicon waveguide layer. The thickness of this layer heavily affects the thermal efficiency of the heater. The average thermal conductivity of SiO_2 fabricated by plasma-enhanced chemical vapour deposition (PECVD) is between 1.3 and 1.5W/mK, while the thermal conductivity of silicon is around 148W/mK. Therefore, for achieving higher thermal efficiency, the thickness of this SiO_2 layer should be as thin as possible. However, the TiN layer has a very high absorption coefficient to the optical signal. Figure 4.18 shows the simulated optical transmission of a 40µm long waveguide with a 10µm long TiN heater on top. As the thickness of SiO_2 layer reached 400nm, the optical loss caused by absorption dropped to around 5% (-0.2dB). In the fabrication process, the thickness of the SiO_2 layer will be controlled to be greater than 400nm. Therefore, the maximum optical loss induced by one TiN heater is smaller than 0.2dB. The thickness of 400nm is used for the SiO_2 layer between waveguide layer and metal layer.

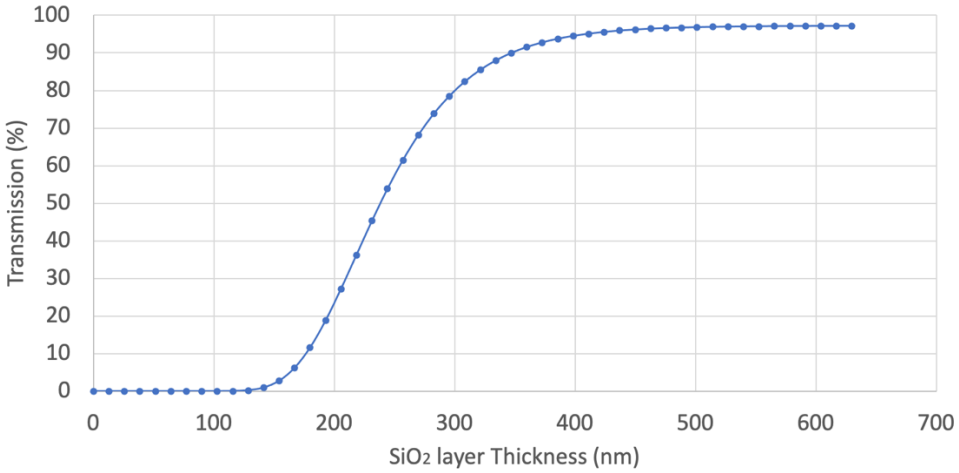

Figure 4.18 - Propagation loss of 10µm length and 1µm width heater on top of waveguide versus thickness of SiO_2 layer.

The heater layer only consists of the TiN filament, which was shown in Figure 4.19. The position of the filament is designed to extend beyond the implantation section in waveguide. In this simulation, the width and length of filament were 1µm and 12µm respectively, while the length of implanted section was 10µm.

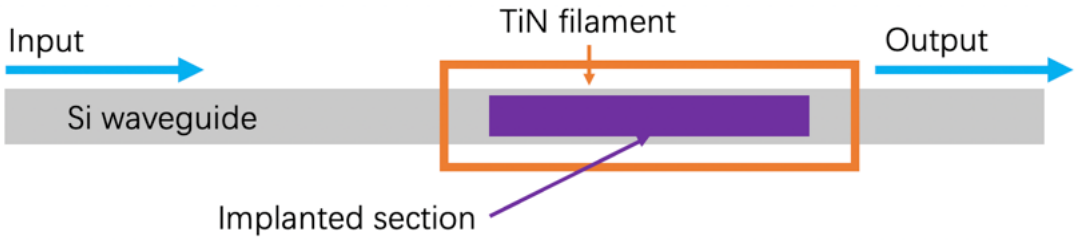

Figure 4.19 - Top view of heater on implanted waveguide.

Figure 4.20 gives the cross-sectional temperature distribution of the implanted waveguide with a 100nm cladding layer. The temperature of the implanted section has reached the annealing temperature, which is over 450℃ [104]. When the applied voltage comes to 7.8V for a 12μm long and 1μm wide filament, the temperature of the filament has reached over 1730℃. The surrounding SiO_2 will have reach its melting temperature, which could result in failure of this heating system. Therefore, in the experiments, the applied voltage should increase from 0V and be controlled under 7.8V. Due to the variations of TiN layer's properties and the dimension variations, the resistance may vary. In this project, the length of filament also changes with the length of implantation section, which is shown in Appendix A, therefore the maximum voltage allowed may be slightly different. This will be discussed in detail in the following experiments.

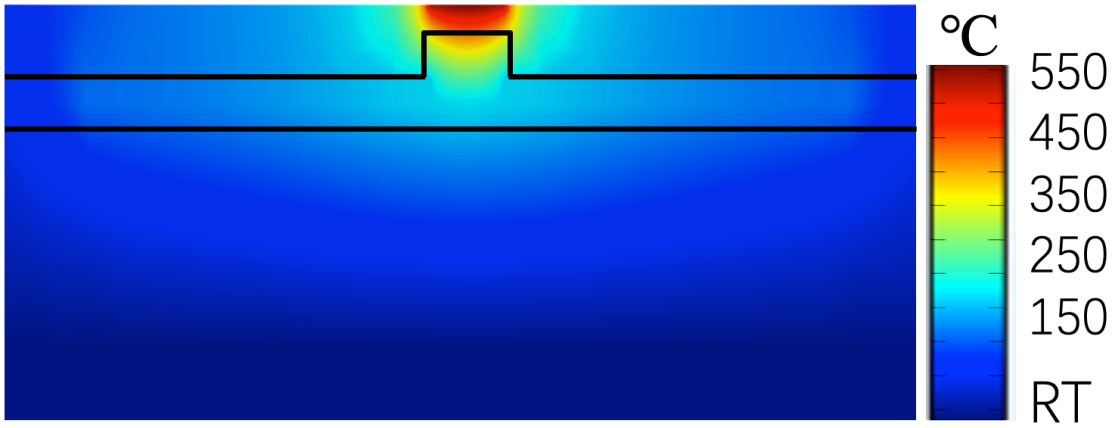

Figure 4.20 - Simulated temperature distribution under 5V applied voltage.

4.3 Device fabrication processes

Figure 4.21 gives the fabrication processes of implanted optical devices on an eight-inch SOI wafer. The patterns of all structures were fabricated by deep ultraviolet (DUV) photolithography in the Nanofabrication Centre at University of Southampton. Grating couplers are positioned at the input and output of waveguides to efficiently couple light (TE polarised) from and to single-mode optical fibres used for measurements. The grating etch depth is 70 nm with 630 nm period and 50% duty cycle. These are standard grating designs used routinely by our group. After the plasmatherm etching process, the photoresist on the wafer is removed via the ashing process for 6 minutes. Then the wafer is transferred to the wet room for an RCA1 cleaning process. RCA1

cleaning uses a solution consisting of 5 parts of deionised water, 1 part of ammonia and 1 part of aqueous H_2O_2 to clean the organic residuals. The cleaning time is 5 minutes, and the temperature is 50℃. After this cleaning process, the wafer was sent to the DUV lithography facility for patterning of the waveguide layer. The etching depth for rib waveguides was 120nm leaving an approximately 100nm thick slab layer. The same ashing and RCA1 cleaning processes were carried out after the etching process. After the fabrication process of all the optical waveguides and devices has been finished, a 300nm thick SiO_2 layer and 400nm thick photoresist were used as a hard mask and a soft mask respectively for the ion implantation process. The SiO_2 hard mask is fabricated by a PECVD process and etched by the plasmatherm process, leaving a 20nm SiO_2 layer to protect the surface of waveguide during the ion implantation process. The ion implantation process was carried out by the Ion Beam Centre at the University of Surrey. The ion implantation energy was 130KeV with a dose of 1×10^{15} ions/cm^2. Approximately 80% of the lattice is disordered [100]. After the implantation process, the photoresist is firstly cleaned via ashing and RCA1 cleaning, and the SiO_2 layer on the top of waveguides is removed by HF etching. For devices used for laser annealing, the cladding layer on top of waveguide layer is approximately 20nm SiO_2, so no further fabrication processes were needed for those devices.

For devices integrated with thermal heaters shown in Figure 4.21 (f), a SiO_2 cladding layer with 400nm thickness was deposited at the top of waveguide layer before the deposition of the metal layer. This SiO_2 cladding layer was intended to be thick enough to prevent optical absorption by the metal. The TiN filaments were fabricated at the top of implantation region. The length of TiN filament was designed as 2μm longer than the implanted section in the waveguides, to achieve a better thermal annealing effect. The TiN filaments are deposited in a sputtering process and developed via a lift-off process. The photoresist is cleaned by a reactive ion etching (RIE) process. Another 500nm thick SiO_2 protection layer for the filament was deposited on top of metal layer. This cladding layer aims to prevent the TiN filament becoming oxidised in the air when the temperature rises over 400 degrees. The vertical hole in this 500nm thick SiO_2 protection layer is etched by HF wet etching. After transferring the pattern of the contact pads, a 500nm Al layer is deposited on top of wafer. The contact pads are also fabricated by the lift-off process. After the approximately 24 hours lift-off, the final resist layer is deposited on top of the wafer. This resist layer is used to protect the chip from the dust pollution in dicing process. The final step is dicing this 8-inch wafer into chips, and cleaning the resist.

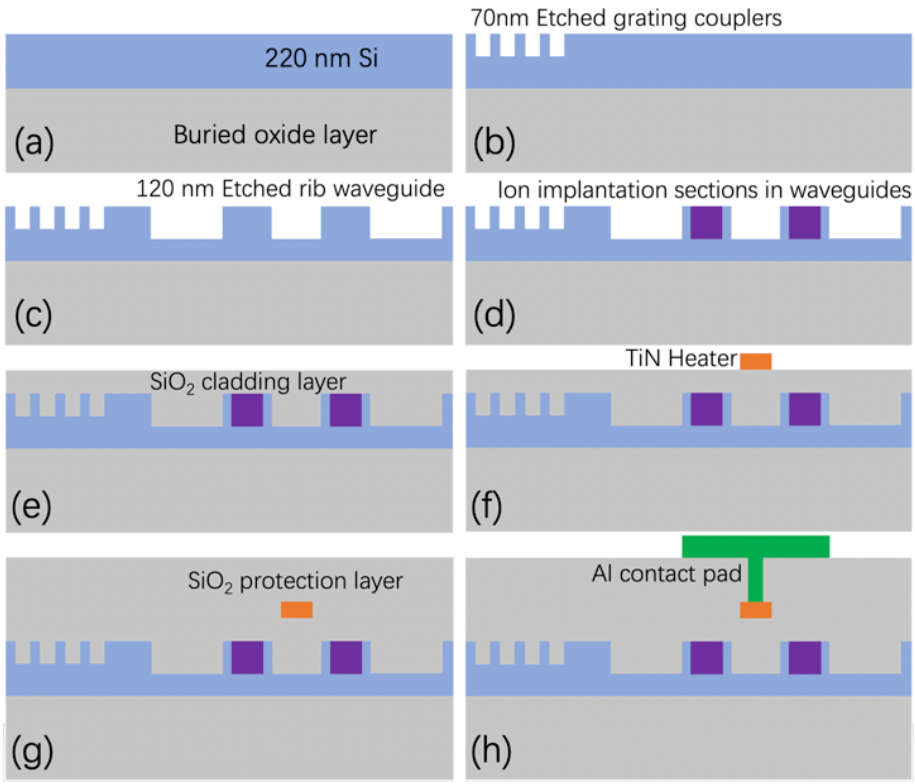

Figure 4.21 - Fabrication processes of implanted MZI: (a) SOI wafer; (b) Etched grating couplers; (c) Etched rib waveguides; (d) Ge ion implantation; (e) SiO_2 cladding layer; (f) TiN heater; (g) SiO_2 protection layer; (h) Al contact pad.

Similar fabrication processes have been carried out for implanted ring resonators, racetrack resonators and directional couplers. In this project, ring resonators use the same dimensions of rib waveguides as used in the MZIs. For rib waveguides in the implanted directional couplers, the etching depth is only 70nm, leaving enough height to form implanted waveguide in the slab layer.

Figure 4.22 shows the mask layout for TiN heaters on top of optical devices. Due to the fabrication variations, and errors, the dimensions and performance of some devices will shift. For examples, the gap between waveguides in the coupling regions of ring resonators and DCs will affect the coupling efficiency. The width of an implanted waveguide will affect the effective index of its fundamental mode, and then affect the coupling efficiency. Therefore, the parameter sweeping is carried out in our mask design. In the implanted DCs, the gaps between conventional waveguides and implanted waveguides were designed as 230nm, 250nm, 280nm. The width of implanted waveguides were designed as 520nm, 540nm, 560nm, 580nm, 600nm. In the implanted ring resonators, the gaps between straight waveguides and ring waveguides were designed as 220nm, 240nm, 260nm, 280nm 300nm and 320nm,

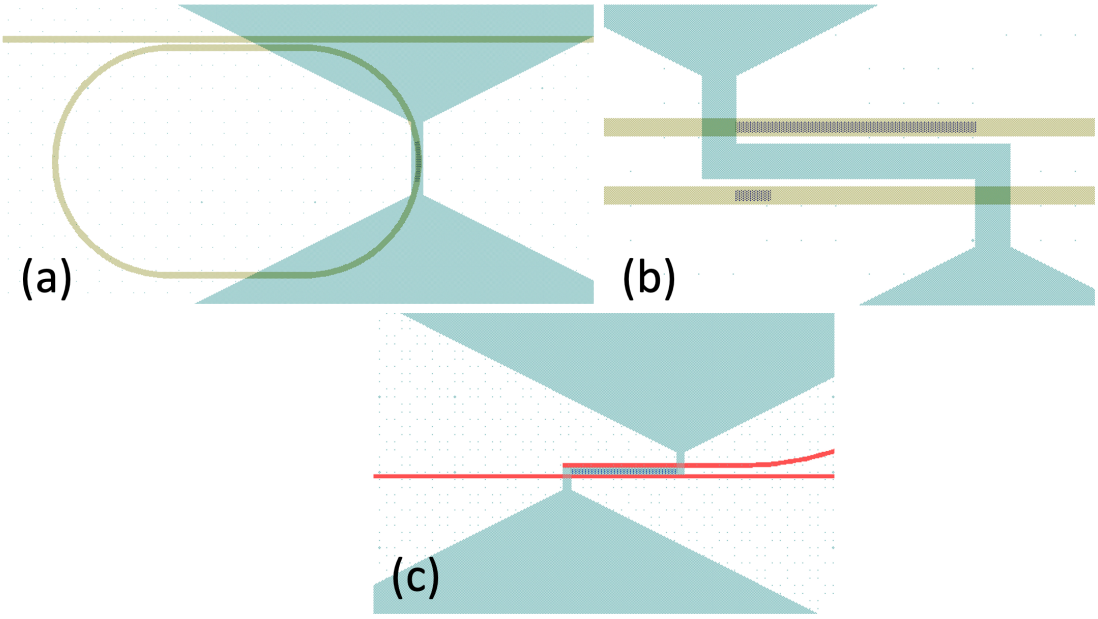

Figure 4.22 - Mask design for (a) racetrack resonator, (b) MZI and (c) two-stage DC.

4.4 Summary

In this chapter, the design, simulation and fabrication processes of implanted optical devices are introduced and discussed. Their optical performance, such as resonant wavelength of ring resonators, coupling coefficient of racetrack resonators, transmission of MZIs and coupling efficiency of DCs can be changed after the ion implantation process. These implantation sections and waveguides can be further modified or removed via annealing processes, including laser annealing and integrated electrical annealing. The annealing experiments will be discussed in chapters 6-8.

Chapter 5 Experimental setups for annealing and device characterisation

This chapter introduces all the experiment setups that were used in this project. The implanted optical devices can be annealed by continuous wave laser, pulsed laser, and electrical thermal power. The optical transmission of devices before and after annealing were measured by optical characterisation setups. For the pulsed laser annealing setups, the real-time monitoring of optical transmission can be achieved.

5.1 Continuous wave laser annealing setup

The CW laser annealing setup is shown in figure 5.1 and figure 5.2. It was designed to deliver the laser power to the amorphous silicon in a controlled and precise manner. A CW Argon ion laser was used as the source. In the figure 5.1, PBS is the polarisation beam splitter. BS is pellicle beam splitter. MO is the microscope objective. The output power was adjusted using a half wave plate and a polarisation cube splitter. The laser beam was focused onto the sample's top surface using a 10× microscope objective, producing a 4.7 µm diameter spot. The chip sample was positioned via a set of linear micro-precision linear stages, so that the laser spot can scan across the target waveguides precisely. A pellicle beam splitter and a charge-coupled device (CCD) camera were used for imaging and control. Using the correct combination of laser power and scanning speed, sufficient thermal energy was transferred to the amorphous silicon material to partially or fully re-crystallise the Si material, thus, modifying its optical properties.

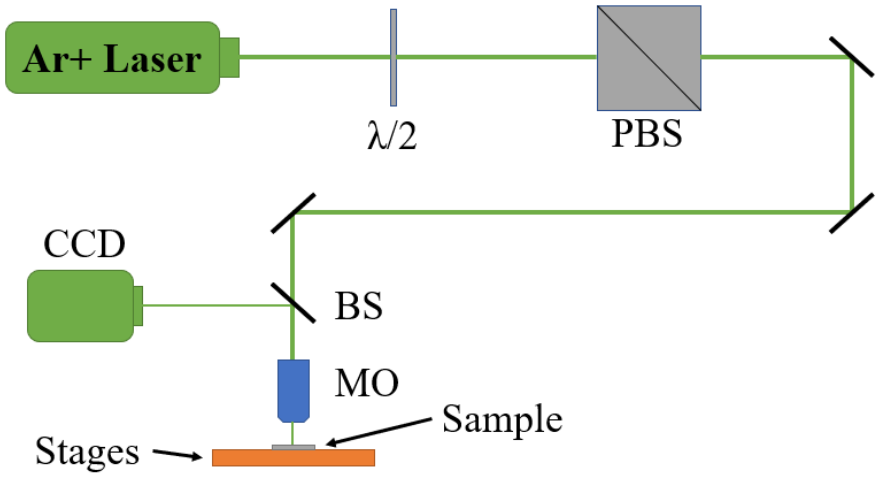

Figure 5.1 - Schematic of CW laser annealing setup. $\lambda/2$ represent the half-wave plate. And BS is a beam splitter. PBS is a polarizing beam splitter. CCD is a charge coupled device. MO is a microscope objective.

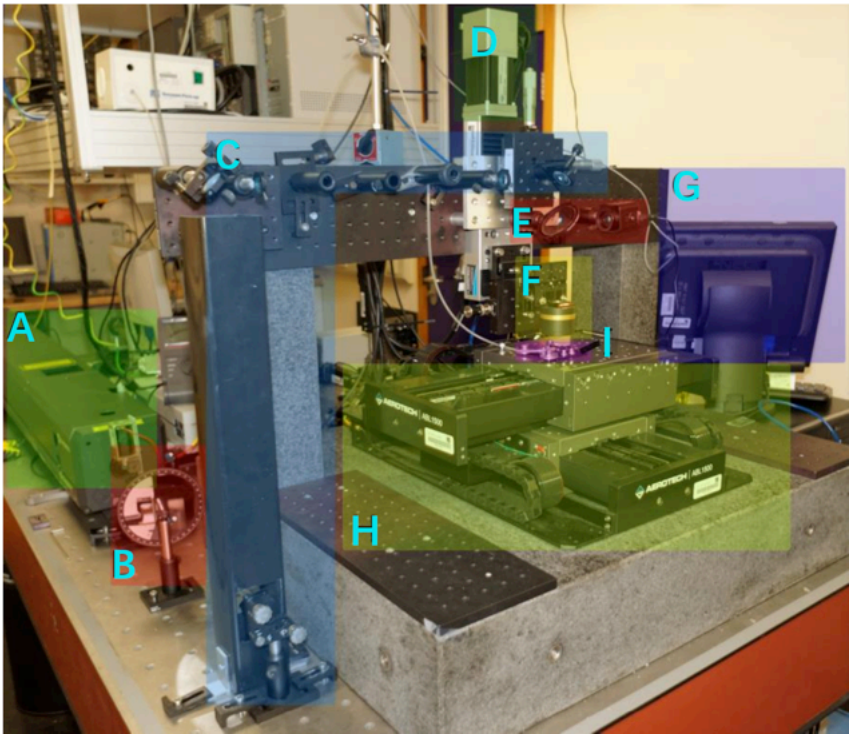

Figure 5.2 – Image of continuous wave laser annealing setup [100].

A) 488 nm Argon-Ion Laser
B) Variable attenuator
C) Beam steering equipment
D) Lens adjustment motor
E) Bean splitter and sample alignment camera
F) Mirror lens
G) Control computer
H) Pneumatic XY stage
I) Vacuum sample mount

5.2 Pulsed laser real-time annealing setup

5.2.1 Annealing setup with real-time spectrum monitoring

Pulsed lasers can also be used for annealing the ion implanted silicon waveguides [133]. One of our setups with pulsed laser annealing is illustrated in figure 5.3; a real-time optical monitoring and feedback system was implemented to achieve higher trimming accuracy. A pulsed laser source at 400 nm wavelength was generated from the second harmonics of a femto-second laser (Coherent Chameleon, pulse duration 200 fs, repetition rate 80 MHz). The laser spot was focused onto the implanted sections using a microscope objective (Mitutoyo, 100X, 0.5NA). Meanwhile, an optical signal was generated by an optical parametric oscillator (Chameleon Compact OPO), providing 200-fs pulses at 1550 nm with a 20 nm bandwidth. The optical signal was launched to the input fibre and coupled into the sample silicon chip using a grating coupler. The output signal from the silicon chip was collected and analysed by a grating spectrometer equipped with an

InGaAs CCD array (Andor). The spectrometer can also be replaced by a photodiode detecting the intensity of optical signal. The sample silicon chip was fixed on a 3D piezo stage as the position of pump laser can be moved precisely along the implanted sections.

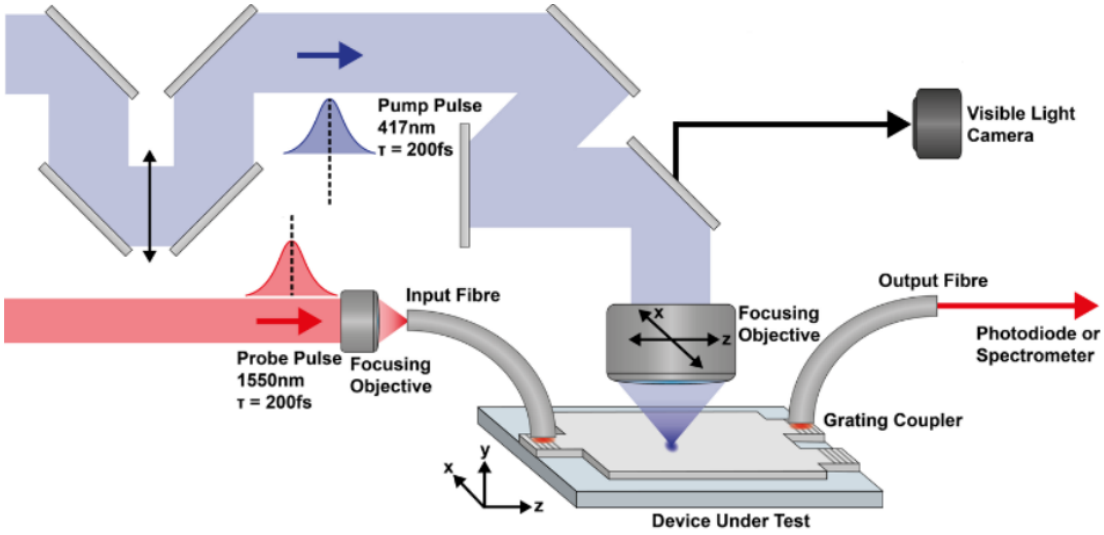

Figure 5.3 - Pulsed laser annealing setup with real-time spectrum monitoring.

5.2.2 Annealing setup with real-time gradient feedback

Figure 5.4 illustrates the pulsed laser annealing setup with real-time gradient feedback of the optical signal. The signal source was replaced by a narrow line tuneable laser at 1550nm with 20nm bandwidth. Therefore, the transmission detected at the through port will change with the shifting resonance during the annealing process. The transmission of through port will reach its minimum while the resonance is trimmed to the probe wavelength. However, using this absolute transmission for decision making has two disadvantages in an annealing experiment. The minimum location can only be observed once the transmission has passed it. Additionally, the accuracy of measured transmission will suffer from drifts of coupling with fibres, laser fluctuations and environment factors, such as temperature shift.

Differential measurements to an external perturbation can provide more reliable information to the annealing process. The relative variation, normalised to the transmission, can be obtained as gradient feedback of the annealing process. The frequency of this feedback is the same with induced perturbation in the whole experiment system. An optical chopper worked at 80Hz was added to pulsed laser pump signal which act as the perturbation, which is the thermo-optic effect from pump light to the refractive index of the waveguide. A lock-in amplifier, which has the same frequency of the chopper, was used to replace the spectrometer used in the previous real-time optical spectrum monitoring and feedback system. In this project, we use the photomodulation response, providing a derivative of detected transmission. The zero value of this derivative

represent the absolute transmission reaching its minimum. Compared with the former experimental setup, this system allows sensitive extinction of the feedback optical signal even with high noise.

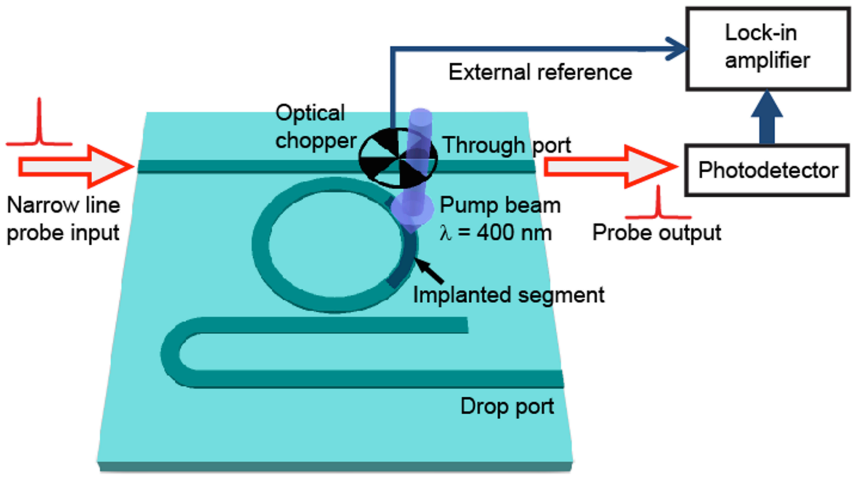

Figure 5.4 - Pulsed laser annealing setup with real-time gradient feedback [149].

5.3 Optical characterisation and electrical annealing setup

All the optical measurements of our silicon photonics chips were carried out at the University of Southampton. Figure 5.5 shows a sketch of the experimental setup for optical characterisation. The blue line represents the electrical signal connection, and the black line represents the transmission of the optical signal. The tuneable laser module (81940A) and optical power sensor module (81634B) are integrated into an Agilent 8163B lightwave multimeter. The light source from a tuneable laser was first converted to TE mode by a polarisation controller and then coupled into the sample photonic chip. The optical signal is coupled into and out from the chip through grating couplers. The output light is detected by an optical power sensor. The laser source and optical power sensor were connected and controlled by a personal computer (PC).

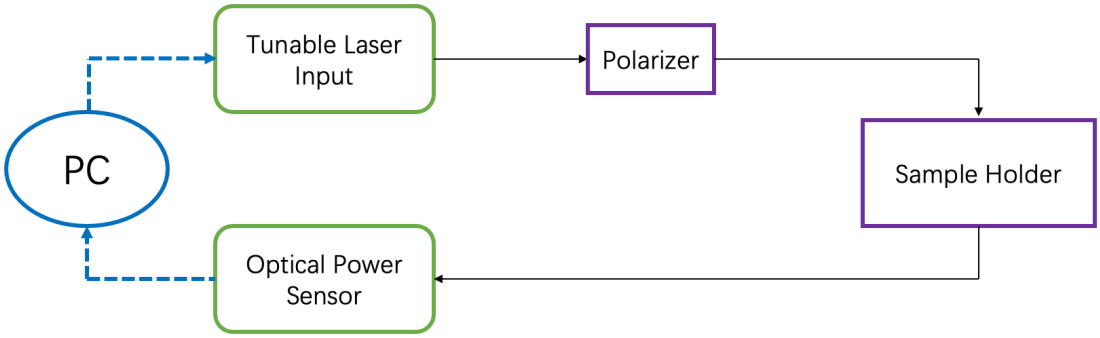

Figure 5.5 - Schematic of optical characterisation setup.

Figure 5.6 shows the electrical annealing setup used in this project. A DC power source was used to apply voltage to the integrated TiN filaments on the chip and heat the implantation area of the

optical devices. The instrument used in this project include an Agilent E3640A with the voltage range from 0V to 8V and a Keithley 6487 multimeter with the maximum current limit of 20mA. The power source can be locally controlled or controlled by an external computer using a Python program. The contact pads of integrated heaters were connected with a power supply by pins and electrical wires. In Appendix B, all the Python codes used to control these instruments are listed.

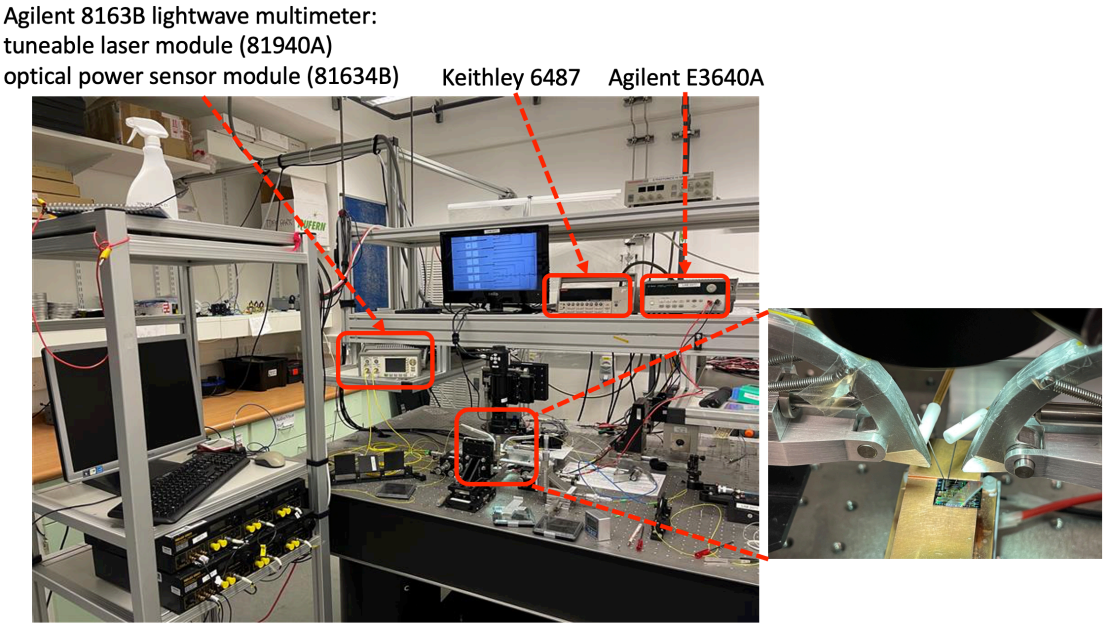

Figure 5.6 - Electrical thermal annealing and optical characterisation setups.

5.4 Summary

The implanted region of waveguide can be heated up through the irradiation of CW laser and pulsed laser. The annealing effect can be realized. During the annealing process, the transmission of optical device is characterized on this measuring stage. In this project, the integrated filament is used to achieve the annealing process for implanted devices on the optical characterized setup.

Chapter 6 Experiment results: ring resonators trimming

The ring resonator is one of the most important optical devices for integrated photonic circuits. It is widely studied for optical filtering, optical multiplexing, wavelength conversion, photonic logic gates, and modulation applications. However, ring resonator is sensitive to fabrication errors [104, 107, 145]. In this chapter, a post-fabrication trimming method, based on ion implantation and annealing techniques, is utilised to alter the resonant wavelength and the coupling state of a ring resonator.

6.1 CW laser annealing of racetrack resonator

The design of devices used in this experiment and their fabrication processes were described in chapter 4. Figure 6.1 (a) gives the schematic of racetrack resonator. The racetrack resonator was designed with the radius of 25µm and coupling length of 10µm. The slab region between the racetrack waveguide and the bus waveguide is implanted with Ge ions. Due to this implanted section, the coupling efficiency between bus waveguide and racetrack waveguide has been changed. The resonant wavelength and extinction ratio of this racetrack can be subsequently trimmed by fully or partially erasing the implantation section via annealing. The unimplanted racetrack resonators were also fabricated with the same dimensions as the implanted ones, and used for reference experiments.

An optical microscope image of a fabricated racetrack resonator is shown in figure 6.1 (b). There is a small square on the top of the straight waveguide, which was designed for laser alignment with the implantation section. The left side of this square is aligned vertically with the starting point of the implanted section between the straight waveguide and ring waveguide. In the laser annealing experiment, the laser spot was firstly aligned to the left-hand side of this square. The implanted region can be gradually annealed as the laser spot is moved vertically down and across the waveguides.

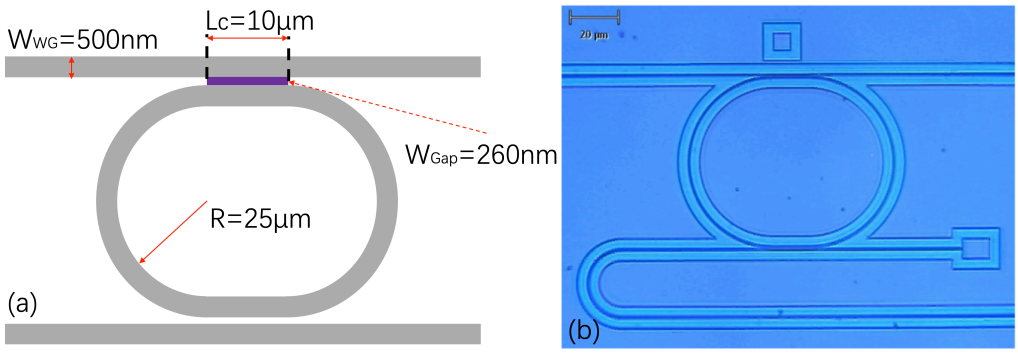

Figure 6.1 - (a) Top view of racetrack with implanted coupling region. (b) An optical microscope image of the fabricated racetrack resonator [150].

The optical transmission of the racetrack resonator with the same design was also simulated in Lumerical Mode solution. Figure 6.2 shows the simulated and experimental transmission spectrum of the unimplanted racetrack resonators. The blue line is the simulated transmission spectrum. The free-spectral range (FSR) of the simulated racetrack is around 3.4nm and the simulated and measured extinction ratios are higher than 25dB. The insertion loss of simulated device is 0.89dB while the dimensions of simulated SOI wafer consist of a 220nm top silicon layer and 2µm buried oxide layer. The Q factor for the simulated racetrack was 1800 while the FWHM (full width of half maximum) is 0.85nm. The fabrication process tolerances may cause variations in device parameters such as etching depth, deposition thickness, waveguide width, and even the thickness of SOI wafer can affect device performance. The measured spectrum is shown as the red line in figure 6.2. The FSR for the measured racetrack is the same as the simulation. Its extinction ratio is also higher than 25dB. However, the insertion loss of this device was 1.83dB at 1550nm, which was greater than the simulated one. Thus, the extinction ratio of measurement results should lower than the simulation results. In figure 6.2, all the measured extinction ratios are less than the simulated ones except for the resonance around 1560nm. This difference comes from the resolution limitation of the monitor in the simulator.

The insertional loss around 1550nm was caused by the imperfect waveguide etching processes and shift of gap between straight waveguide and ring waveguide, leading to additional optical loss. The difference between measured and simulated resonant wavelength comes from the shift of effective index causing by the fabrication variations.

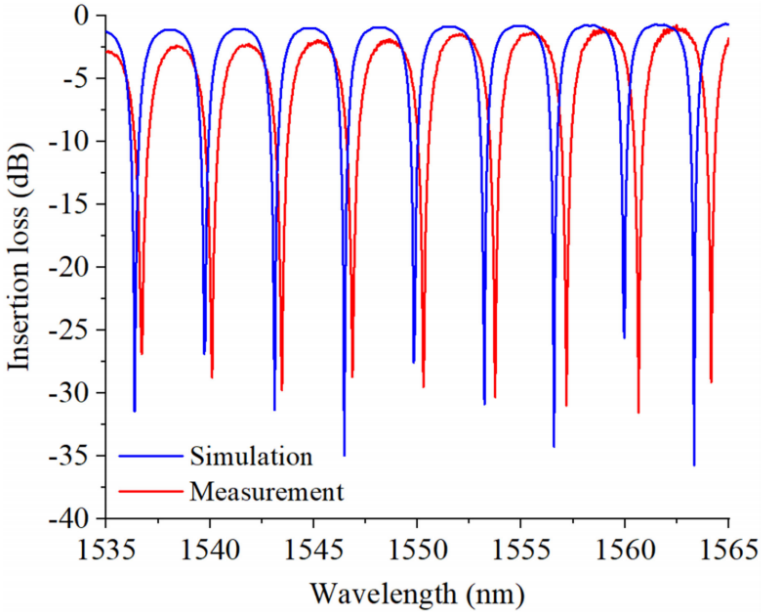

Figure 6.2 - Transmission spectrum showing the difference between simulation and experimental results of un-implanted racetrack resonators [150].

A high-power CW laser is used to anneal the implanted sections in the racetracks. For achieving high power density on the surface of chip, a 20× microscope objective was used. Under this

condition, the diameter of laser spot on the surface of chip was approximately 2.5µm. The laser spot was moved cross the implantation area to anneal the implantation area in a pattern shown in figure 6.3. The laser spot shifts 1µm each step to the right side after every annealing cycle. In one annealing cycle, the laser spot moved 30µm from top to bottom to pass through the implanted region. After ten annealing cycles, the implanted section between the waveguides can be fully scanned.

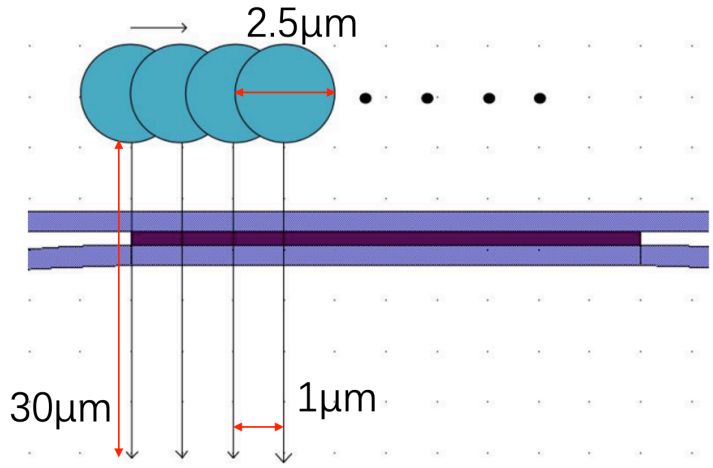

Figure 6.3 - Scanning path of laser spot.

Raman spectroscopy has been used in lattice structure analysis and research [151, 152]. This can be used to identify the lattice structure of the silicon waveguide before and after laser annealing with different laser powers. Three different power levels of annealing laser were used (25mW, 35mW and 45mW) to anneal implanted silicon waveguides, while keeping the scanning speed constant at 10µm/s. In the Raman spectroscopy measurement, a 0.2 mW Nd:YAG laser source (532 nm) has been used. This laser power is much lower than the annealing laser, therefore will not induce permanent changes to the implanted region. The exposure time is 10 seconds for the three samples using a 50× objective lens. Experimental results are shown in figure 6.4.

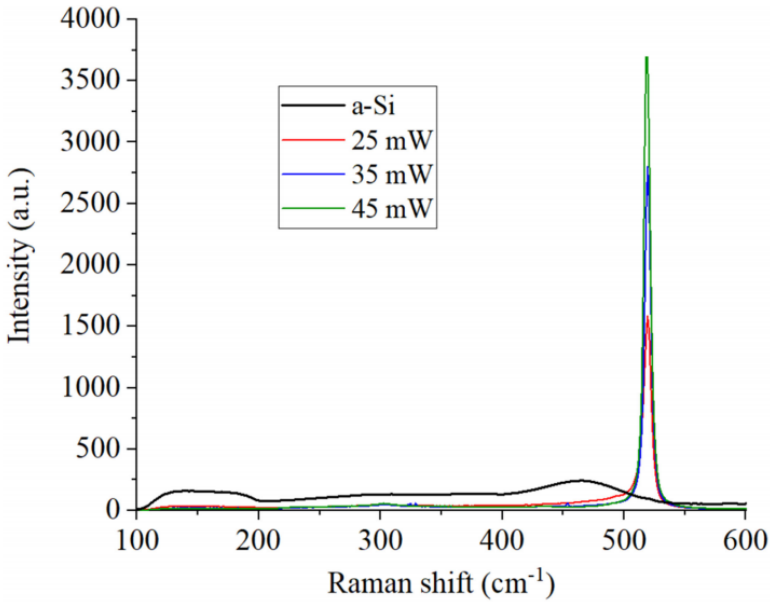

Figure 6.4 - Raman spectra of Ge implanted silicon before (amorphous Si) and after annealing using three different power levels of the annealing laser [150].

In figure 6.4, the Raman spectrum of implanted silicon, shown as black line, has two broad peaks at 150 cm^{-1} and 480 cm^{-1}. This gives the information that the amorphous silicon section had been successfully formed in crystalline silicon waveguide after Ge ion implantation, because the amorphous silicon can provide these two vibrational bands [151, 152]. The Raman spectrum of the implanted section annealed by 25 mW laser is shown as the red line. A tiny broad peak at 150 cm^{-1} was observed, indicating an annealing power of 25mW cannot achieve the temperature for full re-crystallisation of the implanted region in silicon material. Nevertheless, 25mW laser power can still provide the partial annealing for amorphous silicon because the characteristic peak associated with crystalline silicon was observed at 520 cm^{-1}. Annealing with a higher laser power resulted in a higher temperature on the surface of chip. The single silicon peaks at 520 cm^{-1} increases in amplitude when the laser power is 35mW and 45mW, which are shown as the blue line and the green line. There are also small peaks close to 300 cm^{-1} peak for all the Raman spectrum of annealed section. This peak is the Raman mode of pure silicon [153]. Therefore, the lattice structure of annealed section is close to crystalline silicon.

Based on these results, 35mW and 45mW are used as the experimental annealing laser power. Figure 6.5 shows the measured transmission spectra, including an unimplanted racetrack resonator and implanted racetrack resonators with various annealing lengths, which were annealed by the laser using two different power levels. These power levels of the annealing laser are in a very good agreement with the laser power used by my colleagues, Dr. Milan Milosevic and Dr. Xia Chen. In their previous work on ion implantation trimming of different ring resonators and MZIs were explored, and the results revealed that the change of refractive index is similar as

the alternative annealing method using the rapid thermal annealing technique (in the temperature range of 450-500 °C, carried out for 1 min) [103, 104].

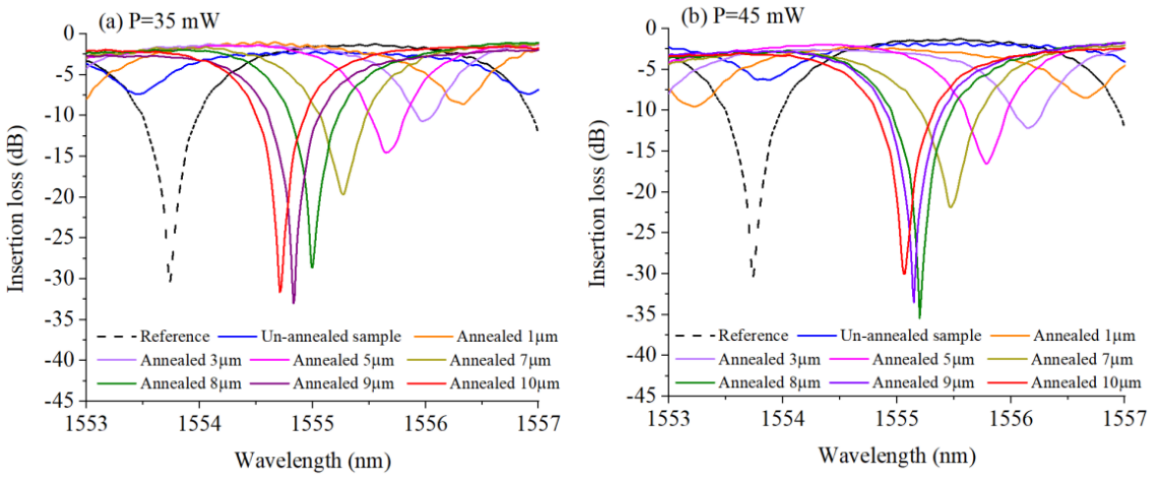

Figure 6.5 - Transmission spectra of ring resonators with various implantation lengths. (a) Annealing laser power was equal to 35mW; (b) Annealing laser power was equal to 45mW [150].

The implanted sections are gradually annealed and removed from racetrack resonators. The coupling efficiency will be changed during this process. The resonant wavelength and extinction ratio can therefore be trimmed. In figure 6.5, the resonant wavelength for each device shows a blue shift with increasing of the annealing length. The maximum shift of the resonant wavelength is ~2.5nm, while the whole implanted section is fully annealed.

Figure 6.5 indicates that it is possible to adjust the extinction ratio of racetrack resonators using this laser annealing technique. A range of different extinction ratios was obtained for different laser power levels and annealing length. Annealing lengths of 8 and 9 μm provided an improvement in extinction ratio compared with the unimplanted devices. The unimplanted resonator (reference) was measured, and its extinction ratio is 28dB. The extinction ratio of 30dB has been measured for the implanted resonator (annealed by the laser power of 35mW) with an annealed length of 9μm. For the laser power of 45mW, the improved extinction ratio of 34dB has been achieved with an annealed length of 8μm. This difference is caused by the additional annealing effect of implanted region, which is brought by the higher laser power. In both figure 6.5 (a) and figure 6.5 (b), the extinction ratios increase with the annealing length and get the closest to the critical coupling at the purple curve and green curve respectively, providing the highest extinction ratio. With the further annealing, the extinction ratios decrease. Based on the theory mentioned in chapter 3, this is because the coupling loss for these two rings become smaller than round trip loss in ring waveguides. Then this ring resonator achieved under coupling.

6.2 Pulse laser annealing of ring resonator and real-time monitoring

Similar to the CW laser, a pulsed laser can also induce an annealing effect into an implanted silicon waveguide. In commercial applications, such as sensing and optical modulators, real-time monitoring of optical transmission of devices during the trimming process is necessary to improve the trimming accuracy. The pulsed laser annealing setup has been shown in chapter 5. The design and fabrication processes of implanted ring resonators have been discussed in chapter 4. A 30-µm-radius ring resonator used in this experiment has been partially implanted with Ge ions. The implanted range is denoted as the angle of the arc, which is varied with different testing devices. In this experiment, the angle of the arc is 22°; correspondingly, the length of the implantation region is approximately 11.5µm. The implanted region was gradually annealed by pulsed laser annealing, shown in figure 6.6 (a). The resonant wavelengths of these devices show a similar trend as the racetrack resonators mentioned in the last section during laser annealing. Figure 6.6 (b) shows the measured resonant wavelength shift of the implanted ring as a function of the annealing length. Before the annealing, the FSR and extinction ratio for the resonant wavelength near 1550nm were 3.19µm and 15dB respectively. The corresponding Q factor is 755.

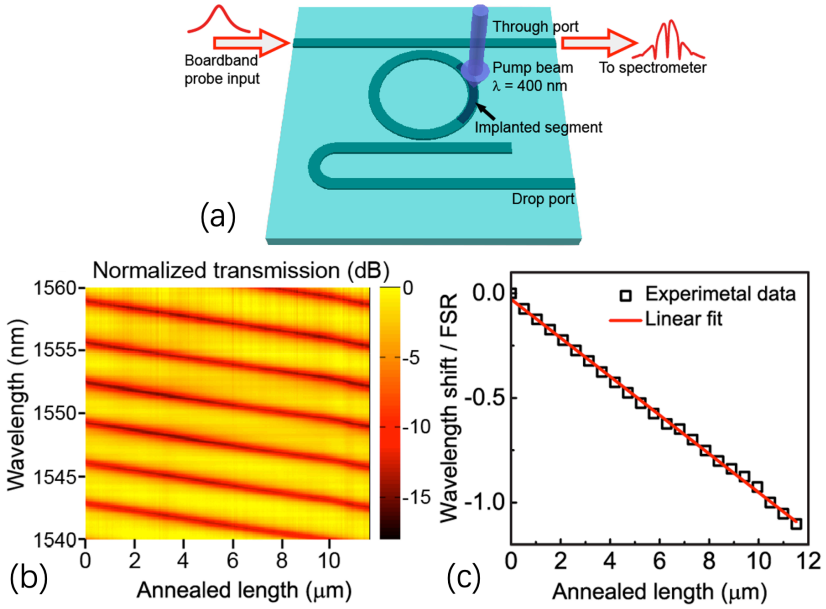

Figure 6.6 - (a) Experiment setup for laser annealing of implanted ring resonators with real-time spectrum monitoring. (b) Measured resonant wavelength shift of the ring as a function of annealing length. (c) Measured resonant wavelength shift normalised to the FSR (in the range from 1540-1560nm) as annealing length was varied [149].

The resonant wavelength will shift as the implanted section is continuously annealed by the pulsed laser. The normalised spectrum shows a linear trend with a slope of approximately 0.09 μm^{-1}, which is shown in figure 6.6 (c). Compared with the former research, which presented a slope of 0.17 μm^{-1}, the method by using a pulsed laser can only give approximately half as much resonance shifting when the same length of implanted section is annealed [104]. This deviation is

caused by the limitation of laser power accumulated on the sample surface. The average laser intensity on the devices was around 8×10^5 W/cm^2 (4mW with a 0.8µm laser spot), which is much smaller than the CW laser (45mW with a 2µm laser spot). Even so, the demonstrated trimming range of the ring resonator was over one FSR which is sufficient for most applications. After laser annealing, the extinction ratio and Q factor of the resonant wavelength near 1550nm have improved to 16.5dB and 830 respectively. This Q factor can be further improved by utilising more fully annealing effect of implanted region.

In this experiment, there was also a systematic error of the resultant spectra caused by the high temperature at the time of annealing and the subsequent temperature drop of the ring resonator. Figure 6.7 shows the spectra shifting at the last annealing point and the state after cooling down to room temperature. This blue shift (0.2 nm) is attributed to a stationary thermo-optic effect. The actual shift after annealing could be smaller than 0.2nm, because the resolution of this spectrometer is 0.2nm. However, this systematic error can be removed by calibration of the process.

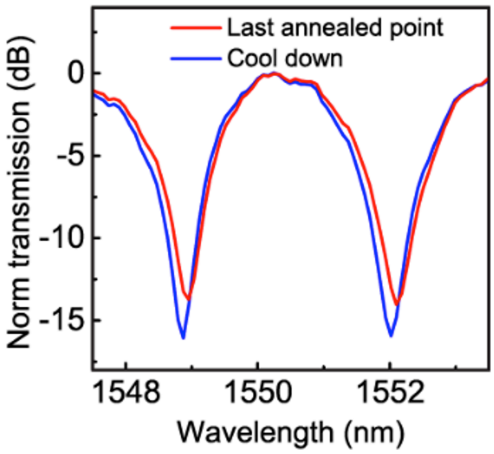

Figure 6.7 - Measurement spectrum of the last annealed point before and after cooling down [149].

6.3 Pulse laser annealing of racetrack resonator and real-time monitoring

The same experimental setup was also used to trim the implanted racetrack resonators. Figure 6.8 illustrates the experiment setup for these devices.

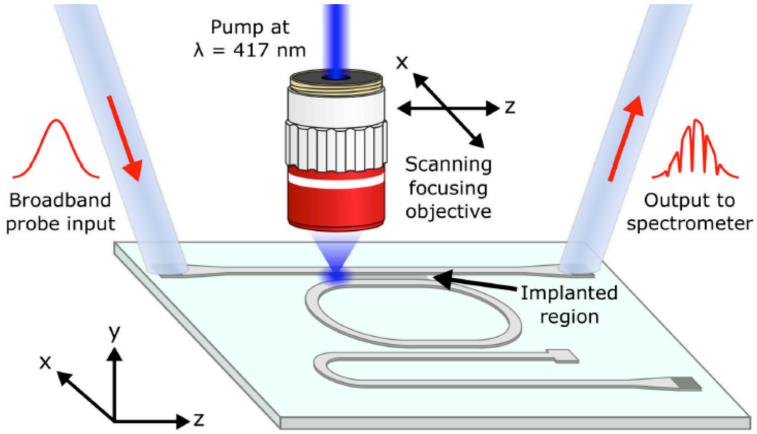

Figure 6.8 - Experimental setup used for pulse laser annealing of racetrack resonators [150].

This device has the same design as the devices discussed in section 6.1. The implantation region was located in the gap between straight waveguide and racetrack waveguide. During the annealing process, the pump spot was scanned along the implantation region while the optical output signal was detected and analysed by a spectrometer. Figure 6.9 (a) shows the dynamic shift of the real-time measured resonant wavelength during the annealing process in which the implanted region is fully scanned by the laser spot. The change of resonant wavelength is approximately 1nm and the extinction ratio increased to approximately 11dB from 4dB after the annealing, which is shown in figure 6.9 (b). The increase of extinction ratio and the shift of the trimmed resonant wavelength in this experiment are obviously smaller than in the CW laser annealing experiment discussed in section 6.1. This is caused by the different thermal power brought by the pulsed laser. In this experiment, the laser can only induce an average power of approximately 5mW. Therefore, the temperature of the implanted region induced by pulsed laser was lower than that temperature induced by the CW laser and only partial annealing was achieved [150].

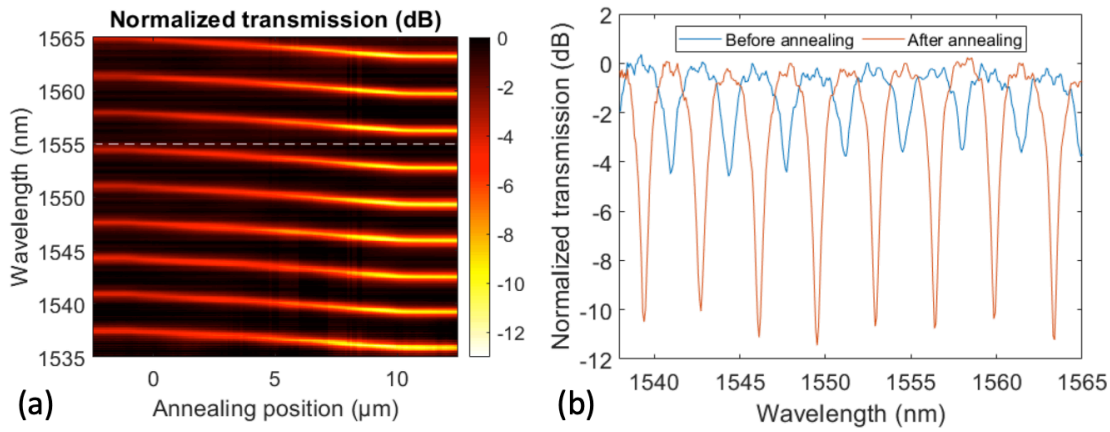

Figure 6.9 - (a) Measured resonant wavelength shift of the ring as a function of annealing length. (b) Normalised transmission of implanted racetrack resonator before and after pulse laser annealing [150].

This real-time monitoring system can provide more information about the annealing process. Figure 6.10 describes the extinction ratio of the implanted racetrack as a function of annealing length. The pulsed laser pump was kept on when scanning the whole 10µm implanted sections. Consider the left-hand side of implanted section as the starting position (0µm) of annealing. We can observe that the annealing process actually starts at the position of -0.5µm. This was caused by the diameter of laser spot being around 800nm. When the laser spot irradiated the position -0.5µm, the implanted section can still be heated and annealed by the laser power. The highest extinction ratio was achieved at an annealing length of 9.5µm. The results show a trend to saturation after 10µm, because the overall length of implantation section was annealed. When the annealing length passes 9µm, the extinction ratio drops a little because the coupling state of this ring resonator change to under coupling from critical coupling. After the annealing, the extinction ratio increased from 4dB to 11dB and the Q factor of this device also increased from 1260 to 1500 (FWHM of 1.07 nm at 1552.9 nm wavelength), indicating that the implanted region has been successfully annealed. As the implanted region is located in the gap between the straight waveguide and the racetrack waveguide, the coupling coefficient of this region is changed with the annealing of the implanted section. In addition, the resonant wavelength also shows a blue shift of approximately 2nm. These measured results agree well with the simulation results mentioned in chapter 4, indicating that the coupling coefficient of a racetrack resonator and its resonance can be shifted via Ge ion implantation and the subsequent annealing process.

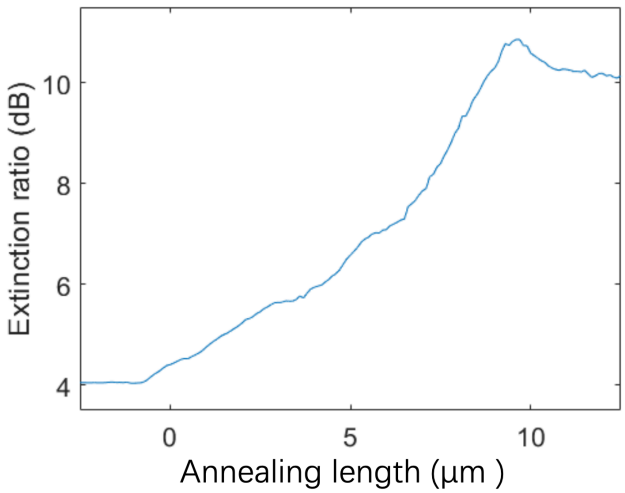

Figure 6.10 - Extinction ratio of implanted racetrack as a function of annealing length [150].

6.4 Electrical annealing of racetrack

In the previous sections 6.1, 6.2 and 6.3, the laser annealing of implanted sections has been demonstrated to implement post-fabrication trimming. The performance shift of a ring resonator, caused by fabrication variations, can therefore be corrected. However, laser annealing of each

device consists of alignment and scanning. Alignment is a time-consuming process, and this will decrease the throughput and increase the cost of industrial production. An electrical annealing method, realised by an integrated electrical heater, has many advantages over laser annealing as mentioned in previous sections of this thesis. Except for placing the electrical probes onto contact pads on the chip/wafer, no alignment process of annealing laser spot is needed. This advantage can increase the throughput of the trimming process. Furthermore, this method is also friendly for integration with electrical circuits. Finally, the annealing process can be realised using integrated thermal heaters, even after the devices are packaged. In this section, we report experimentally demonstrated trimming of ring resonators using electrical annealing.

Figure 6.11 shows the structure of an implanted racetrack with a TiN heater on top. The fabrication process has been described in the previous chapter 4. A short implantation section was induced into racetrack. The implanted section can be annealed by the integrated thermal heater. By annealing the implanted section in ring loop waveguide, the effective index of propagating mode, as well as the resonant wavelength, will gradually change as the lattice damages in waveguide are repaired.

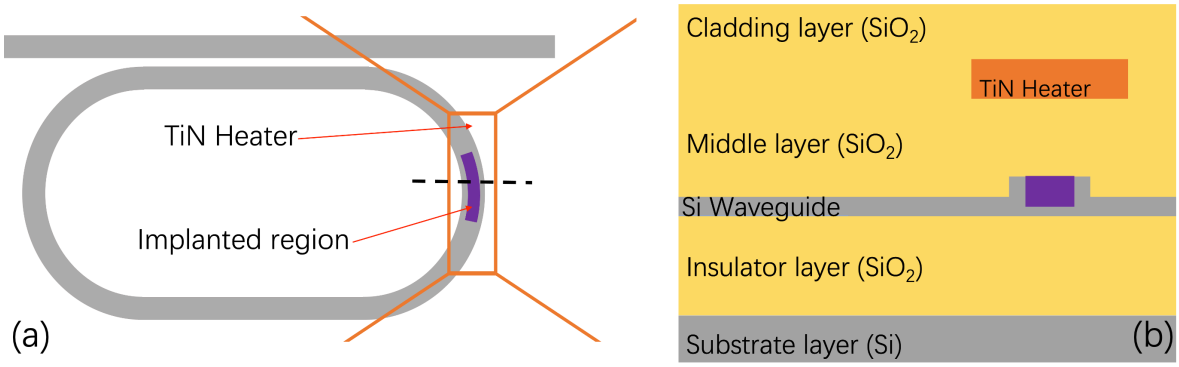

Figure 6.11 - (a) is the top view of an implanted racetrack with TiN heater on top and Ion implanted region is shown in purple colour. (b) is the cross-section of black dotted line position, not the zoomed image of (a).

Figure 6.12 summarises the experiment results of the operating resonant wavelength at a fixed electrical annealing voltage (and hence power) of 1.6V. The applied electrical power is around 43mW. Initially, the resonance peak was located at the wavelength of 1548.720nm and no changes happened as the applied voltage rose from 0V to 1.4V by a step of 0.2V. After the voltage reaches 1.6V and electrical power was maintained for approximately 10 seconds, the resonance wavelength was trimmed to 1548.415nm due to the annealing effect of the amorphous section in the ring waveguide. Each point in the transmission curve of figure 6.12 of this ring is measured at the same room temperature, after the electrical power is removed. The annealing temperature is the same for each annealing cycle as the same applied voltage results in the same electrical power. From figure 6.12, we can see that the shift of resonant wavelength decreases as the

annealing cycles progress, and the resonant wavelength eventually saturates, which is consistent with the annealing process resulting in a maximum level of crystal regrowth for a given applied temperature. The applied voltage of 1.6V provides the starting electrical power for annealing; the annealing speed is slower compared with the continuous laser annealing because the temperature of the amorphous section is lower than that in the laser annealing experiments. Figure 6.13 shows the simulated temperature for this racetrack resonator under 1.6V of applied voltage. The temperature of the implanted region in the waveguide is approximately 350℃, which is lower than the simulated temperature brought about by laser annealing, but clearly some level of annealing is occurring at this temperature.

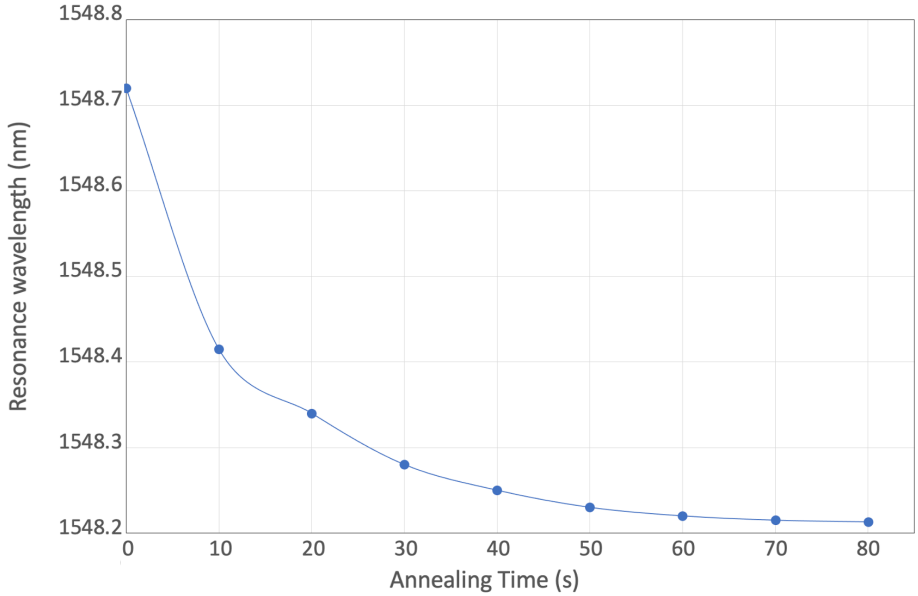

Figure 6.12 - Resonant wavelength as a function of annealing time under 1.6V applied voltage.

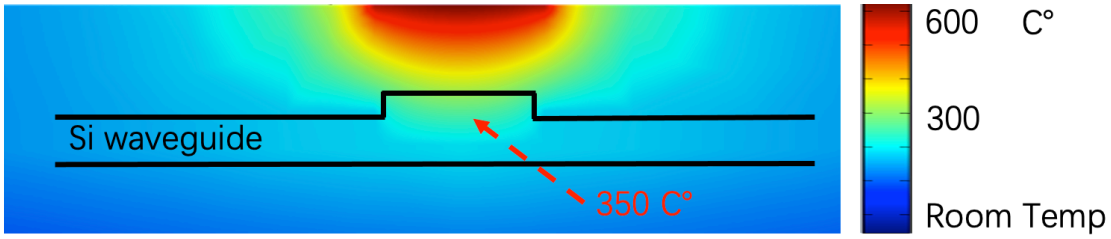

Figure 6.13 - Simulated temperature distribution of the racetrack resonator under 1.6V applied voltage.

For achieving a rapid annealing process, a higher applied voltage can be used. Figure 6.14 shows the resonance change after the device is annealed at a higher electrical power. The implanted section is not annealed when the applied voltage is only 1V. Therefore, the resonance remains the same as in the original transmission. For achieving the full annealing state for each annealing cycle, the electrical power supply needs to be applied continuously for 40 seconds. In figure 6.14, the electrical power for each point is 59mW, 120mW and 160mW, while the applied voltages are 2V, 3V and 4V respectively. The largest resonance shift is ~3.6nm achieved under an annealing power of 160mW. The trimming range is greater than in the laser annealing experiments

mentioned in former sections 6.1 and 6.3. This is caused by the variation in the size of the implanted region located in the ring waveguide, which can provide a greater change to the effective index for a longer implanted length.

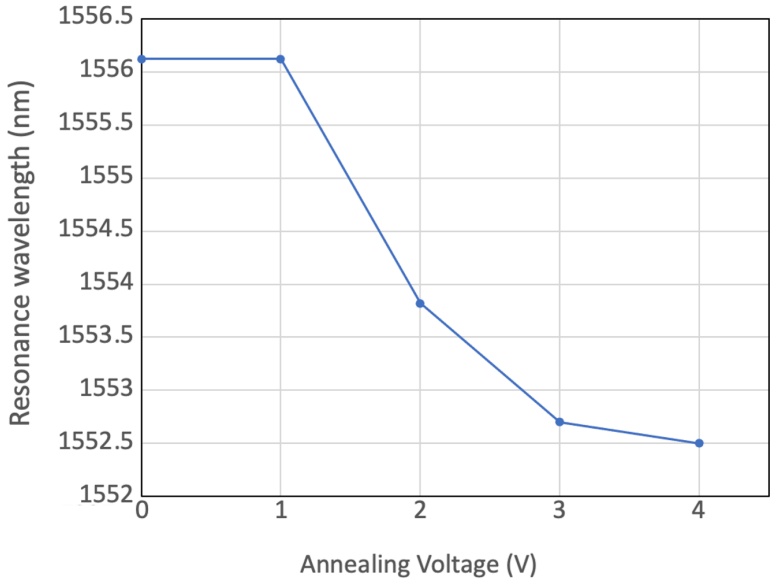

Figure 6.14 - Resonant wavelength as a function of applied voltage on racetrack.

6.5 Summary

This chapter discusses the experiments about the trimming of ring resonators by continuous wave lasers, pulsed lasers and integrated electrical heaters. The laser was firstly used to anneal the implanted section in ring resonators. The performance of these devices, such as the resonant wavelength and extinction ratio, can be changed with the annealing of the implanted regions in waveguides. These processes can be used as a post-fabrication trimming method to fix the performance variations caused by fabrication tolerances.

The annealing speed depends on the temperature of the amorphous sections during the annealing process. The continuous wave laser can deposit more thermal energy into the silicon lattice than the pulsed laser in our experiments; therefore, more shift of resonant wavelength can be brought about by the continuous wave laser annealing.

To demonstrate a more flexible annealing process, which could even be utilised after the devices are packaged, integrated thermal heaters were fabricated on top of optical devices. In addition, electrical annealing can also shorten the time spent on the annealing process, which can increase the throughput of a production line. Results show that the thermal power can also be used to perform annealing and to trim the performance of ring/racetrack resonator devices. High trimming accuracy can be realised at low voltage, which provides a slow annealing speed. Rapid annealing is also accomplished by high applied voltage. Therefore, the electrical thermal

annealing can provide more flexible annealing speeds and annealing process based on different requirements of applications, and it is suitable for further integration with electrical circuits.

Chapter 7 Experimental results: MZI tuning

As shown in the introduction in chapter 3 and simulation in chapter 4, the transmission of a MZI is controlled by the phase difference between two arms. In this chapter, this phase difference is changed via the Ge ion implantation process and subsequent annealing techniques. Therefore, the output transmission of a MZI can be tuned to enable any operating point to be chosen. This property can be used in the post-fabrication trimming of MZIs and building programmable photonic circuits.

7.1 Pulsed laser annealing of MZI with real-time monitoring

Unwanted fabrication variations will cause the shift of operating point of optical devices. The pulsed laser annealing and real-time monitoring experiments of implanted ring resonators have been demonstrated in chapter 6. In this chapter, it is reported how similar techniques were applied to trim the operating point of implanted MZIs. The experimental setup is illustrated in Figure 5.3 (page, 23). The design and fabrication process of MZI devices were described in Chapter 4. Figure 7.1 shows a schematic of the laser annealing process for an ion implanted MZI.

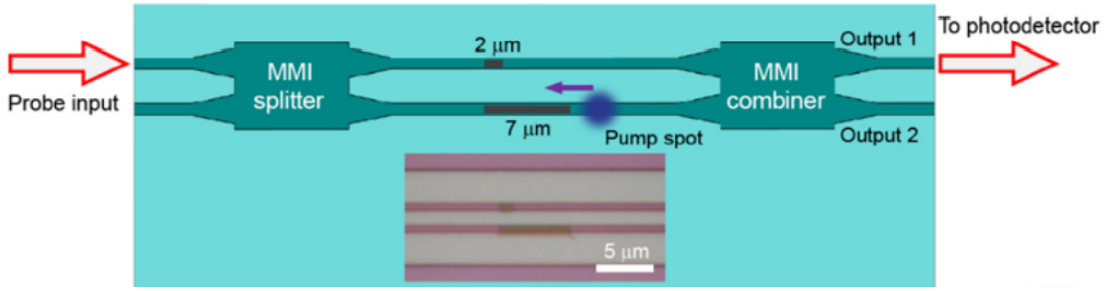

Figure 7.1 - Illustration of pulsed laser annealing with ion implanted MZI [149].

The phase difference between two arms in an implanted, nominally balanced MZI, is defined by the different lengths of the implantation sections in each arm, and any physical arm length difference due to fabrication tolerances. For the device used in this pulsed laser annealing experiment, the length of the longer implantation section is 7µm, while the shorter one is 2µm. During the annealing experiment, the pulsed laser spot was focused onto the longer implanted section. The implanted silicon was recrystallised via the annealing technique, using laser scanning. Therefore, the phase difference between the two arms was changed when the laser spot scanned the amorphous region of the longer implanted region. Due to the small difference of optical path length between the two arms of this particular MZI, the free spectral range is much wider than the telecom probe used for optical characterisation, which is an ultrafast laser pulse at 1550nm

with 20nm bandwidth. The output signal T was collected from output1 and coupled into a photodetector. A lock-in amplifier was used to collect ΔT for high accuracy trimming and analysis.

Figures 7.2 (a) and (b) depict the change of signal T and ΔT respectively, while the 7μm implanted segment was gradually annealed by the pulsed laser. The laser spot was first focused onto the intrinsic silicon beside the implantation region. In figure 7.1, we can define the righthand side of implanted region as the 0μm and define the moving direction of the annealing laser as the positive direction. In figure 7.2 (a), the optical signal T has no change when the laser position changed from -2μm to 0μm. A small increasing trend of T can be observed in this region, which is attributed to the gradually accumulated thermal heating brought by the pulsed laser. After the laser spot step into the amorphous region, the phase difference between two arm starts to be trimmed. The output signal T significantly changed from position 0μm to 6.5μm. The output signal shows a saturate trend after the position 6.5μm. This is because, after the centre of laser spot (with a radius of 500nm) passed the 6.5μm, the overlapping area between the annealing laser spot and the implantation area stared to decrease. The annealing effect become weaker than the previous positions. The trend of figure 7.2 (a) agrees well with the implantation length 7μm. In figure 7.2 (b), the ΔT curve achieves the lowest value at around 3μm. Based on the transfer function of a one input MZI discussed in chapter 3 ,which are equations (3-49) and (3-50), this minimum point corresponds the quadrature point of the MZI transmission with the largest derivative (0.5π). Then we can estimate that the whole phase shift after the first annealing process should be approximately 0.72π. The small discontinuity shown in this curve was caused by the error and disruption of a slip-stick piezo stage.

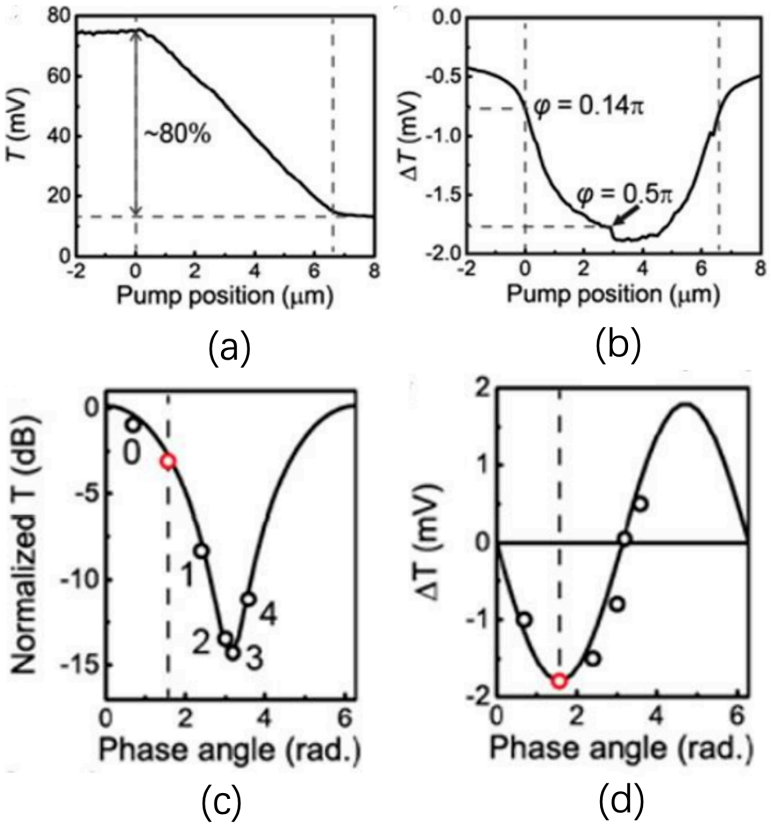

Figure 7.2 - (a) Measured transmission (T) signal shifts as the function of the pump spot position during the scanning along the whole 7 μm implanted section; (b) measured ΔT signal dependent on the pump spot position. Measured values of (c) T and (d) ΔT for four subsequent annealing cycles, labelled 1–4 in (d), with red dot corresponding to a balanced working point as determined from minimum in ΔT of (c) [149].

Three more annealing cycles were repeated to achieve a greater phase shift. The result of T, normalised to input signal, and ΔT, are shown in figures 7.2 (c) and (d) respectively. After four scanning cycles for the 7μm length implanted section, a phase shift of 1.2π was achieved.

7.2 Electrical annealing of MZI

Using the laser annealing technique, we can position the laser spot accurately onto the device and anneal part of the implanted sections, as previously discussed. However, it is relatively time-consuming to focus the laser spot and physically scan through the implanted waveguides one by one. Besides, it is not possible to anneal a packaged device, as the top surface of the silicon chip will not be accessible for the free-path laser. Electrical annealing using integrated micro-heaters can solve these issues.

The structure and fabrication process of the MZIs with TiN micro-heaters are described in chapter 4. For these devices, two different lengths of implanted sections were also fabricated, one in each arm. Top view and cross sectional view schematics of the ion implanted MZI is shown in figure 7.3.

Experimental results: MZI tuning

The dimensions of the implanted MZI used in this electrical annealing experiment is also illustrated.

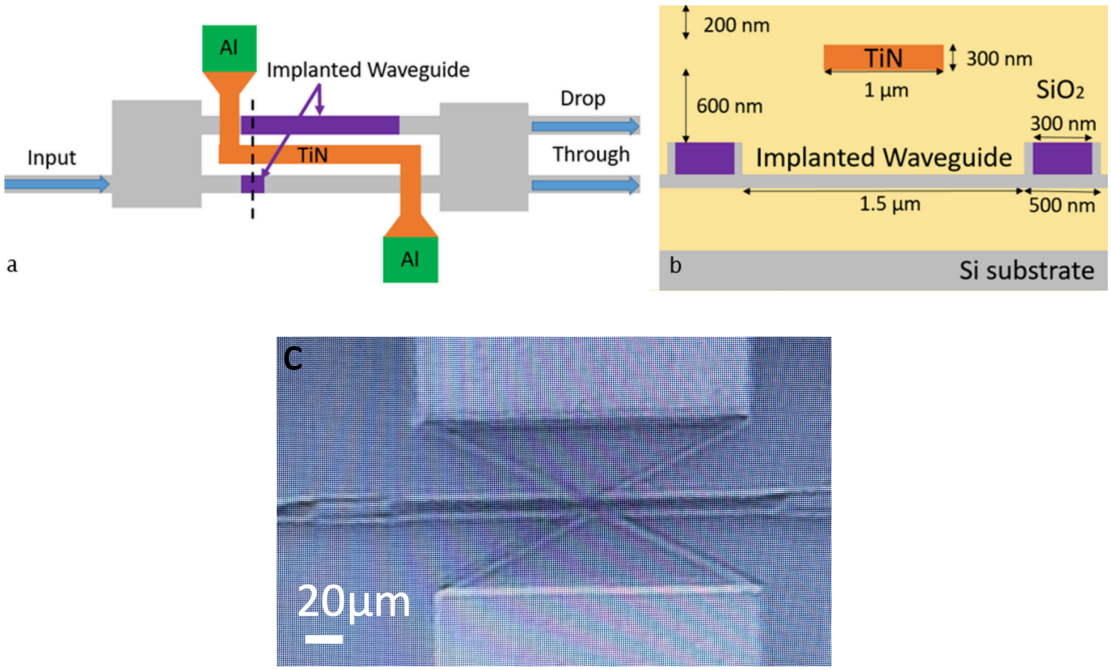

Figure 7.3 - A schematic of ion implanted MZI, (a) top view, (b) cross section view. (c) An optical microscope image of the fabricated implanted MZI with TiN heater [154].

Figure 7.4 shows the measured optical transmission spectrum of the ion implanted MZI before and after electrical annealing. For the unimplanted MZI used for reference, the optical signals would be mainly output at the through port. By introducing the implantation sections in the waveguide arms and the subsequent annealing process, we can then control the phase difference between the two arms, and therefore control the operating point of the MZI. The length of the implanted sections in this device are 16µm in one arm, and 1µm the other arm. Before the annealing, over 90% of the optical signal was coupled into the drop port. For the annealing process, the applied voltage is 7V (the electrical power is approximately 150 mW) and annealing time is approximately 10 seconds. This recipe was chosen after studying the annealing characteristics of similar devices to ensure that full annealing could be achieved at 7v. After the electrical annealing, the transmission of this MZI has been inverted. Over 90% of optical signal was detected at the through port output, which matched the transmission state of the test MZI with no implantation sections. Regarding the results shown in figure 7.4, the change of the MZI transmission corresponds a change of ~π in phase shift. To make sure the annealing is fully complete, this device was annealed for another 10s at 7V. No further change of optical transmission was observed, indicating full annealing. All the implanted section was annealed fully and completed in several seconds, which was much faster than the laser annealing experiment. Thus, electrical annealing method can significantly improve the throughput of annealing process. There is a potential issue with the transmission shift in this experiment. A 3π phase shift (or any

odd multiple of π) will also produce the same result as a π phase shift, and hence result in the same measurement. Therefore, the smallest electrical power should be used for annealing to make the process as efficient as possible, which requires complete characterisation of the annealing process for any given device.

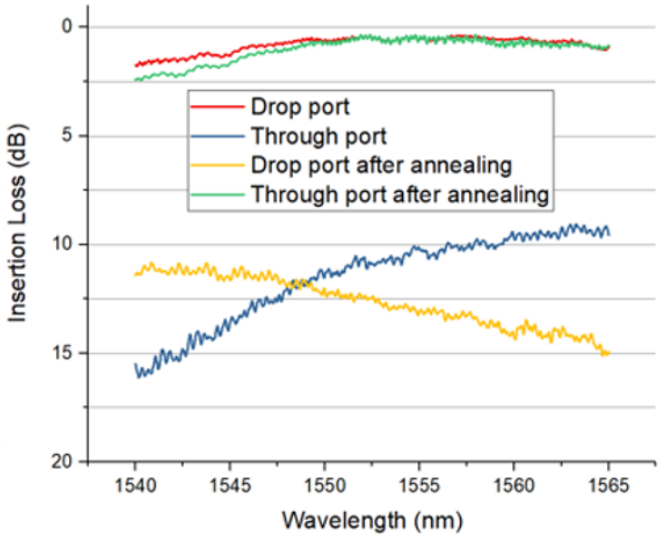

Figure 7.4 - Optical transmission spectrum of ion implanted MZI before and after annealing by 18 µm TiN filament [154].

Based on the discussion in section 2.3.1 on page 36, the working state of the MZI in figure 7.4 is directly shifted from 'cross' to 'bus'. For post-fabrication trimming and programmable photonic circuits applications, selecting other operating points is also important. Figure 7.5 shows smaller transmission shifts when the implanted section was partially annealed at lower electrical power. This MZI was fabricated with an implanted section of 8µm, and the heater filament is 10µm long. The applied voltage started from 0V. Each point shown in this figure represents one annealing cycle, which continues for 20 seconds. After the electrical power is increased to higher than 44.8mW, corresponding to the applied voltage of 1.8V, the implanted region starts to be annealed. Prior to this point, the changes are reversible via the thermo-optic effect. The optical signal at the through port shifts from 85% to 75%. The transmission of the implanted MZI has no change after the first annealing cycle. As the electrical power increases, the phase difference between two arms was gradually decreased, and more optical power was coupled into drop port output. The highest coupling efficiency achieved was over 93%, while the lowest transmission of the through port output can be trimmed to be smaller than 5%. The transmission of through and drop port have greater shift under higher electrical power, which is because the temperature is higher. For example, the transmission shift, as well as phase change, brought by 105mW is much greater than 40mW. When the electrical power reached 160mW, corresponding to an applied voltage of 4V, the amorphous section was fully annealed. Therefore, over 90% of the signal is detected at the through port. The tuning speed of the phase difference, as well as the

transmission of MZI, was much more controllable than the experiment discussed in section 7.2. The phase change after the full annealing of the implanted MZI is 1.5π, corresponding to a longer implanted section of 8μm. Therefore, the phase shift of the implanted MZI in the former annealing experiment is 3π, corresponding to an even longer implanted section of 16μm.

In this experiment, the detail of transmission shift is preliminary shown. However, the jumping between each transmission points seems still too large for trimming and programmable photonic circuits applications. Therefore, the tuning accuracy should be improved, and more data points should be collected during the annealing process.

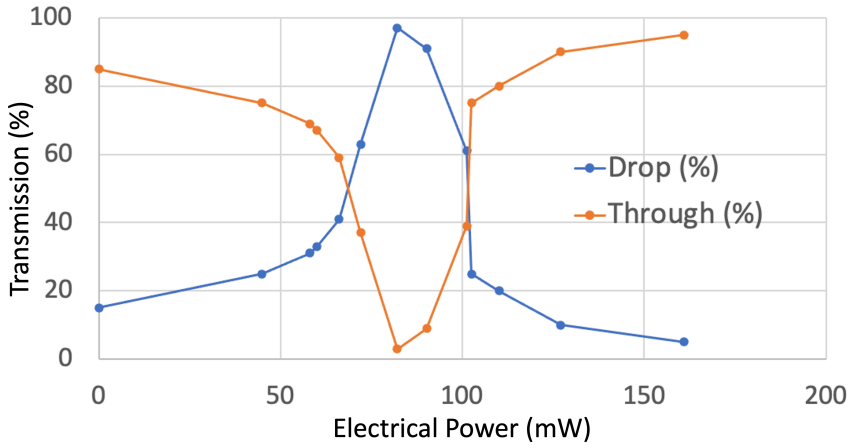

Figure 7.5 - Optical transmission shift of MZI under 0.2V voltage rising step and 20s annealing time.

7.3 High accuracy tuning of MZI

An MZI cannot only work as an optical switch, but also can split the optical signal with a any desired splitting ratio in an optical network. High accuracy tuning is critical for this application. Therefore, the phase difference needs to be controlled accurately between the two arms of the MZI during the annealing process. In the previous experiment, the applied voltage is manually adjusted to 4V. Errors, such as incorrect annealing time and inaccurate voltage, will compromise accuracy, and must be minimised because the operating point of MZIs is very sensitive to the phase difference between two arms, and therefore manual operation of annealing functions is undesirable. In these experiments, the applied voltage and annealing time are controlled by setups described in section 5.3 (page, 84). Python coding was used to command the instruments.

In this experiment, the results of which are shown in figure 7.6, the annealing time for each annealing cycle was as long as 20s. Based on the former RTA experiments mentioned in the work of Milosevic et al., shorter annealing time and lower annealing temperature provided less annealing effect of implanted sections, as expected [104]. Higher precision of MZI working points

can be achieved, which is essential for optical AI network application. To improve the precision of MZI operating point setting, 0.02V was used as the step in applied voltage. The voltage source, an Agilent E3640A, has the response time of approximately 1×10^{-5} s. To minimise the measurement errors, 0.1s was chosen as the ON time of electrical power in the Python code. The optical transmission of the implanted MZI with 8μm implanted length is shown in figure 7.6. The length of filament on this MZI is 10μm long. The initial working state of this MZI is significantly different with the MZI used in figure 7.6. This was caused by the fabrication errors. A similar situation also happened in the work of Dr. Xia Chen [103].

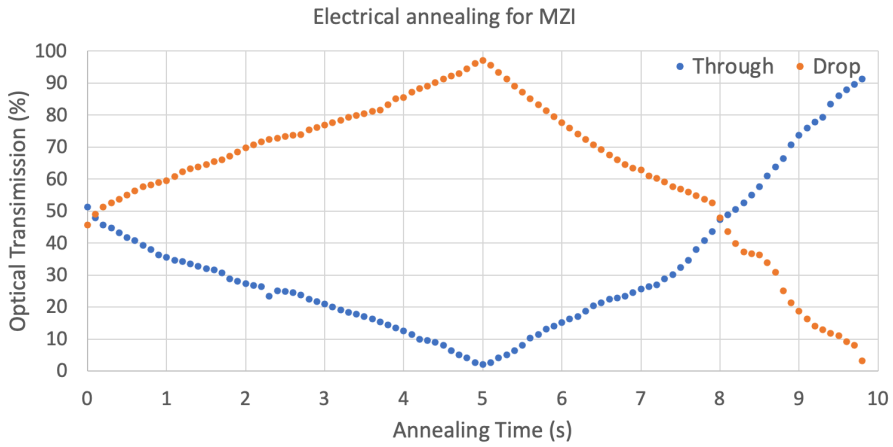

Figure 7.6 - Optical transmission shift of MZI under 0.02V voltage rising step and 0.1s annealing time.

During the whole annealing process, 99 data points were collected, corresponding a phase shift of 1.5π. The tuning accuracy of this experiment is higher than 0.02π, which is approximately 10 times higher than the last experiment (figure 7.5). Due to the fabrication error, the initial transmission of this MZI was significantly different to the MZI used in the last experiment. The annealing effect still started when the electrical power reached 45mW while the applied voltage is 1.8 V. The optical power coupled to drop port output increased as the phase difference became smaller during the annealing process. The highest coupling efficiency of 96.5% of total power was achieved. After this peak, the optical power started to couple back to the through port output. After the electrical power reached approximately 165mW, the optical power detected at the drop port output was ~3% while 92% of input optical power was collected at the through port output. In the last annealing cycle, the applied voltage has reached 3.76V. No change of transmission was observed at higher electrical power and longer annealing time, indicating full annealing had taken place.

The final applied electrical power is greater than the last experiment, even though the applied voltage is smaller. This difference is caused by differences in the filament heaters. In this experiment, the tuned coupling efficiency is even higher than the transmission after fully

annealing. This is because that Ge ion implantation and annealing techniques have the ability to improve the fabrication imperfections in this MZI by selecting the optimum operating point.

7.4 Summary

In this chapter, pulsed laser annealing and integrated electrical thermal annealing experiments of implanted MZIs are introduced and discussed. The phase shift after full annealing by laser annealing is approximately 0.9π, for an implantation length difference of 5μm, corresponding the phase trimming efficiency of approximately 0.18π per 1μm implanted segment. For MZIs with 7μm implantation length difference, the electrical annealing can achieve a greater phase shift of 1.5π, corresponding to a trimming efficiency of approximately 0.21π per 1μm implanted segment. This improved trimming efficiency is brought by the more entire electrical annealing to the implantation arear. The whole operational process of electrical annealing is also much simpler than laser annealing. By controlling the instruments through software, the electrical thermal heater can also achieve a high phase tuning resolution of 0.02π for the implanted MZI.

Chapter 8 Experiment results: Erasable directional couplers

Directional Couplers (DCs) are one of the most basic passive devices in photonic circuits. They can realise the power redistribution of signals [155]. Their structure also realises the function of phase shifting, which can be used to build configurable programmable photonic circuits [109]. Compared with MZI and ring resonators, DCs typically have smaller dimensions that can bring advantages in terms of footprint for large-scale integrated circuits. Furthermore, the operation of a directional coupler also has lower sensitivity to ambient temperature changes [156]. The fabrication and design of implanted one and two-stage directional couplers has been introduced in the chapter 4. The distribution of optical power at the output ports is related to the coupling length in the DCs. The coupling length in an implanted DC is depends on the length of an implanted waveguide. It has been demonstrated that the lattice disorder can be fully or partially repaired via an annealing process. Therefore, the length of an implanted waveguide in a DC could also be changed by the same methods. In this chapter, the annealing experiments for implanted one and two-stage directional couplers will be presented, including CW laser annealing and integrated electrical annealing.

8.1 Continuous wave laser annealing of erasable directional couplers

In the two-stage implanted directional couplers, the waveguide between the through port and drop port is created by ion implantation in the silicon slab layer, as shown schematically in Fig. 8.1. The width of the implanted waveguided and conventional waveguide are 560nm and 500nm respectively. The gap between the implanted region and conventional waveguide is designed as 230nm. The length of the implanted waveguide is 20μm. The optical signal can couple from the bottom waveguide to the implanted waveguide in the middle and then subsequently couple to the top waveguide. The amorphous waveguide formed by Ge ion implantation can be erased by the annealing process. In this section, the devices were annealed by a continuous wave laser, which was described in detail in chapter 5. The scanning route of the laser spot is shown in figure 8.1. Based on the former discussion of this structure in chapter 4, the final distribution of optical power at output ports highly depends on the length of the implanted waveguide. As the implanted waveguide is gradually annealed by the laser beam, the transmission of optical signal coupled from bottom waveguide to the top waveguide can consequently also be tuned.

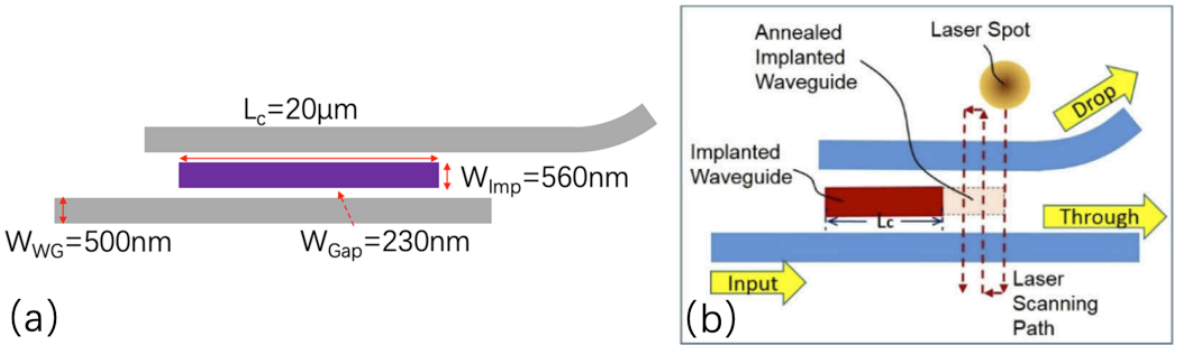

Figure 8.1 - (a) Top view of implanted two-stage DC. (b) Illustration of laser annealing process for two-stage DCs [73].

Figure 8.2 gives the measured transmissions of a two-stage erasable DC during the whole annealing process. Before the annealing the length of the implanted waveguide was 20μm. With the reduction of implanted waveguide, the coupling efficiency increases. The highest coupling experimental efficiency of over 90% is achieved when the coupling length, Lc, is around the 11μm, or12μm. However, it is notable that, for some points, the sum of the optical transmission at the two output ports is less than 100%. This is caused primarily by the scattering of optical power left at the end of the implanted waveguide, when the optical power cannot be fully coupled into top waveguide or drop back to bottom waveguide. After the whole implantation region is annealed by the laser, the input optical signal will remain in the bottom waveguide.

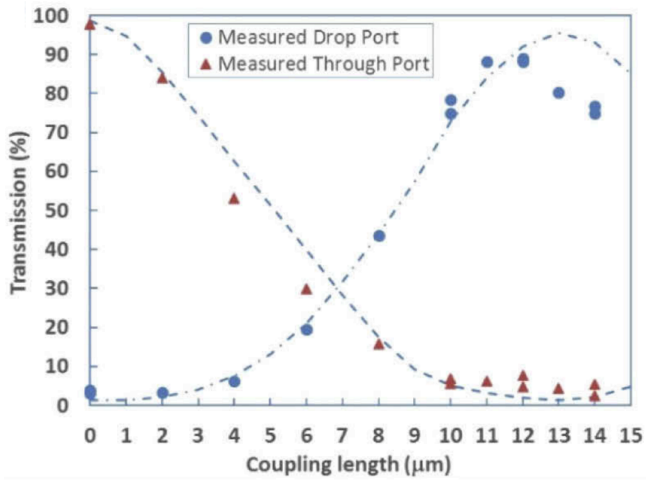

Figure 8.2 - Measured optical transmission of two-stage implanted directional couplers [73].

For photonic artificial intelligence and neural network applications, the basic tuneable units are required to work at the pass or cross state, as discussed in section 2.3.1 (page, 36). However, the scattering loss will lead to a maximum 2.2dB loss when the transmission of the through port and drop port in DC are equal. Based on the simulation results in chapter 4 (page, 70), the single-stage DC has less such scattering loss. Figure 8.3 shows the top-view and transmission of implanted single-stage DCs with different coupling lengths. The width of the implanted waveguide is 540nm. The gap between the implanted waveguide and conventional waveguide is 200nm. The straight

part of the implanted waveguide is defined as the coupling length, L_c. Single-stage DCs have the different shape of transmission curve. In comparison to the transmission curve of the two-stage DC (figure 8.2), the sum of the optical signals from two output ports are approximately 100%. The light scattering loss is very low during the coupling process. This is due to the end of the implanted waveguide of single-stage DC being connected with a conventional waveguide. The coupled optical signal in the implanted waveguide will still propagate into the drop port output. Therefore, for a 3dB coupler application, a single-stage DC is more suitable than a two-stage DC. For wafer scale-testing applications, implanted directional couplers can be used as erasable optical inputs/outputs in the integrated photonic circuits. The highest coupling efficiency of a single-stage DC, shown in figure 8.3 (b), is only over 80%, while the two-stage DC can achieve a coupling efficiency higher than 90%. The reflection loss between the implanted waveguide and conventional rib waveguide is one of the reasons resulting in lower coupling efficiency. Another reason is the transmission loss in the implantation waveguide. The length of the implanted waveguide between the end of coupling region and conventional rib waveguide is even twice longer than the L_c.

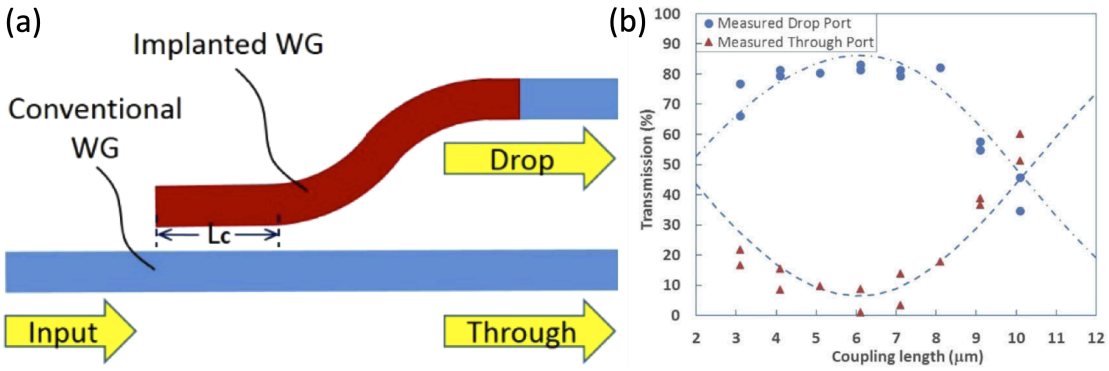

Figure 8.3 – (a) Top-view of a single-stage DC. (b) Measured transmission of implanted single-stage DC during the CW laser annealing process [73].

The highest coupling efficiency has been improved to over 90% by minimising bending and propagation loss and in this single-stage implanted DC, which is shown in figure 8.4. The highest coupling efficiency is achieved at L_c=5um. In this device, the implanted bent waveguide is replaced by the conventional rib waveguide. The highest coupling efficiency is improved because the bending in this device is gentler than the bending in the former experiments, and propagation in the implanted region is minimised. The bending loss of conventional waveguide is also lower than the implanted waveguide with same dimension.

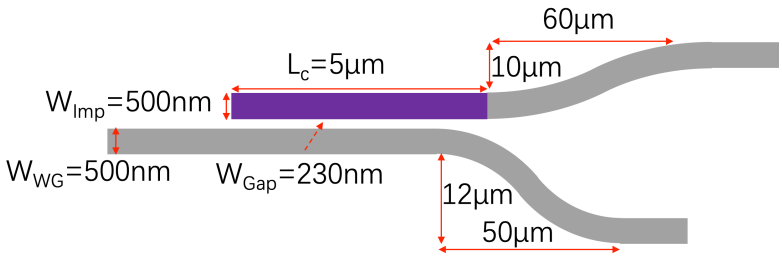

Figure 8.4 - Schematic of single-stage implanted DC with optimized bending region.

8.2 Electrical annealing of erasable directional couplers

As mentioned previously in section 7.2, the electrical integrated heater can achieve the annealing process even after the devices are packaged and the annealing process can be done with a much higher speed than using lasers. In this section, a TiN heater is fabricated on top of the two-stage implanted DCs. The on-chip electrical annealing process is much easier to implement than laser annealing because it has no preparation work such as alignment and scanning. The design of the device used in this experiment is shown in figure 8.5. The width of the conventional rib waveguides and implanted waveguide in a 150nm thick slab layer is 500nm. The gap between the conventional waveguide and implanted waveguide is 230nm. The 200nm cladding layer on top is used to protect the heater filament from air at high temperature, while the 600nm middle oxide layer is to avoid optical signal absorption by the heater on top. The width and thickness of the TiN filament are 1µm and 300nm respectively. The length of the heater filament is designed to be 2µm longer than the implantation waveguide to give a full thermal coverage of the implanted region. The length of the implantation waveguide is 17µm while the length of filament is 19µm. Figure 8.6 gives the transmission of implanted two-stage DC before and after annealing.

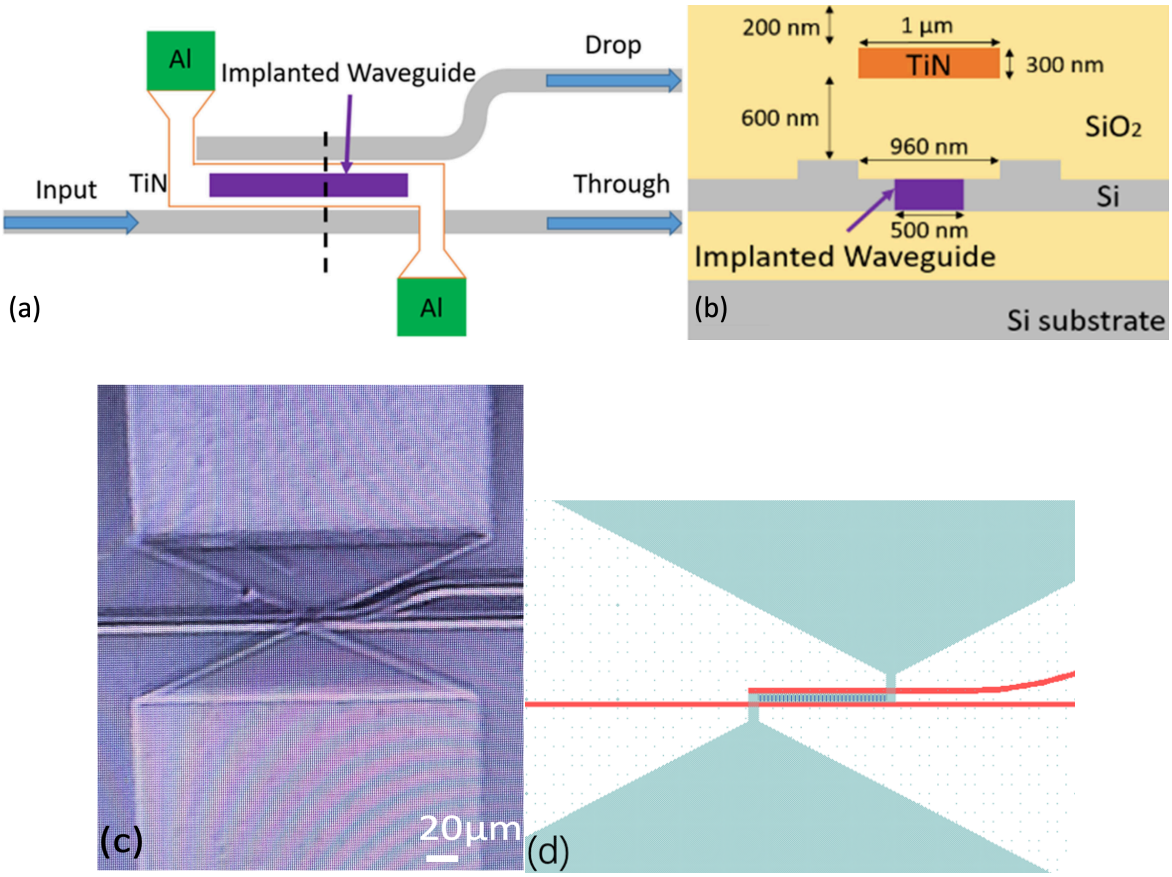

Figure 8.5 - Top view (a) and cross section (b) of ion implanted two-stage directional couplers with TiN heater. (c) An optical microscope image of the fabricated implanted two-stage DC with TiN heater. (d) Mask layout of an implanted two-stage DC with TiN heater [154].

Before annealing, approximately 65% of the optical power is coupled into the drop port and 35% of the optical power is detected at the through port. A preliminary annealing test was carried out to check the overall performance of this device. The annealing process was manually controlled at first. The applied voltage was manually increased from 0V to 8.7V gradually in 30s. During the first 25s, the applied voltage was manually increased to 8V. As the applied voltage raised to 8.7V and was kept at 8.7V for another 5s, the heater failed. Under the applied voltage of 8V, the electrical power is approximately 150mW. After this annealing process, the optical signal output at the drop port was only about 1.5% while the optical power output detected at through port was more than 95%. This change of transmission is because the implanted waveguide was erased by the thermal heater. Based on the former results of laser annealing, in section 8.1, the implanted waveguide in the two-stage DC is fully annealed in this case.

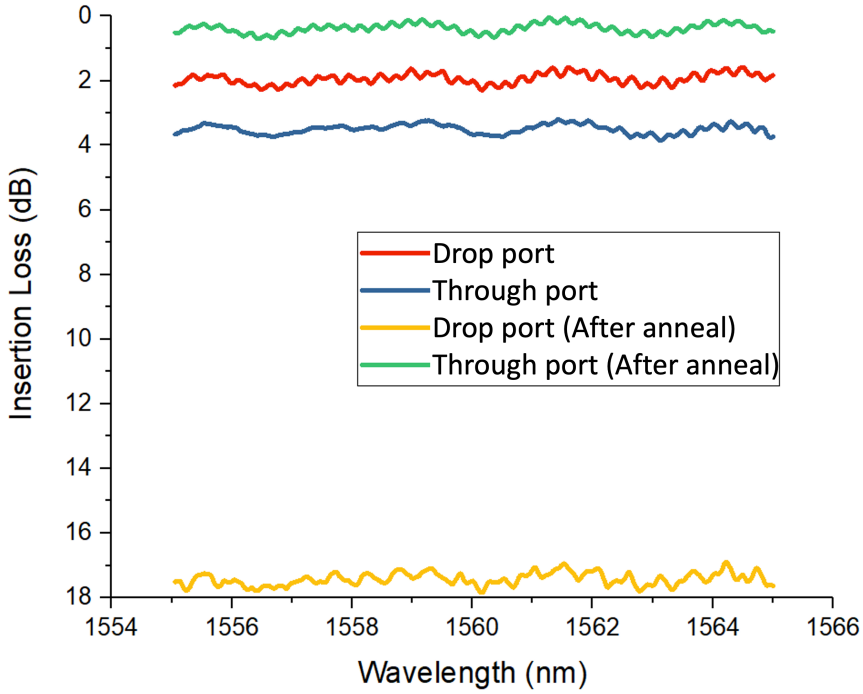

Figure 8.6 - Optical transmission of DC before and after annealing by 19 μm TiN filament [154].

Figure 8.7 gives the dynamic curves of this annealing process for another implanted two-stage DC with 15μm implantation waveguide and 17μm filament. The black curve in figure 8.7 illustrates the dynamic shifting process of transmission at the drop output when the applied voltage gradually rises from 0V to 7V in 120s. The raising step is 1V and the duration time for each point is 20s. The change in applied voltage is shown as the red curve in figure 8.7. After an applied voltage from 0V to 6V, the optical transmission will return to its original value after the applied voltage is removed i.e. the change is reversible. Therefore, the change of transmission shown in the curve is caused by the thermo-optical effect. The refractive index, as well as coupling efficiency, can be temporary be controlled by applied electrical power. This principle is now widely used in building reversible programmable photonic circuits. Once the applied voltage reaches 7V, the output signal at the drop port suddenly drops to around 2% in 3s. The electrical power at 7V applied voltage is 145mW. The temperature distribution at this state is shown in figure 8.8. The temperature at the centre of the implanted waveguide is around 700°C, which is higher than the temperature used in RTA of ring resonators, and consequently suggests that the annealing temperature has been reached.

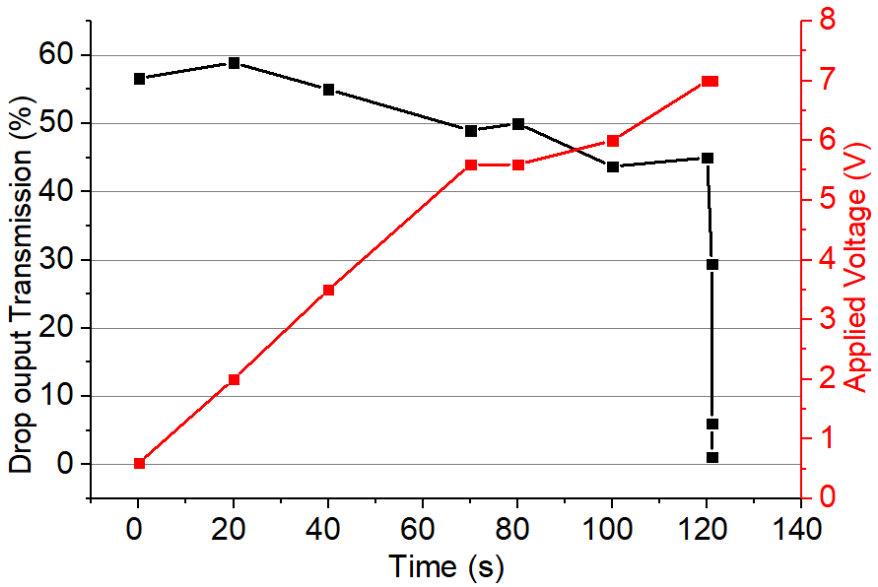

Figure 8.7 - Measured dynamic results of annealing process for an implanted two-stage DC with 17µm filament [154].

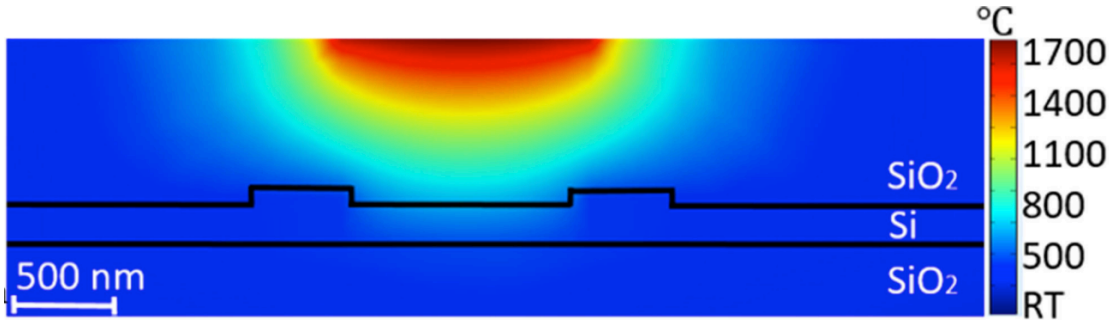

Figure 8.8 - Temperature distribution of implanted two-stage DC under 7V applied voltage [154].

After full annealing of the implanted waveguide, almost all the optical signal remained in the bottom waveguide, which means that this device is completely erased from the main circuit. This function can be used as erasable switch/optical signal input and output in wafer-scale testing of photonic integrated circuits.

In the pulsed laser annealing experiments of implanted MZI presented in section 7.1 (page, 99), the implanted sections in the waveguide were fully erased after four annealing cycles. Therefore, partial annealing state of device can be potentially achieved if the applied voltage was controlled in smaller steps.

Figure 8.9 shows the measured transmission of the implanted two-stage DC with 14µm implantation waveguide and 16µm filament, when the applied voltage for annealing is slowly increased. Similarly to the colour scheme of figure 8.7, the black line presents the dynamic transmission measurements and the applied voltage is shown as the red line, as it rises from 0V to 7V in 265s. There are three phases of evolution of the transmission data of this whole graph. During the first phase, the applied voltage on the heater rises from 0V to 6.3V in 175s. The optical

signal at the drop port shows a steady decrease from 35% to approximately 20%. However, the transmission of optical signal will return to 35%, once the applied electrical power is removed. Therefore, the shift of transmission of the directional coupler in this phase is caused by thermal-optical effect and is reversible. As the voltage was increased to 6.5V, the change of transmission become irreversible, because the temperature of the implanted waveguide has reached the annealing temperature under such applied voltage. The lattice disorder in the implanted waveguide has started to be annealed by the applied electrical power. The annealing speed and phase shift in this state is much slower and more controllable than the previous experiments with a larger voltage step. After the reversible phase comes a partial annealing phase, as voltage is increased further. If the applied voltage is removed during this phase, partial annealing of the implanted DC is achieved. Figure 8.10 shows the temperature profile of the cross section. Unlike with the simulated temperature for the full annealing experiment, the temperature of implanted section in this experiment is much lower (around 500°C). The electrical thermal power is approximately 130mW under the applied voltage of 6.5V for example (fig 8.10).

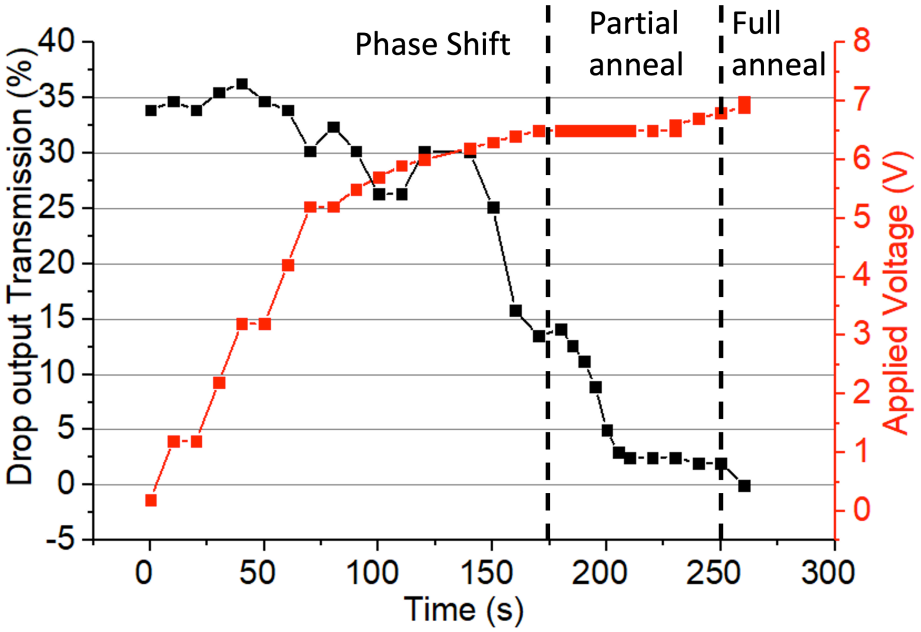

Figure 8.9 - Experimental results showing dynamics of the annealing process for a directional coupler with 16µm TiN filament [154].

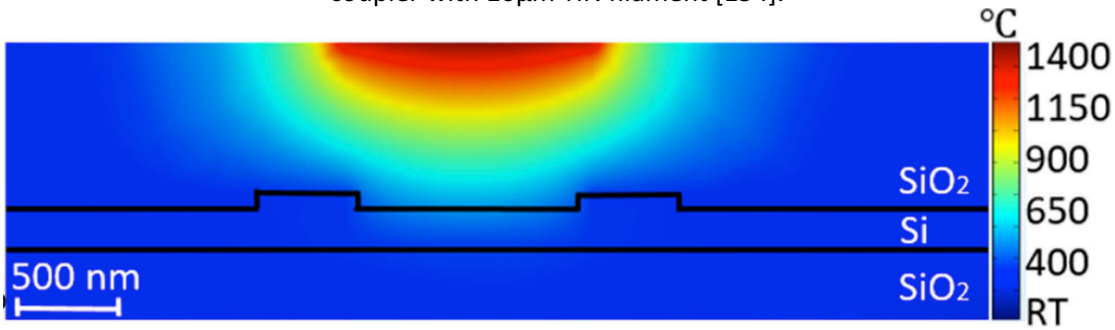

Figure 8.10 - Simulation result showing a temperature distribution of implanted two-stage DC under 6.5V applied voltage [154].

The third phase is the full annealing of the implanted two-stage DC. After the applied voltage reaches 7V, the optical signal coupled to the drop port is around 1%. Most of the optical signal is still in the through port waveguide. The difference in optical transmission between the crystalline silicon and fully annealed amorphous silicon, is negligible. Therefore, we can conclude that the lattice damage induced by the ion implantation process have been repaired by integrated electrical annealing.

Due to the non-uniformity in the fabrication process and variation of device dimensions, the performance of the heater filament can also be different even if the dimensions and applied voltage are the same. A range of implanted two-stage DCs with different TiN filament lengths were tested to demonstrate full annealing. This experiment data is plotted in figure 8.11, together with the simulated voltages that satisfy the annealing temperature for implantation waveguide. The central solid blue line is the fitted curve for the simulation data, while the red points represent the measured experimental data. The simulated data in the solid blue line shows a non-ideal linear trend, which is caused by the error of reading voltage in the simulator. The two blue dotted lines are the fitted curves for simulation data under the worst variation of fabrication processes across the wafer, such as the thickness of middle oxides layer and width of the filament. This variation is normally caused by the misalignment of different layers in a lithography process and fabrication errors in the lift-off process. The resistance of each filament can be significantly affected. To achieve the same electrical power, lower applied voltage is required for the filament with smaller resistance. For example, for 17µm filaments, shown as two red dots in figure 8.11, 7.2V is needed for a filament to achieve annealing temperature in one experiment and only 6.9V is needed for another narrower filament to achieve the same annealing effect. These two dotted blue lines give the maximum expected deviation of experimental data. The experimental data all falls within this region and agrees well with the trend of simulation data.

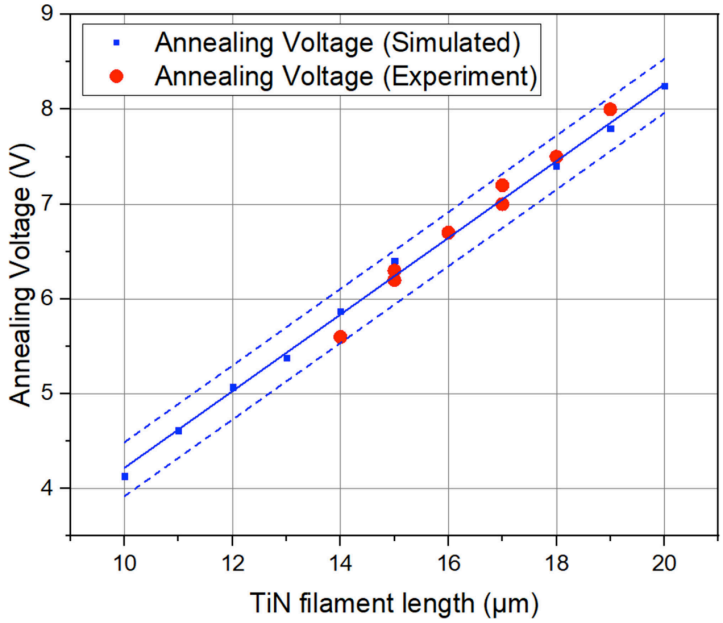

Figure 8.11 - Experimental and simulation voltage supplied on the filament achieving fully annealing [154].

8.3 High accuracy tuning of erasable DC

In the last partial annealing experiment for the implanted DC in section 8.2, the electrical integrated thermal heater shows its potential for a high accuracy tuning of power distribution at the output ports. In the experiment introduced in this section, the applied voltage increased in 0.1V steps for each annealing cycle with an annealing time of 0.2s. The transmission change of the implanted DC during the whole annealing process is illustrated in figure 8.12. The first point in this graph shows the initial transmission of the device with no annealing. The second data point was collected as the applied voltage reached 4V when the electrical power is approximately 44mW. This is the applied power level where the refractive index of the implanted waveguide had been changed permanently. As the electrical power increased to 130mW, the optical signals detected at two output ports are the same, at 30% of input optical power. The rest of the optical power is scattered at the end of implanted waveguide. Whilst the power level is lower than ideal, it does demonstrate that two output waveguides can be provided with equal power. After the electrical power reaches the 220mW, this device reaches the fully annealed state. The optical power left in the drop port is only 2%. The measured transmission curve agrees with the curve obtained by laser annealing.

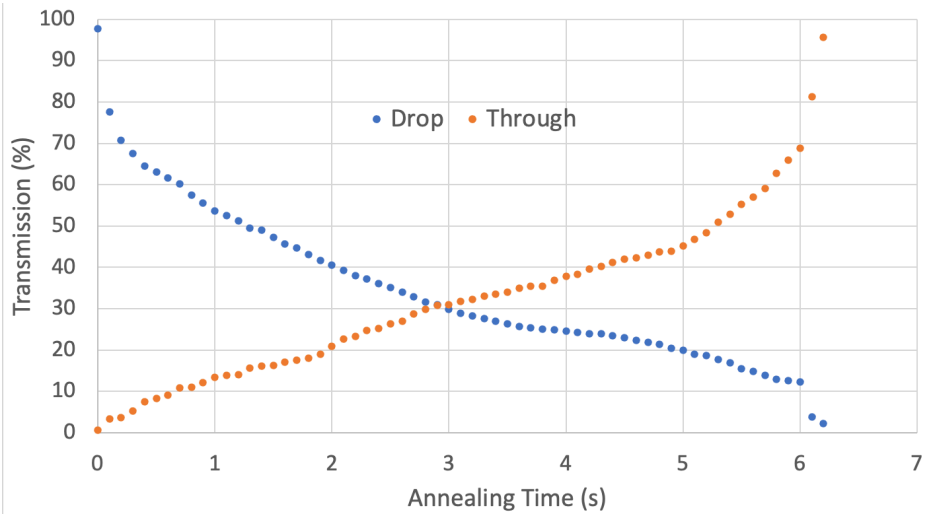

Figure 8.12 - Measured optical transmission of implanted two-stage DC under high accuracy control of applied electrical power.

8.4 Summary

This chapter introduced the annealing experiments of implanted DCs using lasers and integrated electrical heaters. Similar to the implanted MZIs and ring resonators, the implanted section in the devices can be erased after the full annealing process. However, for implanted DCs, the implanted sections of these devices are permanently removed from the integrated photonic circuit. Compared with laser annealing, the annealing process with integrated heaters is easier and better for industrial production, because the operation processes of laser annealing, such as alignment and scanning, are more difficult and time-consuming than electrical annealing. Therefore, erasable DCs can work as the optical input/output port for optical wafer-scale testing, and can be subsequently erased. The highest coupling efficiency is over 90%. By partial annealing a two-stage DC, the coupled signal can also be tuned from 0% to approximately 95%.

Chapter 9 Conclusions and future work

9.1 Summary and conclusions

This project started from the Ge ion implantation into silicon waveguides. Lattice damage and lattice disorder are induced, resulting in a rise of refractive index (~0.4) of the silicon due to amorphisation. Compared with other implantation elements, like silicon, Ge is from group IV. Therefore it is not a dopant and the concentration of free carrier in silicon will not be changed after the implantation. Consequently, no additional free carrier absorption loss will be induced in optical devices, although amorphisation does increase the loss for other reasons. In addition, Ge is a CMOS compatible element, which cater to CMOS production foundries.

In this project, the implanted region in the silicon waveguide can be erased or partially annealed via the annealing process, including laser annealing and integrated electrical heater annealing. The principle of the annealing process is recrystallization and removal of the induced lattice defects and disorder via thermally assisted diffusion. After the annealing, the refractive index of annealed silicon can be close to crystalline silicon. In the laser annealing method, the laser spot locally focuses on the implanted area in one optical device, leaving no alteration on other nearby devices. However, this annealing method is not suitable for mass production. Focusing the laser spot on a chip is a time-consuming process, which increases the time-cost of the production. The time used for annealing only one device using laser annealing is around several minutes. Furthermore, laser annealing cannot be used after the devices are packaged. In the final testing for the integrated products, the annealing process may be required even after packaging, particularly for programmable photonic circuits. For solving these two issues, we explore and demonstrate on-chip electrical annealing. There is no preparation process before annealing, which is convenient for operators in the production line, or in post production. The annealing process can be realised by applying an electrical signal onto the in-built thermal heater. Even after the photonic circuits are packaged, the annealing can still be used. After the electrical connections are made with the contact pads, the annealing process of one device can be finished in seconds, and could also be automated in principle. The throughput can also be greatly improved by using integrated electrical annealing, because annealing can be carried out in parallel or automated. In this project, Ge ion implantation and annealing techniques have been used in wafer-scale testing, post-fabrication trimming and building programmable photonic circuits.

In the industrial production of silicon photonic integrated circuits, yield of photonics chips has always been one of the key indices to affect the cost. A reliable and suitable testing method plays a significant role in the optical industrial production. Compared with the traditional testing

methods for photonic circuits, the erasable testing ports mentioned in this thesis can provide a more flexible and reliable testing method for large-scale photonic circuits with a high integration level.

Erasable directional couplers and tuneable MZIs are successfully demonstrated to couple optical signals for testing applications. These devices can act as the optical inputs and outputs in photonic integrated circuits. Erasable DCs have smaller dimensions than MZIs, which could result in a smaller footprint for each testing port. The device design, fabrication, characterisation and electrical annealing experiments have been performed. Due to the change in refractive index of implanted silicon waveguides via annealing, the optical transmission of optical devices can be changed after the implantation process. In a two-stage directional coupler, the length of the implanted waveguide deeply affects the coupling efficiency because it defines the coupling length. Simulated and experimental results both illustrate that the optical transmission is shifted as a function of the length of implanted waveguide, a well-known phenomenon in directional couplers. As the implanted waveguide length increases from 0μm to 11μm, the optical signal coupled to the drop port shows an increasing trend. The highest transmission signal at the drop port is approximately 90% of the input, which is achieved by a 12μm long implanted waveguide. With the continuous lengthening of the implanted waveguide, the optical signal in the drop port waveguide will be gradually be coupled back to the through port waveguide. Therefore, the transmission of a two-stage implanted DC shows a periodic change with the length of implanted waveguide, as in conventional directional couplers.

Based on this property, this device can be applied in optical switching. The Ge ion implantation and annealing of an optical device are not reconfigurable processes. To achieve more cycles of the transmission, the implanted waveguide needs to be longer. However, in contrast to the reconfigurable phase shifters based on the thermo-optic effect, a longer implanted waveguide induces greater optical propagation loss. The average loss for 560nm wide implanted waveguides is around 33.5dB/mm. Therefore the implanted waveguide cannot be too long, or unacceptable loss is induced. For a two-stage DC with a 50μm long implanted waveguide, the additional optical loss caused by the implanted waveguide is around 1.68dB per device. In a large photonic integrated circuit, the optical loss will be hard to ignore. Therefore, the erasable DC is more suitable to act as a one-time testing port in photonic integrated circuit. This is similar with the function of a non-volatile testing port in electrical integrated circuits. After testing or debugging of a sub-sectional circuit, this testing port can be permanently erased. These testing ports also allow comprehensive testing of optical circuits even during the fabrication process. Problems will be identified before the wafers are processed to the next fabrication or packaging steps. After the test, these testing points can be removed from the main optical circuits via the annealing process

and leave a negligible influence on the final functions and insertion loss. It will help to increase the final yield of products made from silicon photonics and save cost in the industrial production. Compared with the test points invested by, for example, phase change materials, the Ge-ion implantation technique is much more CMOS compatible.

During the annealing process, the implanted region can be gradually removed. Therefore, the optical performance of implanted devices also changed. With full removal of the implanted waveguide in implanted DCs, the wafer-scale testing port is erased from integrated photonic circuits. An implanted waveguide with 21μm length was created in a two-stage directional coupler to couple approximately 90% of the optical signal. After full annealing of the implanted region, about 5% of the optical signal was remaining in the drop port. However, for the two-stage directional coupler with 14μm implanted waveguide, negligible optical power is left in the drop port waveguide. For the implanted devices used in the future wafer-scale testing, there is no need to launch all the optical power out for testing. If a shorter implantation waveguide is fabricated, less optical power loss could be achieved after the testing process. Around 10% of the optical signal is typically enough for one testing port, corresponding a residual insertional loss of 0.1dB.

We also designed and fabricated implanted MZIs and ring resonators. within contrast to implanted DCs, the implanted section in MZIs and ring resonators is created in the conventional waveguide itself. Different lengths of implanted regions were induced into two arms of MZIs, resulting in a phase difference between the arms. The transmission of the MZI can then be changed by selective annealing. The measurement results show that approximately a 5μm length change of an implanted region can bring a whole π phase shift of transmission. For ring resonators, an implanted section in the ring waveguide changes the effective index of propagating mode in the same way, providing a red shift of resonant wavelength. In different devices, we also investigated the implantation of the coupling region between waveguides of racetrack resonators. During the annealing process of the implanted sections in MZIs and ring resonators, their transmissions will be also changed. Therefore, the implantation and annealing techniques can be applied to achieve post-fabrication trimming, and hence compensate for fabrication tolerance-based performance errors.

Due to the non-uniformity of fabrication processes across the whole wafer, the performance of some optical devices can vary significantly, even they are designed to be identical. A post-fabrication trimming method for optical components is essential to guarantee the fine operation of all components and hence the entire photonic circuit, particularly if devices are utilised that are particularly susceptible to fabrication errors. The cost pf otherwise failed circuits can therefore also be salvaged. The Ge-ion implantation and annealing techniques are demonstrated to realise

post-fabrication trimming for ring resonators and MZIs. Based on the experimental results, the operating point of MZIs and the spectrum of ring resonators can be trimmed via this method. The trimming range highly depends on the length of the implantation regions in the waveguides. Larger implantation area means more lattice damage in the waveguides, which can bring a greater phase shift, but also a greater loss, so devices must be carefully designed. In our experiments, implanted ring resonators achieved over one FSR trimming range and the implanted MZI can achieve over a π shift. A 2π trimming range can be achieved for MZIs via inducing longer implantation sections. This trimming range is sufficient to confront the variations brought about by fabrication variations. The comparison of different post-fabrication trimming methods is shown in table 9.1. The effective index change represents the trimming efficiency. Ion implantation into the conventional silicon waveguides can provide an effective index change of 0.19, which is an order of magnitude greater than other methods. Throughput is also an essential factor for production. One 12-inch wafer contains thousands of optical devices. The trimming process mentioned in this work only take less than 10 seconds after the electrical power is applied and could be automated. High throughput means this trimming method has an advantage for mass production. Finally, all the processes used in this work are CMOS compatible. These advantages make the post-fabrication trimming method in this thesis more suitable for current photonic industrial production than other methods.

Table 9.1 - Comparison of different trimming methods for ring resonators.

	Ref [66, 67]	Ref [68]	Ref [114, 116]	This work
Methods	E-beam	UV light	Sb_2Se_3	Ion implantation and annealing
CMOS compatibility of materials	Yes	No	No	Yes
Throughput (minutes/device)	Low (>17)	Low (>17)	High (<1)	High (<1)
Effective index change	0.06	<0.1	0.071	0.19

Higher trimming accuracy can also be achieved via integrated electrical annealing. By controlling the annealing time and applied electrical power, the annealing speed can be slowed down when the resonant wavelength and optical transmission come close to the target. The trimming accuracy for the resonant wavelength of a racetrack is around 0.1nm, corresponding an optical

phase accuracy smaller than 0.01π. The tuning resolution for optical transmission of MZIs and DCs is around 0.02π.

In addition to the post-fabrication trimming, an ion implanted optical device and integrated thermal heater can also be used to fabricate the basic building blocks for the one-time switchable optical circuits and non-volatile programmable photonic networks. The two-stage implanted DCs can couple over 90% of the optical signal from through port to drop port after the ion implantation process. The optical transmission of these implanted devices can be reversed via annealing. The residual loss is less than 0.2dB. These behaviours correspond to the bar state and cross state of 2×2 couplers mentioned in chapter 2. For implanted MZIs and single-stage DCs, they can also work as a 'partial state'. The long-term operation of these devices needs no continuous electrical power supply as the changes are non-volatile. Table 9.2 gives the comparison of different methods for the 2×2 couplers, which can be used to build a programmable photonic network. Ge ion implantation and annealing techniques are promising for building the programmable photonic circuits, especially for commercial applications. Firstly, compared with the phase shifters and couplers based on the thermo-optic effect, the solution proposed in this thesis has no continuous power consumption and thermal crosstalk issues. Therefore, several milliwatts of electrical power can be saved from each heater. Secondly, compared with the circuits built with Sb_2Se_3, the fabrication processes are all CMOS compatible. No other uncertain factors will be induced to affect the production yield. Thirdly, after the photonic circuits are packaged in an integrated product, the pulsed laser irradiation used to modify Sb2Se3 devices, is no longer possible. The tuneable couplers built with Ge ion implantation can still be programmed on-site via an electrical signal. This is also much more convenient for the self-customisation of optical circuits for different applications. Finally, the shorter optical path is better to achieve a large FSR-filtering function. The footprint of the coupling region of an implanted DC proposed in this thesis is only 20×3μm^2. This is also an advantage for the photonic circuits with high integration levels.

Table 9.2 - Comparison of different methods for the 2×2 couplers in programmable photonic circuits.

	Ref [157]	Ref [158]	Ref [114]	This work
Method	Therma-optic effect	MEMS	PCM	Ge Ion implantation and annealing
Power consumption	Yes	No	No	No
Programming method	Electrical signal	Electrical signal	Pulsed laser	Electrical signal
CMOS Compatibility	Yes	Yes	No	Yes
Optical loss/coupler (dB)	0.23	0.2	0.5	0.2~0.5
Footprint (Length × Width μm2)	61.6×10	40×30	33×6	20×3

9.2 Future Work

The future development of this project should start with increasing the tuning accuracy of implanted devices. Based on the measured results of implanted MZIs, over 100 effective data points are collected during a 1.5π tuning range. The resolution of the tuning process can be further increased by using a voltage source with high response to the electrical signals from computers. This can provide a shorter ON time of the applied electrical power.

High trimming accuracy is the basis of a reliable post-fabrication trimming method. The transmission of an optical device should be as close to the target as possible after the trimming. Based on the experimental results in chapter 6, lower applied voltage can also provide a smaller movement of resonant wavelength. However, the annealing time could be several minutes for each device. This is not an ideal solution for mass production. In a practical trimming process, a narrower pulse-width of an electrical signal can provide shorter heating time for the implanted region. A single pulse could be as short as millisecond to a microsecond. The whole annealing process for a single device could ideally be finished in seconds. Therefore, using a narrower electrical signal and relatively high voltage can guarantee high throughput and high trimming accuracy.

Utilising programmable PICs for artificial intelligence and machine learning is one of the most popular emerging applications of silicon photonics. These applications require high tuning accuracy of each optical device. Consider an optical neural network in deep learning application as an example; the transmission of each basic tuning unit will represent the learning results from software. Accurately tuning the transmission of the optical neural network heavily affects the final learning outcomes. The measurement results from Yichen Shen et al. in 2017 shows that an error rate of 0.005% for each port corresponds to the correct identification ratio of 90% [159]. Therefore, in order to achieve a learning accuracy higher than 90%, over 20,000 data points should be collected in a 2π phase shift for each phase shifter. Based on the experimental result in chapters 7 and 8, the 'ON-time' for the heater filament should therefore be less than 0.6 milliseconds.

In addition to the tuning accuracy, the calibration of transmission after the removal of electrical power is needed for the tuneable devices in this project. Based on the experiment results from chapter 6, a blue shift has been observed after the cooling down of annealed devices. For obtaining a higher accuracy, this shift should be always considered into any trimming or tuning processes, and removed as a systematic error. This would be straightforward for a computerised system.

Appendix A Mask Design

The mask designs presented in this following were used for the fabrication of silicon optical devices.

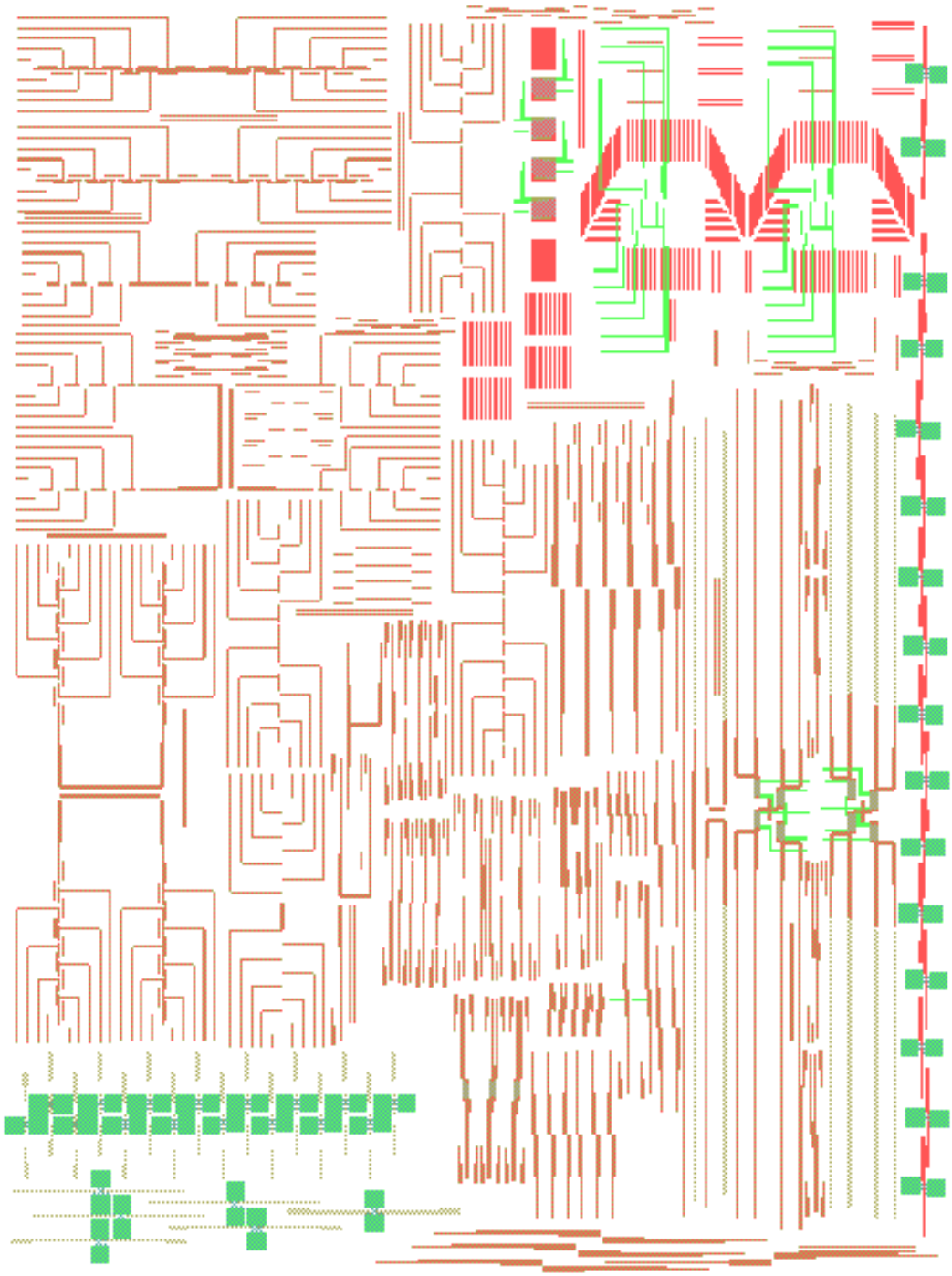

Figure A.9.1 – Mask design for implanted DCs, implanted racetrack and Implanted MZIs used for low accuracy electrical annealing.

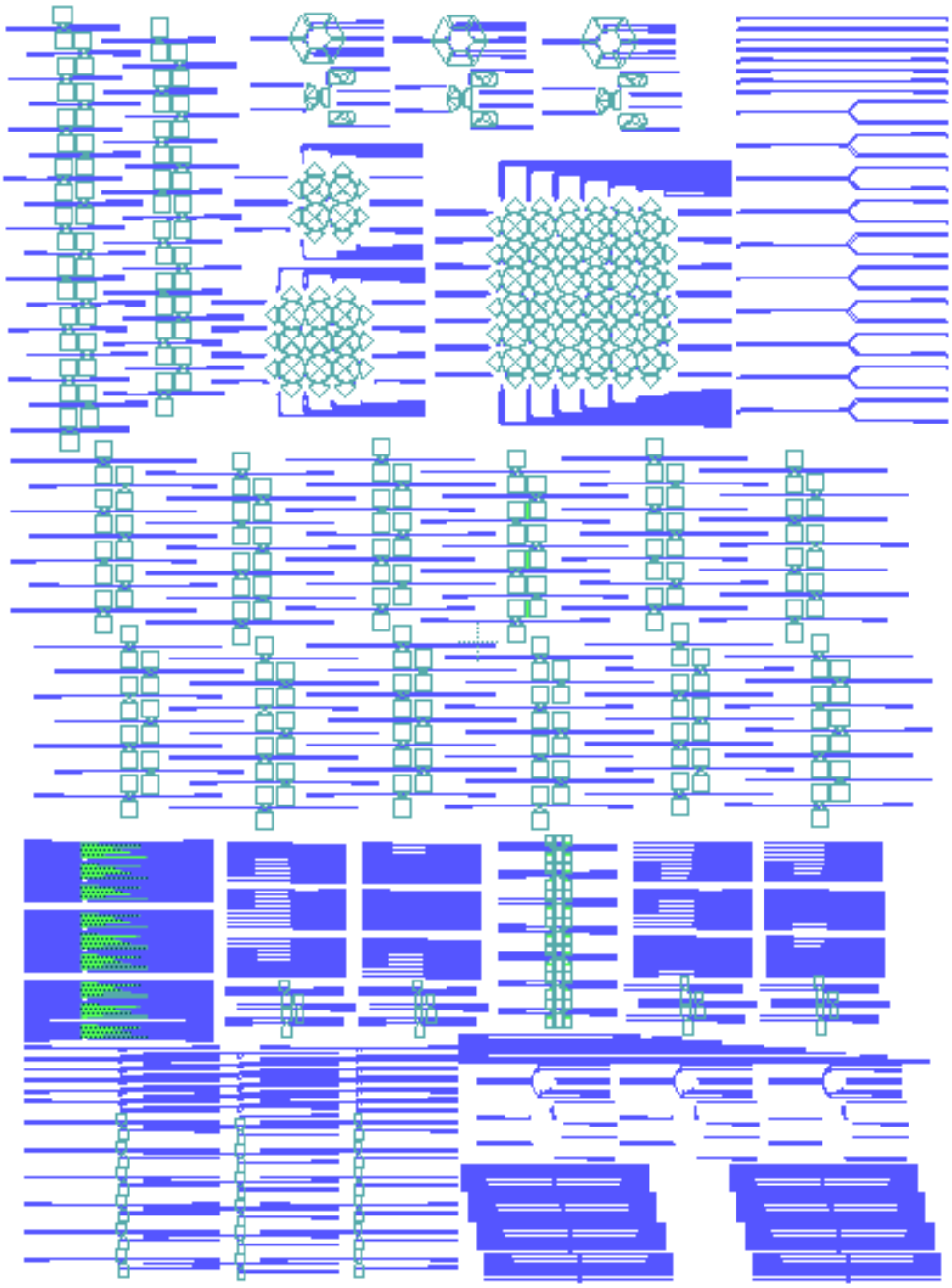

Figure A.9.2 – Mask design for implanted racetrack, implanted MZIs and implanted DCs used for high accuracy electrical annealing.

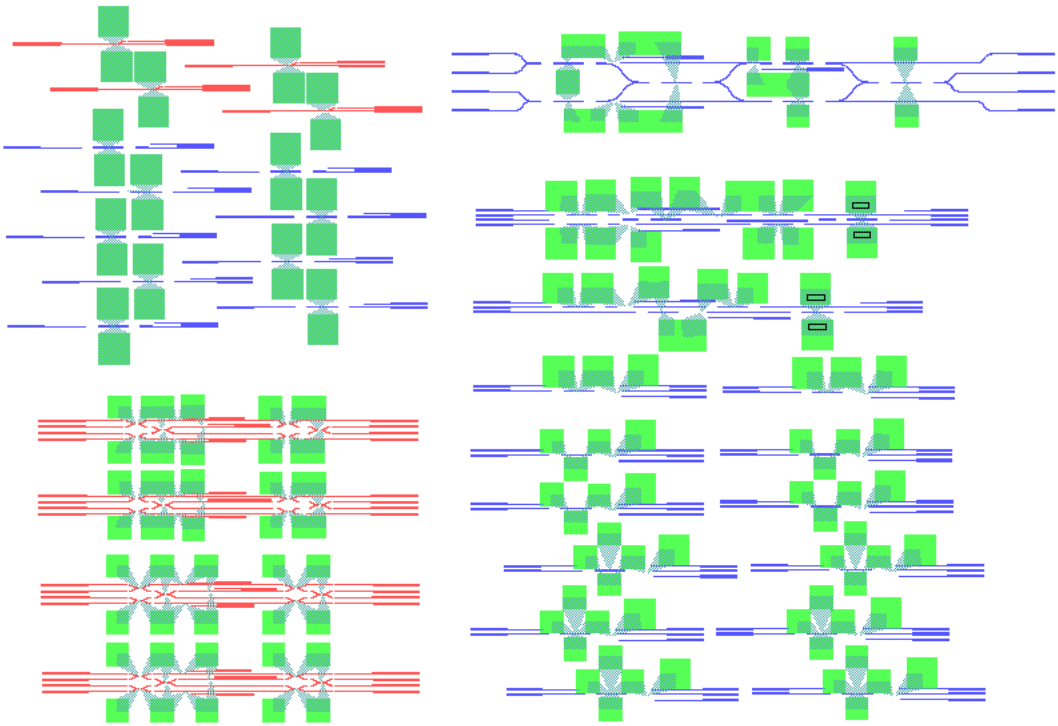

Figure A.9.3 – Mask design for implanted MZIs, implanted DCs and tuneable switching networks.

Appendix B Python scripts

The python scripts used for controlling the experimental setup are presented in the following section.

This script sweeping the applied voltage from 0V to 8V with a step of 0.5V. For each step, 4s is set as the waiting time.

```
####### define file and graphic interface
file = open('E:\PYTHON\Measurement20190305\Test8-1.csv', 'w')
#fil = open('\Measurement20190305\Noantenna3_agilent2_test_all.txt', 'w')

#### Define GPIB address #####
GPIB_address = "5"

####### define sweep parameters (possible starting WL 1892.8 to WL 2016 )
start_V = 0 #Volts
stop_V = 8 #Volts
step=0.5 #Volts
step_time = 4 #wait time between points
#num = 1

#### Import packages ####
import numpy as np
import time, random
import realtime_plot as rtp
from matplotlib import pyplot as plt
import math
from collections import deque

### Set up AgilentE3640A
from Agilent import AgilentE3640A
A = AgilentE3640A("GPIB::" + GPIB_address)

### Set up real time plot ####
fig, axes = plt.subplots()
display = rtp.RealtimePlot(axes)

#### Run a voltage scan: ###
#curr_zch = K.measure_current_zch()
```

```
#currents = np.empty(num)
for V in np.arange(start_V, stop_V+step, step):
#Set voltage
A.set_v(V)
#Pause for step_time
#for n in range(num):
time.sleep(step_time)
#Get current reading
curr = A.get_i()

# Add point to graph
#curr = currents.mean()
display.add(V, curr)
plt.pause(0.001)
# Write point to file
#print >> fil,V, currents
print >> file,V, curr

A.set_v(0.0)

file.close()
plt.show()
```

This script applied square annealing signal onto the electrical heater. The ON voltage is set as 1V and continues for 10s. The OFF voltage is 0V with another 10s waiting time. There are five cycles.

```
####### define file and graphic interface
file = open('E:\PYTHON\delete.csv', 'w')
#fil = open('\Measurement20190305\Noantenna3_agilent2_test_all.txt', 'w')

#### Define GPIB address #####
GPIB_address = "5"

####### define sweep parameters (possible starting WL 1892.8 to WL 2016 )
start_V = 0 #Voltsz
stop_V = 1 #Volts
step=0.2 #Volts
```

```
step_time = 10 #1s wait time between points
#num = 1

#### Import packages ####
import numpy as np
import time, random
import realtime_plot as rtp
from matplotlib import pyplot as plt
import math
from collections import deque

### Set up AgilentE3640A
from Agilent import AgilentE3640A
A = AgilentE3640A("GPIB::" + GPIB_address)
print(A.get_idn())
### Set up real time plot ####
fig, axes = plt.subplots()
display = rtp.RealtimePlot(axes)

#### Run a voltage scan: ###
#curr_zch = K.measure_current_zch()

#currents = np.empty(num)
for i in np.arange(0, 10, 1):
if (i%2 == 0):
V = start_V
#Set voltage
A.set_v(V)
#Pause for step_time
#for n in range(num):
time.sleep(step_time)
#Get current reading
curr = A.get_i()
A.set_v(0)
# Add point to graph
#curr = currents.mean()
display.add(i, curr)
plt.pause(0.001)
```

```
# Write point to file
#print >> fil,V, currents
print >> file,i,V, curr
else:
V = stop_V
#Set voltage
A.set_v(V)
#Pause for step_time
#for n in range(num):
time.sleep(step_time)
#Get current reading
curr = A.get_i()
A.set_v(0)
# Add point to graph
#curr = currents.mean()
display.add(i, curr)
plt.pause(0.001)
# Write point to file
#print >> fil,V, currents
print >> file,i,V, curr
A.set_v(0.0)

file.close()
plt.show()
```

List of References

[1] Reed G T, Knights A P. Silicon photonics: an introduction[M]. John Wiley & Sons, 2004.

[2] Won R. Integrating silicon photonics[J]. Nature photonics, 2010, 4(8): 498-499.

[3] Chen X, Li C, Tsang H K. Device engineering for silicon photonics[J]. NPG Asia Materials, 2011, 3(1): 34-40.

[4] Asghari M. Silicon photonics: a low-cost integration platform for datacom and telecom applications[C]//National Fiber Optic Engineers Conference. Optical Society of America, 2008: NThA4.

[5] Chrostowski L, Hochberg M. Silicon photonics design: from devices to systems[M]. Cambridge University Press, 2015.

[6] Liang D, Roelkens G, Baets R, et al. Hybrid integrated platforms for silicon photonics[J]. Materials, 2010, 3(3): 1782-1802.

[7] Jalali B, Fathpour S. Silicon photonics[J]. Journal of lightwave technology, 2006, 24(12): 4600-4615.

[8] Politi A, Cryan M J, Rarity J G, et al. Silica-on-silicon waveguide quantum circuits[J]. Science, 2008, 320(5876): 646-649.

[9] Preisler E J, Brooke J, Oldham N C, et al. Pulsed laser deposition growth of Fe 3 O 4 on III–V semiconductors for spin injection[J]. Journal of Vacuum Science & Technology B: Microelectronics and Nanometer Structures Processing, Measurement, and Phenomena, 2003, 21(4): 1745-1748.

[10] Tang M, Park J S, Wang Z, et al. Integration of III-V lasers on Si for Si photonics[J]. Progress in Quantum Electronics, 2019, 66: 1-18.

[11] Li N, Xin M, Su Z, et al. A silicon photonic data link with a monolithic erbium-doped laser[J]. Scientific reports, 2020, 10(1): 1-9.

[12] Liang D, Bowers J E. Recent progress in heterogeneous III-V-on-silicon photonic integration[J]. Light: Advanced Manufacturing, 2021, 2(1): 59-83.

[13] Baur C, Hermle M, Dimroth F, et al. Effects of optical coupling in III-V multilayer systems[J]. Applied physics letters, 2007, 90(19): 192109.

[14] Marchetti R, Lacava C, Carroll L, et al. Coupling strategies for silicon photonics integrated chips[J]. Photonics Research, 2019, 7(2): 201-239.

[15] Deri R J, Kapon E. Low-loss III-V semiconductor optical waveguides[J]. IEEE Journal of Quantum Electronics, 1991, 27(3): 626-640.

[16] Mu X, Wu S, Cheng L, et al. Edge couplers in silicon photonic integrated circuits: A review[J]. Applied Sciences, 2020, 10(4): 1538.

[17] Liu D, Xu H, Tan Y, et al. Silicon photonic filters[J]. Microwave and Optical Technology Letters, 2021, 63(9): 2252-2268.

[18] Zhang W, Yao J. On-chip silicon photonic integrated frequency-tunable bandpass microwave photonic filter[J]. Optics Letters, 2018, 43(15): 3622-3625.

[19] Bhandare S, Ibrahim S K, Sandel D, et al. Novel nonmagnetic 30-dB traveling-wave single-sideband optical isolator integrated in III/V material[J]. IEEE Journal of selected topics in quantum electronics, 2005, 11(2): 417-421.

[20] Garrigues M, Leclercq J L, Viktorovitch P. III-V semiconductor based MOEMS devices for optical telecommunications[J]. Microelectronic Engineering, 2002, 61: 933-945.

[21] Toliver P, Menendez R, Banwell T, et al. A programmable optical filter unit cell element for high resolution RF signal processing in silicon photonics[C]//2010 Conference on Optical Fiber Communication (OFC/NFOEC), collocated National Fiber Optic Engineers Conference. IEEE, 2010: 1-3.

[22] Zhu Y, Zhang F, Yang F, et al. Toward single lane 200G optical interconnects with silicon photonic modulator[J]. Journal of Lightwave Technology, 2019, 38(1): 67-74.

[23] Ummethala S, Kemal J N, Alam A S, et al. Hybrid electro-optic modulator combining silicon photonic slot waveguides with high-k radio-frequency slotlines[J]. Optica, 2021, 8(4): 511-519.

[24] Ibrahim S K, Bhandare S, Sandel D, et al. Non-magnetic 30 dB integrated optical isolator in III/V material[J]. Electronics Letters, 2004, 40(20): 1293-1294.

[25] Liu L, Van Campenhout J, Roelkens G, et al. Carrier-injection-based electro-optic modulator on silicon-on-insulator with a heterogeneously integrated III-V microdisk cavity[J]. Optics letters, 2008, 33(21): 2518-2520.

[26] Ikku Y, Yokoyama M, Ichikawa O, et al. Low-driving-current InGaAsP photonic-wire optical switches using III-V CMOS photonics platform[J]. Optics Express, 2012, 20(26): B357-B364.

[27] Li Q, Han J H, Ho C P, et al. Ultra-power-efficient 2× 2 Si Mach-Zehnder interferometer optical switch based on III-V/Si hybrid MOS phase shifter[J]. Optics Express, 2018, 26(26): 35003-35012.

[28] Fang Q, Song J F, Liow T Y, et al. Ultralow power silicon photonics thermo-optic switch with suspended phase arms[J]. IEEE Photonics Technology Letters, 2011, 23(8): 525-527.

[29] Beggs D M, White T P, O'Faolain L, et al. Ultracompact and low-power optical switch based on silicon photonic crystals[J]. Optics letters, 2008, 33(2): 147-149.

[30] Stillman G E, Robbins V M, Tabatabaie N. III-V compound semiconductor devices: Optical detectors[J]. IEEE Transactions on Electron Devices, 1984, 31(11): 1643-1655.

[31] Sun J, Han M, Gu Y, et al. Recent advances in group III–V nanowire infrared detectors[J]. Advanced Optical Materials, 2018, 6(18): 1800256.

[32] Verstuyft M, Akiki E, Walter B, et al. Proposal for an integrated silicon-photonics terahertz gas detector using photoacoustics[J]. Optics Express, 2020, 28(15): 22424-22442.

[33] Piels M, Bowers J E. Photodetectors for silicon photonic integrated circuits[J]. Photodetectors, 2016: 3-20.

[34] Li C, Tian R, Yi R, et al. MoTe2 PN homojunction constructed on a silicon photonic crystal cavity for high-performance photodetector[J]. ACS Photonics, 2021, 8(8): 2431-2439.

[35] LaPierre R R, Robson M, Azizur-Rahman K M, et al. A review of III–V nanowire infrared photodetectors and sensors[J]. Journal of Physics D: Applied Physics, 2017, 50(12): 123001.

[36] Li K, Liu S, Thomson D J, et al. Electronic–photonic convergence for silicon photonics transmitters beyond 100 Gbps on–off keying[J]. Optica, 2020, 7(11): 1514-1516.

[37] Chen Y, Lin H, Hu J, et al. Heterogeneously integrated silicon photonics for the mid-infrared and spectroscopic sensing[J]. ACS nano, 2014, 8(7): 6955-6961.

[38] Xie W, Komljenovic T, Huang J, et al. Heterogeneous silicon photonics sensing for autonomous cars[J]. Optics express, 2019, 27(3): 3642-3663.

[39] Wangüemert-Pérez J G, Hadij-ElHouati A, Sánchez-Postigo A, et al. Subwavelength structures for silicon photonics biosensing[J]. Optics & Laser Technology, 2019, 109: 437-448.

[40] Qi Y, Zheng Z, Banakar M, et al. Integrated switching circuit for low-noise self-referenced mid-infrared absorption sensing using silicon waveguides[J]. IEEE Photonics Journal, 2021, 13(6): 1-10.

[41] Jones R, Doussiere P, Driscoll J B, et al. Heterogeneously integrated InP silicon photonics: fabricating fully functional transceivers[J]. IEEE Nanotechnology Magazine, 2019, 13(2): 17-26.

[42] Filer, M. Co-packaging in future Microsoft data center networks: https://www.epic-assoc.com. **2021**.

[43] Westerveld W J, Mahmud-Ul-Hasan M, Shnaiderman R, et al. Sensitive, small, broadband and scalable optomechanical ultrasound sensor in silicon photonics[J]. Nature Photonics, 2021, 15(5): 341-345.

[44] Baets R. Silicon-Photonics-Based Spectroscopic Sensing for Environmental Monitoring and Health Care[C]//2021 Optical Fiber Communications Conference and Exhibition (OFC). Ieee, 2021: 1-42.

[45] Chen X, Meng F, Fortune S A, et al. Silicon photonic beam steering module with backside coupling elements toward dense heterogeneous integration with drive electronics[J]. APL Photonics, 2021, 6(11): 116106.

[46] Shen Y, Harris N C, Skirlo S, et al. Deep learning with coherent nanophotonic circuits[J]. Nature Photonics, 2017, 11(7): 441-446.

[47] Harris N C, Carolan J, Bunandar D, et al. Linear programmable nanophotonic processors[J]. Optica, 2018, 5(12): 1623-1631.

[48] Chen X, Milosevic M M, Stanković S, et al. The emergence of silicon photonics as a flexible technology platform[J]. Proceedings of the IEEE, 2018, 106(12): 2101-2116.

[49] Traverso M, Mazzini M, Lakshmikumar K, et al. Integrated Silicon Photonics Transceiver Module for 100Gbit/s 20km Transmission[C]//2021 Optical Fiber Communications Conference and Exhibition (OFC). IEEE, 2021: 1-3.

[50] Apple is entering silicon photonics.

http://www.yole.fr/Silicon_Photonics_Market_Update_2021.aspx, 2021.

[51] Silicon photonics reaches tipping point, with transceivers shipping in volume. http://www.semiconductor-today.com/features/PDF/semiconductor-today-april-may-2018-Silicon-photonics.pdf

[52] https://www.zurich.ibm.com/st/photonics/devices.html

[53] https://community.hpe.com/t5/Advancing-Life-Work/Advancing-photonics-research-for-HPC/ba-p/7147470#.YgErllh_rX0.

[54] Intel® Silicon Photonics: from Research to Product https://ewh.ieee.org/soc/cpmt/presentations/cpmt1703a.pdf

[55] Reed G T. Silicon photonics breaks new ground[C]//Silicon Photonics XVI. International Society for Optics and Photonics, 2021, 11691: 1169102.

[56] Lidar scales up thanks to silicon photonics. https://www.electrooptics.com/feature/lidar-scales-thanks-silicon-photonics

[57] Rogers C, Piggott A Y, Thomson D J, et al. A universal 3D imaging sensor on a silicon photonics platform[J]. Nature, 2021, 590(7845): 256-261.

[58] Vandoorne K, Mechet P, Van Vaerenbergh T, et al. Experimental demonstration of reservoir computing on a silicon photonics chip[J]. Nature communications, 2014, 5(1): 1-6.

[59] Zhao Z J, Shin S H, Lee S Y, et al. Direct Chemisorption-Assisted Nanotransfer Printing with Wafer-Scale Uniformity and Controllability[J]. ACS nano, 2022.

[60] Horikawa T, Shimura D, Jeong S H, et al. The impacts of fabrication error in Si wire-waveguides on spectral variation of coupled resonator optical waveguides[J]. Microelectronic Engineering, 2016, 156: 46-49.

[61] Chen X, Mohamed M, Li Z, et al. Process variation in silicon photonic devices[J]. Applied optics, 2013, 52(31): 7638-7647.

[62] Chrostowski L, Wang X, Flueckiger J, et al. Impact of fabrication non-uniformity on chip-scale silicon photonic integrated circuits[C]//Optical Fiber Communication Conference. Optical Society of America, 2014: Th2A. 37.

[63] Azuelos P, Girault P, Lorrain N, et al. Optimization of porous silicon waveguide design for micro-ring resonator sensing applications[J]. Journal of Optics, 2018, 20(8): 085301.

[64] Pantouvaki M, Verheyen P, De Coster J, et al. 56Gb/s ring modulator on a 300mm silicon photonics platform[C]//2015 European Conference on Optical Communication (ECOC). IEEE, 2015: 1-3.

[65] Reed G T, Mashanovich G, Gardes F Y, et al. Silicon optical modulators[J]. Nature photonics, 2010, 4(8): 518-526.

[66] Schrauwen J, Van Thourhout D, Baets R. Trimming of silicon ring resonator by electron beam induced compaction and strain[J]. Optics express, 2008, 16(6): 3738-3743.

[67] Prorok S, Petrov A Y, Eich M, et al. Trimming of high-Q-factor silicon ring resonators by electron beam bleaching[J]. Optics letters, 2012, 37(15): 3114-3116.

[68] Zhou L, Okamoto K, Yoo S J B. Athermalizing and trimming of slotted silicon microring resonators with UV-sensitive PMMA upper-cladding[J]. IEEE Photonics Technology Letters, 2009, 21(17): 1175-1177.

[69] Canciamilla A, Grillanda S, Morichetti F, et al. Photo-induced trimming of coupled ring-resonator filters and delay lines in As 2 S 3 chalcogenide glass[J]. Optics letters, 2011, 36(20): 4002-4004.

[70] Bogaerts W, Pérez D, Capmany J, et al. Programmable photonic circuits[J]. Nature, 2020, 586(7828): 207-216.

[71] Chen X, Stroobant P, Pickavet M, et al. Graph representations for programmable photonic circuits[J]. Journal of Lightwave Technology, 2020, 38(15): 4009-4018.

[72] Capmany J, Gasulla I, Pérez D. The programmable processor[J]. Nature Photonics, 2016, 10(1): 6-8.

[73] Chen X, Milosevic M M, Runge A F J, et al. Silicon erasable waveguides and directional couplers by germanium ion implantation for configurable photonic circuits[J]. Optics Express, 2020, 28(12): 17630-17642.

[74] Littlejohns C G, Rowe D J, Du H, et al. CORNERSTONE's silicon photonics rapid prototyping platforms: Current status and future outlook[J]. Applied Sciences, 2020, 10(22): 8201.

[75] Shen X, Chen B, Zhu Y, et al. Silicon photonic integrated circuits and its application in data center[C]//Seventh Symposium on Novel Photoelectronic Detection Technology and Applications. International Society for Optics and Photonics, 2021, 11763: 1176380.

[76] Jaturaphagorn, P.; Chattham, N.; Limsuwan, P.; et al. Optimization of end-fire coupling between an LED mid-IR light source and SiNx optical waveguides for spectroscopic sensing. *Results in Optics.* **2021**, *5*, 100174. [https://doi.org/10.1016/j.rio.2021.100174]

[77] Han, Y.T.; Yun, S.J.; Jung, H.D.; et al. A hybrid-integrated 400G TROSA module using chip-to-chip optical butt-coupling. *Optical Fiber Communication Conference*. Optical Society of America. **2020**, *M1F*. 3. [https://www.osapublishing.org/abstract.cfm?URI=OFC-2020-M1F.3]

[78] Zhang, W.Q.; Gao, M.X.; Guo, B. Tunable modulation of photonic spin Hall effect by using a prism-coupling waveguide with hyperbolic metamaterials. *JOSA B*, **2020**, *37*, 3777-3783. [https://doi.org/10.1364/JOSAB.408939]

[79] Selvaraja, S.K.; Vermeulen, D.; Schaekers, M.; et al. Highly efficient grating coupler between optical fiber and silicon photonic circuit. *Conference on Lasers and Electro-Optics and 2009 Conference on Quantum electronics and Laser Science Conference*. IEEE, **2009**, 1-2. [https://ieeexplore.ieee.org/stamp/stamp.jsp?arnumber=5225319]

[80] Chen X, Xu K, Cheng Z, et al. Wideband subwavelength gratings for coupling between silicon-on-insulator waveguides and optical fibers[J]. Optics letters, 2012, 37(17): 3483-3485.

[81] Deen M J, Basu P K. Silicon photonics: fundamentals and devices[M]. John Wiley & Sons, 2012.

[82] Sarid D. High efficiency input–output prism waveguide coupler: an analysis[J]. Applied optics, 1979, 18(17): 2921-2926.

[83] Chen X, Li C, Tsang H K. Device engineering for silicon photonics[J]. NPG Asia Materials, 2011, 3(1): 34-40.

[84] Almeida V R, Panepucci R R, Lipson M. Nanotaper for compact mode conversion[J]. Optics letters, 2003, 28(15): 1302-1304.

[85] Sure A, Dillon T, Murakowski J, et al. Fabrication and characterization of three-dimensional silicon tapers[J]. Optics express, 2003, 11(26): 3555-3561.

[86] Barwicz T, Janta-Polczynski A, Khater M, et al. An O-band metamaterial converter interfacing standard optical fibers to silicon nanophotonic waveguides[C]//Optical Fiber Communication Conference. Optical Society of America, 2015: Th3F. 3.

[87] Dewanjee A. Efficient Light Coupling Techniques for Integrated Photonics[D]. University of Toronto (Canada), 2017.

[88] Scarcella C, Gradkowski K, Carroll L, et al. Pluggable single-mode fiber-array-to-PIC coupling using micro-lenses[J]. IEEE Photonics Technology Letters, 2017, 29(22): 1943-1946.

[89] Dietrich P I, Blaicher M, Reuter I, et al. In situ 3D nanoprinting of free-form coupling elements for hybrid photonic integration[J]. Nature Photonics, 2018, 12(4): 241-247.

[90] Lee J M, Kim K J, Kim G. Enhancing alignment tolerance of silicon waveguide by using a wide grating coupler[J]. Optics Express, 2008, 16(17): 13024-13031.

[91] Roelkens G, Van Thourhout D, Baets R. High efficiency grating coupler between silicon-on-insulator waveguides and perfectly vertical optical fibers[J]. Optics letters, 2007, 32(11): 1495-1497.

[92] Taillaert D, Van Laere F, Ayre M, et al. Grating couplers for coupling between optical fibers and nanophotonic waveguides[J]. Japanese Journal of Applied Physics, 2006, 45(8R): 6071.

[93] Chen X, Xu K, Cheng Z, et al. Wideband subwavelength gratings for coupling between silicon-on-insulator waveguides and optical fibers[J]. Optics letters, 2012, 37(17): 3483-3485.

[94] Michels T, Aksyuk V. Optical probe for nondestructive wafer-scale characterization of photonic elements[J]. IEEE Photonics Technology Letters, 2017, 29(8): 643-646.

[95] Trappen M, Blaicher M, Dietrich P I, et al. 3D-printed optical probes for wafer-level testing of photonic integrated circuits[J]. Optics Express, 2020, 28(25): 37996-38007.

[96] Automated Wafer-level PIC Test. https://www.photonics.com/Products/Automated_Wafer-level_PIC_Test/pr66556

[97] Testing photonic integrated circuits. https://www.exfo.com/en/solutions/academic-research-institutions/pic-testing/

[98] Topley R, Martinez-Jimenez G, O'Faolain L, et al. Locally erasable couplers for optical device testing in silicon on insulator[J]. Journal of Lightwave Technology, 2014, 32(12): 2248-2253.

[99] Topley R, O'Faolain L, Thomson D J, et al. Planar surface implanted diffractive grating couplers in SOI[J]. Optics Express, 2014, 22(1): 1077-1084.

[100] Topley R. Erasable diffractive grating couplers in silicon on insulator[D]. University of Southampton, 2014.

[101] Yu X, Chen X, Milosevic M M, et al. Ge Ion Implanted Photonic Devices and Annealing for Emerging Applications[J]. Micromachines, 2022, 13(2): 291.

[102] Bachman D, Chen Z, Fedosejevs R, et al. Permanent fine tuning of silicon microring devices by femtosecond laser surface amorphization and ablation[J]. Optics express, 2013, 21(9): 11048-11056.

[103] Chen X, Milosevic M M, Thomson D J, et al. Post-fabrication phase trimming of Mach–Zehnder interferometers by laser annealing of germanium implanted waveguides[J]. Photonics Research, 2017, 5(6): 578-582.

[104] Milosevic M M, Chen X, Cao W, et al. Ion implantation in silicon for trimming the operating wavelength of ring resonators[J]. IEEE Journal of Selected Topics in Quantum Electronics, 2018, 24(4): 1-7.

[105] Knights A P, Wang Z, Paez D, et al. Electrical trimming of the resonance of a silicon micro-ring resonator[C]//2017 IEEE 14th International Conference on Group IV Photonics (GFP). IEEE, 2017: 29-30.

[106] Hagan D E, Torres-Kulik B, Knights A P. Post-fabrication trimming of silicon ring resonators via integrated annealing[J]. IEEE Photonics Technology Letters, 2019, 31(16): 1373-1376.

[107] Jayatilleka H, Frish H, Kumar R, et al. Post-fabrication trimming of silicon photonic ring resonators at wafer-scale[J]. Journal of Lightwave Technology, 2021, 39(15): 5083-5088.

[108] Shoji Y, Kintaka K, Suda S, et al. Low-crosstalk 2× 2 thermo-optic switch with silicon wire waveguides[J]. Optics Express, 2010, 18(9): 9071-9075.

[109] Miller D A B. Self-aligning universal beam coupler[J]. Optics express, 2013, 21(5): 6360-6370.

[110] Quack N, Sattari H, Takabayashi A Y, et al. MEMS-enabled silicon photonic integrated devices and circuits[J]. IEEE Journal of Quantum Electronics, 2019, 56(1): 1-10.

[111] Errando-Herranz C, Takabayashi A Y, Edinger P, et al. MEMS for photonic integrated circuits[J]. IEEE Journal of Selected Topics in Quantum Electronics, 2019, 26(2): 1-16.

[112] Ollier E. Optical MEMS devices based on moving waveguides[J]. IEEE Journal of selected topics in quantum electronics, 2002, 8(1): 155-162.

[113] Ríos C, Stegmaier M, Hosseini P, et al. Integrated all-photonic non-volatile multi-level memory[J]. Nature photonics, 2015, 9(11): 725-732.

[114] Delaney M, Zeimpekis I, Du H, et al. Nonvolatile programmable silicon photonics using an ultralow-loss Sb2Se3 phase change material[J]. Science Advances, 2021, 7(25): eabg3500.

[115] Fang Z, Zheng J, Saxena A, et al. Non-Volatile Reconfigurable Integrated Photonics Enabled by Broadband Low-Loss Phase Change Material[J]. Advanced Optical Materials, 2021, 9(9): 2002049.

[116] Delaney M, Zeimpekis I, Lawson D, et al. A new family of ultralow loss reversible phase-change materials for photonic integrated circuits: Sb2S3 and Sb2Se3[J]. Advanced Functional Materials, 2020, 30(36): 2002447.

[117] Pai S, Williamson I A D, Hughes T W, et al. Parallel programming of an arbitrary feedforward photonic network[J]. IEEE Journal of Selected Topics in Quantum Electronics, 2020, 26(5): 1-13.

[118] Miller D A B. Setting up meshes of interferometers–reversed local light interference method[J]. Optics Express, 2017, 25(23): 29233-29248.

[119] Zhuang L, Roeloffzen C G H, Hoekman M, et al. Programmable photonic signal processor chip for radiofrequency applications[J]. Optica, 2015, 2(10): 854-859.

[120] Pérez, D. et al. Multipurpose silicon photonics signal processor core. Nat. Commun. 8, 1–9 (2017).

[121] Pérez-López, D., Gutierrez, A. M., Sánchez, E., DasMahapatra, P. & Capmany, J. Integrated photonic tunable basic units using dual-drive directional couplers. Opt. Express 27, 38071 (2019).

[122] Franssila S. Introduction to microfabrication[M]. John Wiley & Sons, 2010.

[123] Holmström E, Kuronen A, Nordlund K. Threshold defect production in silicon determined by density functional theory molecular dynamics simulations[J]. Physical Review B, 2008, 78(4): 045202.

[124] Bai G, Nicolet M A. Defects production and annealing in self-implanted Si[J]. Journal of applied physics, 1991, 70(2): 649-655.

[125] Ghosh G. Temperature dispersion of refractive indices in crystalline and amorphous silicon[J]. Applied physics letters, 1995, 66(26): 3570-3572.

[126] Juarez D I A, Zimmermann L. Loss measurement of SOI nano-wires[J]. 2010.

[127] Hanim A R, Hazura H, Mardiana B, et al. Free carrier absorption loss on pin and npn silicon phase modulator at λ= 1.3 μm and λ= 1.55 μm[C]//2010 IEEE International Conference on Semiconductor Electronics (ICSE2010). IEEE, 2010: 351-354.

[128] Barwicz T, Haus H A. Three-dimensional analysis of scattering losses due to sidewall roughness in microphotonic waveguides[J]. Journal of Lightwave Technology, 2005, 23(9): 2719.

[129] Cocorullo G, Della Corte F G, Rendina I, et al. Thermo-optic effect exploitation in silicon microstructures[J]. Sensors and Actuators A: Physical, 1998, 71(1-2): 19-26.

[130] Baranova E C, Gusev V M, Martynenko Y V, et al. On silicon amorphisation during different mass ions implantation[M]//Ion implantation in semiconductors and other materials. Springer, Boston, MA, 1973: 59-71.

[131] Kachurin G A, Pridaehin N B, Jmimov L S. Annealing of radiation-induced defects by pulsed laser irradiation[J]. Fizika I Tekhnika Poluprovodnikov, 1975, 9: 1429.

[132] Antonenko A K, n N N, Dvurechenskij A V, et al. Distribution of an impurity implanted into silicon after laser annealing[J]. Fizika i Tekhnika Poluprovodnikov, 1976, 10(1): 139-140.

[133] Bell A E. Review and analysis of laser annealing[J]. Rca Review, 1979, 40(3): 295.

[134] Gat A, Gerzberg L, Gibbons J F, et al. cw laser anneal of polycrystalline silicon: Crystalline structure, electrical properties[J]. Applied Physics Letters, 1978, 33(8): 775-778.

[135] Baeri P, Rimini E. Laser annealing of silicon[J]. Materials chemistry and physics, 1996, 46(2-3): 169-177.

[136] Auston D H, Surko C M, Venkatesan T N C, et al. Time-resolved reflectivity of ion-implanted silicon during laser annealing[J]. Applied physics letters, 1978, 33(5): 437-440.

[137] Boyd I W. A review of laser beam applications for processing silicon[J]. Contemporary physics, 1983, 24(5): 461-490.

[138] Laser annealing of semiconductors[M]. Elsevier, 2012.

[139] Reed G T. Silicon photonics: the state of the art[J]. 2008.

[140] Nedeljković M. Silicon photonic modulators for the mid-infrared[D]. University of Southampton, 2013.

[141] Fischer U, Zinke T, Kropp J R, et al. 0.1 dB/cm waveguide losses in single-mode SOI rib waveguides[J]. IEEE Photonics Technology Letters, 1996, 8(5): 647-648.

[142] Somekh S, Garmire E, Yariv A, et al. Channel optical waveguide directional couplers[J]. Applied physics letters, 1973, 22(1): 46-47.

[143] L. Soldano and E. Pennings, “Optical multi-mode interference devices based on self-imaging: principles and applications,” J. Lightwave Technol., vol. 13, pp. 615–627, apr 1995.

[144] Cao W. High-speed silicon photonics modulators for the 2 μm wavelength[D]. University of Southampton, 2020.

[145] Johnson, Mack H. Low Q-factor Silicon Photonic Cavities for Optical Filtering and Single-Photon Detection. [D]. University of Bristol, 2020.

[146] Bogaerts W, De Heyn P, Van Vaerenbergh T, et al. Silicon microring resonators[J]. Laser & Photonics Reviews, 2012, 6(1): 47-73.

[147] Li W, Guler U, Kinsey N, et al. Refractory plasmonics with titanium nitride: broadband metamaterial absorber[J]. Advanced Materials, 2014, 26(47): 7959-7965.

[148] Haynes W M, Lide D R, Bruno T J. CRC handbook of chemistry and physics[M]. CRC press, 2016.

[149] Chen B, Yu X, Chen X, et al. Real-time monitoring and gradient feedback enable accurate trimming of ion-implanted silicon photonic devices[J]. Optics express, 2018, 26(19): 24953-24963.

[150] Milosevic M M, Chen X, Yu X, et al. Ion implantation of germanium into silicon for critical coupling control of racetrack resonators[J]. Journal of Lightwave Technology, 2020, 38(7):

1865-1873.

[151] Marinov M, Zotov N. Model investigation of the Raman spectra of amorphous silicon[J]. Physical Review B, 1997, 55(5): 2938.

[152] Vink R L C, Barkema G T, van Der Weg W F. Raman spectra and structure of amorphous Si[J]. Physical Review B, 2001, 63(11): 115210.

[153] Kolobov A V. Raman scattering from Ge nanostructures grown on Si substrates: Power and limitations[J]. Journal of Applied Physics, 2000, 87(6): 2926-2930.

[154] Yu X, Chen X, Milosevic M M, et al. Electrically Erasable Optical I/O for Wafer Scale Testing of Silicon Photonic Integrated Circuits[J]. IEEE Photonics Journal, 2020, 12(5): 1-8.

[155] Chinni V R, Huang T C, Wai P K A, et al. Crosstalk in a lossy directional coupler switch[J]. Journal of Lightwave Technology, 1995, 13(7): 1530-1535.

[156] Morino H, Maruyama T, Iiyama K. Reduction of wavelength dependence of coupling characteristics using Si optical waveguide curved directional coupler[J]. Journal of lightwave technology, 2014, 32(12): 2188-2192.

[157] Harris N C, Ma Y, Mower J, et al. Efficient, compact and low loss thermo-optic phase shifter in silicon[J]. Optics express, 2014, 22(9): 10487-10493.

[158] Bogaerts W, Takabayashi A Y, Edinger P, et al. Programmable silicon photonic circuits powered by MEMS[C]//Smart Photonic and Optoelectronic Integrated Circuits 2022. SPIE, 2022, 12005: 55-69.

[159] Shen Y, Harris N C, Skirlo S, et al. Deep learning with coherent nanophotonic circuits[J]. Nature Photonics, 2017, 11(7): 441-446.